

## **General Disclaimer**

### **One or more of the Following Statements may affect this Document**

- This document has been reproduced from the best copy furnished by the organizational source. It is being released in the interest of making available as much information as possible.
- This document may contain data, which exceeds the sheet parameters. It was furnished in this condition by the organizational source and is the best copy available.
- This document may contain tone-on-tone or color graphs, charts and/or pictures, which have been reproduced in black and white.
- This document is paginated as submitted by the original source.
- Portions of this document are not fully legible due to the historical nature of some of the material. However, it is the best reproduction available from the original submission.

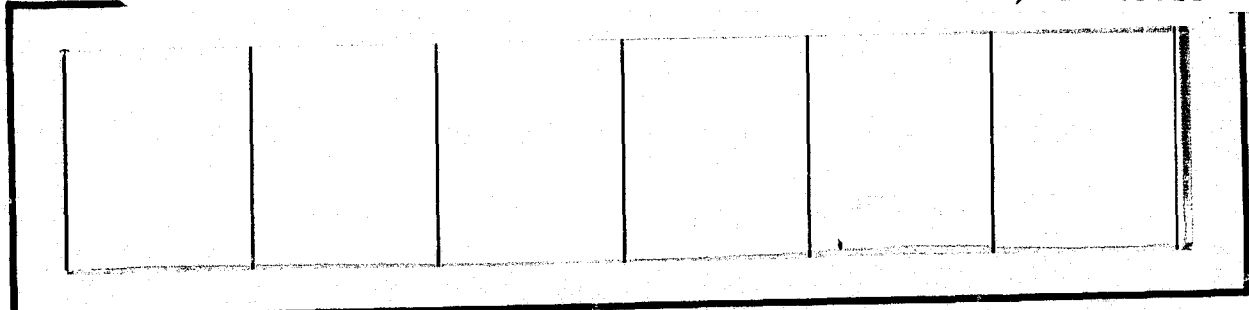
NASA CR-

147842

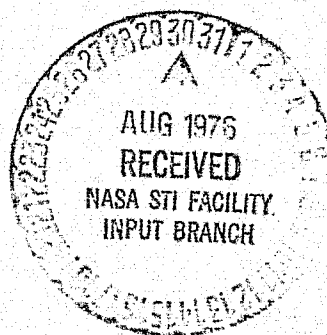
N76-30420

(NASA-CR-147842) STUDY TO INVESTIGATE AND  
EVALUATE MEANS OF OPTIMIZING THE RADAR  
FUNCTION FOR THE SPACE SHUTTLE Final Report  
(Axiomatix, Marina del Rey, Calif.) 180 p  
HC \$7.50

Unclassified  
CSCL 17I G3/32 48425



 Axiomatix



Marina del Rey • California

**STUDY TO INVESTIGATE AND EVALUATE MEANS  
OF OPTIMIZING THE RADAR FUNCTION  
FOR THE SPACE SHUTTLE**

**Final Report**

**Contract No. NAS 9-14614  
Exhibit B**

**Prepared for**

**NASA Lyndon B. Johnson Space Center  
Houston, Texas 77058**

**Prepared by**

**Axiomatix  
13900 Panay Way, Suite 110M  
Marina del Rey, California 90291**

**Axiomatix Report No. R7607-4  
July 31, 1976**

## TABLE OF CONTENTS

	<u>Page</u>
<b>1.0 INTRODUCTION AND OVERVIEW . . . . .</b>	<b>1</b>
<b>2.0 THE ORBITER MONOPULSE ANTENNA ANGULAR CONTROL SYSTEM . . . . .</b>	<b>4</b>
<b>2.1 Communication Mode . . . . .</b>	<b>4</b>
<b>2.2 Radar Antenna Angle Rate Considerations . . . . .</b>	<b>5</b>
<b>3.0 SPIRAL SCAN CONSIDERATIONS . . . . .</b>	<b>10</b>
<b>4.0 POWER BUDGETS FOR PASSIVE TARGET DETECTOR - PULSE DOPPLER RADAR . . . . .</b>	<b>13</b>
<b>5.0 SIGNAL DESIGN CONSIDERATIONS FOR PULSE DOPPLER RADAR SYSTEM . . . . .</b>	<b>16</b>
<b>5.1 Detection Mode . . . . .</b>	<b>16</b>
<b>5.2 Acquisition Mode . . . . .</b>	<b>17</b>
<b>5.3 Tracking Mode . . . . .</b>	<b>17</b>
<b>5.4 Short Range Tracking Mode . . . . .</b>	<b>19</b>
<b>5.5 Parameters Summary for Baseline Case . . . . .</b>	<b>19</b>
<b>6.0 GROUND RETURN ANALYSIS . . . . .</b>	<b>21</b>
<b>7.0 RADAR/COMMUNICATION SYSTEM BLOCK DIAGRAM - SUMMARIZING DESCRIPTION . . . . .</b>	<b>22</b>
<b>7.1 Transmitter . . . . .</b>	<b>22</b>
<b>7.2 Antenna . . . . .</b>	<b>24</b>
<b>7.3 Receivers . . . . .</b>	<b>24</b>
<b>7.3.1 Radar Mode . . . . .</b>	<b>25</b>
<b>7.3.2 Communication Mode . . . . .</b>	<b>26</b>
<b>8.0 CONCLUSION . . . . .</b>	<b>28</b>
<b>Appendix L The Orbiter Monopulse Antenna Angular Control System</b>	
<b>Appendix M Spiral Scan Analysis</b>	
<b>Appendix N Power Budgets for Passive Target Detection - Pulse Doppler Radar</b>	
<b>Appendix O Signal Design for Pulse Doppler Radar System</b>	
<b>Appendix P Ground Return Analysis</b>	

## 1.0 INTRODUCTION AND OVERVIEW

This is the final report for Phase II of the "Study to Investigate and Evaluate Means of Optimizing the Radar Function for the Space Shuttle." During the earlier Phase I part of the study, the primary objectives were to consider the optimization of only the radar function, i.e., without considering any other function, such as the Ku-band communication system which is also carried on board the Shuttle. However, as the study progressed, a previously established concept of time-sharing the Ku-band equipment between the radar and the communication functions regained a predominant role in NASA's design philosophy. Consequently, the optimization of the radar function was modified accordingly to conform with the ultimate goal of an integrated radar/communication system design. For example, the considerations in the choice of the radar operating frequency were narrowed down to the region of the Shuttle's Ku-band communication system, which operates via the TDRS in the 13 to 15 GHz frequency range.

Also, the two-axis amplitude monopulse angle tracking technique, which is one of the major functions performed by the radar subunit, is being considered in terms of its compatibility with the communication signal tracking requirements. Specifically, the considerations of the angular search methods for the radar mode indicate that these methods can be adapted to the requirements of the communication mode, thus increasing the areas of equipment commonality. It appears, therefore, that a properly designed integrated radar/communication system can provide an overall savings in component requirements by time-sharing the two functions.

The considerations required for integrating the radar/communication functions also point to the advantages of sharing the transmitter tube between the two modes. But, since the communication transmitter is limited to about 50 watts peak power (being a 50-watt CW tube), the radar system signal design must be compatible with this peak power constraint. During

Phase I of this contract, it was established that a coherent pulse doppler system can perform satisfactorily within the 50-watt peak power limitation.

The coherent pulse doppler radar is characterized by a relatively high duty cycle, 0.1 to 0.7 typically, and the analysis indicates that, with all of the other system parameters properly selected (i.e., dish size, system losses, operating frequency, etc.), this type of radar can be implemented by sharing the communication transmitter tube and the monopulse angle tracking components.

With the pulse doppler radar, the range rate is determined nonambiguously by measuring the doppler shift of the main PRF spectral line. However, the doppler shifts associated with the passive and cooperative targets necessitate minimum PRFs of about 10 kpps and 100 kpps, respectively, to insure nonambiguous main line detection, acquisition and tracking.

For either the passive or the cooperative target case, these PRFs are considered to be too high to provide nonambiguous range acquisition. Thus, special techniques for resolving the range ambiguity, such as multiple PRFs with the Chinese remainder theorem algorithm, are proposed.

The decision to concentrate on providing maximum subunit commonality between the radar and the communication equipment resulted in detailed analytical studies of the TDRS acquisition and tracking performance with the two-axis monopulse system required for the radar mode. Preliminary results, which did not include the effect of platform stabilization, were presented in the final report for Phase I. During Phase II, the TDRS acquisition and tracking analysis was expanded to include the effects of a stabilized platform, as well as the effects of a special acquisition mode which utilizes a wide beamwidth horn. Section 2.0 of this report summarizes the results of the latest analysis and the details are given in Appendix L.\*

---

\* Because the topics of this final report are logical extensions and additions to the material contained in the final report for Phase I, the Appendix notation is a continuation of the notation used in the earlier report.

The advantages of the spiral scan for angular acquisition of both the radar targets and the TDRS were established in the early part of Phase II. Consequently, a detailed analysis of the spiral scan was performed for antenna sizes ranging from 20 inches to 36 inches in diameter and for search angles characteristic of both the radar and the communication acquisition modes. The results of this analysis are summarized in Section 3.0, and the analysis itself is given in Appendix M.

In view of the potential advantages to be gained from the use of antennas larger than the 20-inch diameter of the baseline dish, the power budgets for passive target radar detection were calculated for antenna diameters ranging from 20 to 36 inches. Dwell times commensurate with spiral scan were used for these budget calculations. Section 4.0 presents a brief summary of the results, with the details given in Appendix N.

The signal design for the candidate pulse doppler system is summarized in Section 5.0, and Appendix O provides the supporting analysis.

Section 6.0 provides the summary of the ground return analysis carried out for the passive target radar mode. The details of this analysis are presented in Appendix P.

And finally, the summarizing description of the proposed candidate radar/communication system configuration is given in Section 7.0.

## 2.0 THE ORBITER MONOPULSE ANTENNA ANGULAR CONTROL SYSTEM

### 2.1 Communication Mode

The Ku-band link from the TDRS to the Orbiter requires PN spreading to reduce the power density of the TDRS signal incident upon the earth's surface. Therefore, when considering the monopulse antenna angular control system operation in the communication mode, the basic question is: Can the angle tracking be performed on the spread signal, thus eliminating the need for code synchronization prior to angle acquisition? The results of our detailed analysis indicate that the angle tracking of the TDRS PN spread communication signal received by the Orbiter can indeed be carried out directly on the spread wideband waveform. Hence, PN despreading is not necessary in the angle tracking loop, thereby significantly simplifying the acquisition sequence of the TDRS waveform by the Orbiter Ku-band communication receiver.

A coherent amplitude comparison monopulse system angle tracking system for the Ku-band communication signal from the TDRS is proposed for the baseline system. This system is similar to that baselined for the radar mode. The analysis is carried out for single axis tracking only. The results are sufficiently optimistic, however, to allow a more than ample safety margin for any crosstalk which may be encountered in a two-axis monopulse system. Specific characteristics of the baseline system (see Figure 1 of Appendix L) which we propose are:

- (a) The monopulse angle tracking signal is derived directly from the PN spread received signal, with no spectrum compression and no data wipe-off.
- (b) A noncoherent AGC is used.
- (c) A coherent amplitude phase detector (CAD) is employed to generate the angle information.

For this system, the RMS angle tracking error due to receiver front-end noise is shown to be

$$\sigma_{\Delta_e} \approx 5 \times 10^{-3} \text{ degrees}$$

when the ratio of the average received power in the sum channel at bore-sight to the one-sided noise power spectral density is

$$\frac{P_{\text{rec}}}{N_0} = 73.2 \text{ dB-Hz}.$$

This result was determined using conservative design values for the IF bandwidth, the antenna error angle gain characteristic, and the angle control system loop bandwidth.

The RMS error shown is very small compared to any realistic specification that is expected. This performance prediction is also more than an order of magnitude below the specification for the angle tracking of the Ku-band radar in both the skin-track and cooperative modes of operation.

In Appendix L, the following cases are considered:

- (1) No despreading and a preamplifier in both the sum and difference channels.
- (2) No despreading and a preamplifier in the sum channel only.

The latter case corresponds to the present baseline configuration. Also, in the development of the RMS error, the signal loss incurred in passing through the IF filters is taken into account.

## 2.2 Radar Antenna Angle Rate Considerations

The measurement of the radar target angular motion rate is one of the requirements of the radar mode. A technique for obtaining the angular rate information of the target motion with respect to an inertial reference is presented below. This technique has previously been used successfully in the Apollo system. The angle control system is the same

as that discussed in Addendum A of Appendix L, except that the error signal is derived from the skin radar return instead of the TDRS wideband communication signal. The angle error,  $\varepsilon$ , between the target and the antenna boresight is

$$\varepsilon = \theta_T - \theta_A \quad (1)$$

where  $\theta_T$  = target angle

$\theta_A$  = antenna boresight angle.

All angles are assumed to be with respect to an inertial reference. The error signal developed in the radar receiver which feeds into the angle control system is proportional to  $\varepsilon$ . Taking the time derivatives and rearranging them,

$$\dot{\theta}_T = \dot{\varepsilon} + \dot{\theta}_A. \quad (2)$$

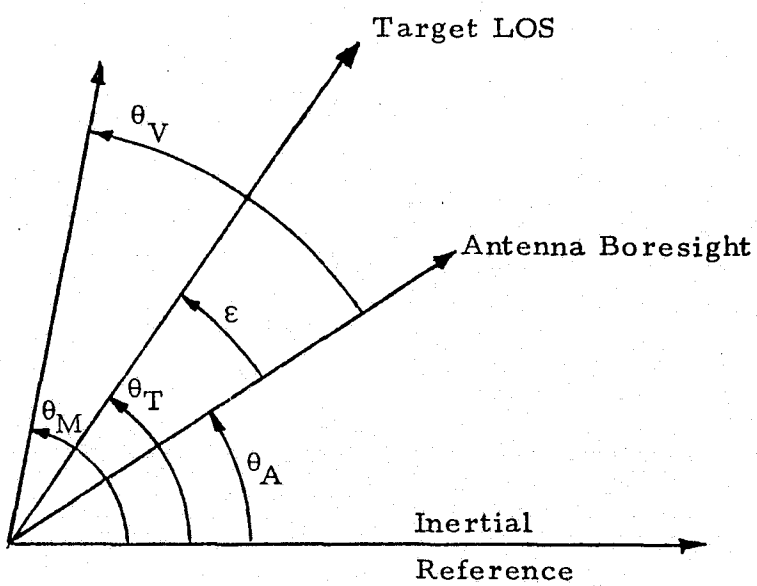


Figure 1. Angle Geometry With Respect to an Inertial Reference

The quantity we are interested in is  $\dot{\theta}_T$ , the angular rate of the target with respect to an inertial reference. If we had available the time derivative of the error signal and the time derivative of the antenna angle with respect to an inertial reference, we could easily obtain  $\dot{\theta}_T$ . We could then obtain  $\dot{\epsilon}$  from  $\epsilon$ . It may be noisy, however, but  $\dot{\theta}_A$  is not available.

Alternatively, the antenna angle can also be expressed as

$$\theta_A = \theta_M - \theta_V \quad (3)$$

where  $\theta_V$  = vehicle angle

$\theta_M$  = motor angle.

If the vehicle was stationary, and we arbitrarily placed the inertial reference with respect to the vehicle, then the antenna angle would be the same as the motor angle.

Taking the time derivatives,

$$\dot{\theta}_A = \dot{\theta}_M - \dot{\theta}_V \quad (4)$$

The motor responds to two different signals, one resulting from the target error and the other resulting from the angular rotation of the vehicle.

We therefore decompose  $\dot{\theta}_M$  into

$$\dot{\theta}_M = \dot{\theta}_{MV} + \dot{\theta}_{MT} \quad (5)$$

where  $\dot{\theta}_{MV}$  = motor motion due to the vehicle

$\dot{\theta}_{MT}$  = motor motion due to the target.

Substituting (5) into (4), and (4) into (2),

$$\dot{\theta}_T = \dot{\epsilon} + \dot{\theta}_{MT} + (\dot{\theta}_{MV} - \dot{\theta}_V) \quad (6)$$

Using the assumption that the inertial stabilization loop is functioning properly, then

$$\dot{\theta}_{MV} - \dot{\theta}_V \approx 0 \quad (7)$$

and  $\dot{\theta}_T = \dot{\varepsilon} + \dot{\theta}_{MT}$ . (8)

The motion of the motor required to track the target is

$$\dot{\theta}_{MT} = \dot{\theta}_A. \quad (9)$$

This can be seen by substituting (5) into (4) and using (7). Substituting (9) into (8),

$$\dot{\theta}_T = \dot{\varepsilon} + \dot{\theta}_A. \quad (10)$$

Since  $\dot{\theta}_A$  is not accessible, a satisfactory alternative is to apply the command rate voltage, designated as  $\dot{\theta}_c$ , into the rate gyro (see Addendum A of Appendix L). Therefore,

$$\dot{\theta}_T \approx \dot{\theta}_c + \dot{\varepsilon}(t). \quad (11)$$

The voltage  $\dot{\theta}_c$  is also directly proportional to the angle error signal  $\varepsilon(t)$ , so that

$$\dot{\theta}_T \approx \alpha \varepsilon(t) + \dot{\varepsilon}(t), \quad (12)$$

where  $\alpha$  is a proportionality constant. If

$$|\dot{\varepsilon}| \ll \varepsilon \quad (13)$$

which is the case with the targets that are anticipated, then a satisfactory approximation is given by

$$\dot{\theta}_T \approx \alpha \varepsilon(t). \quad (14)$$

This is certainly appealing since  $\varepsilon(t)$  is directly accessible in the antenna angle control system. This approximation was used successfully in Apollo, and is proposed in the baseline Ku-band system of the Orbiter as the method of obtaining the angular rate of the target with respect to an inertial reference.

It appears that such an approximation will always be very accurate, provided the target angular motion is small.

### 3.0 SPIRAL SCAN CONSIDERATIONS

For both the radar targets and the TDRS acquisition regions defined by conical angles, the spiral scan offers definite advantages over the rectangular search pattern. First, if the antenna is designated towards the expected target, or TDRS direction (vectored search), the spiral scan begins the search from that direction and thus maximizes the probability of an intercept. Second, with the spiral scan, the search is performed over the area of a circle which is inscribed within the square defined by the limits of the rectangular scan. Thus, strictly from the standpoint of the scan area required to search out the uncertainty limits, the circular scan is more efficient than the rectangular scan by a factor of  $4/\pi$ . Furthermore, with a rectangular scan, about 20% of line time must be allowed for scan reversal. The total increase in scan time requirement is

$$\frac{\text{Rectangular scan time}}{\text{Spiral scan time}} = \frac{4}{\pi} (1.2) = 1.53, \text{ or } 1.85 \text{ dB.} \quad (15)$$

Or, conversely, at least 1.85 dB is gained in dwell time by the use of a spiral scan which is confined to the circular area whose diameter is equal to the sides of the rectangular pattern. Note that, in both cases, the diameter of the circular and the sides of the rectangular search patterns, respectively, are determined by the  $\pm 3\sigma$  angle uncertainty of the target's (or TDRS') initial position with respect to the designated axis.

As with any other scan pattern, the most important parameter for the spiral scan is the minimum available dwell time,  $t_d$ , commensurate with the designated scan limits and the available search time. Appendix M presents the detailed analysis of the relationship between the dwell time, the total scan time, and the scan rate for the following types of spiral scans:

- (1) Spiral scan with constant rotational velocity.
- (2) Spiral scan with constant tangential velocity.
- (3) Hybrid scan which starts out with a constant rotational velocity and then switches over to a constant tangential velocity.

For any given scan limit ( $\pm \theta_m$ ) and available search time ( $T_s$ ), the dwell time is a function of the beamwidth and this, in turn, depends on the antenna's dimensions. The numerical examples in Appendix M are carried out for dish diameters ranging from 20 inches to 36 inches. Figure 2 shows the relationship between the minimum dwell time  $t_d$  and the antenna dish diameter as functions of  $\theta_m$  and  $T_s$ . The data shown are for the hybrid spiral scan operating within a scan frequency range of 2 Hz to 10 Hz. The scan frequency  $f_s$  is, in this case, the constant rotational rate at the onset of the scan. The antenna servo, therefore, must be able to perform with  $f_s \geq 2$  Hz during the initial portion of the acquisition scan. After switchover to a constant tangential velocity,  $f_s$  is automatically reduced. Furthermore, after the acquisition is completed, the servo loop bandwidth can be narrowed to meet the angular tracking accuracy requirements.

Note that, as pointed out in Appendix M (see Figures 4 through 7), the  $f_s \geq 2$  Hz requirement applies only to the case of  $\theta_m = \pm 30^\circ$  and  $T_s = 30$  sec. This is to be expected because, for the latter case, the antennas have to scan the maximum angular field within the minimum allotted scan time. As a result, the  $f_s$  has to be relatively "fast" to spiral the antenna beam across the scan volume determined by the  $\theta_m$  limits.

The values of dwell time shown in Figure 2 can be used for determining the radar/communication system performance for the various modes encountered.

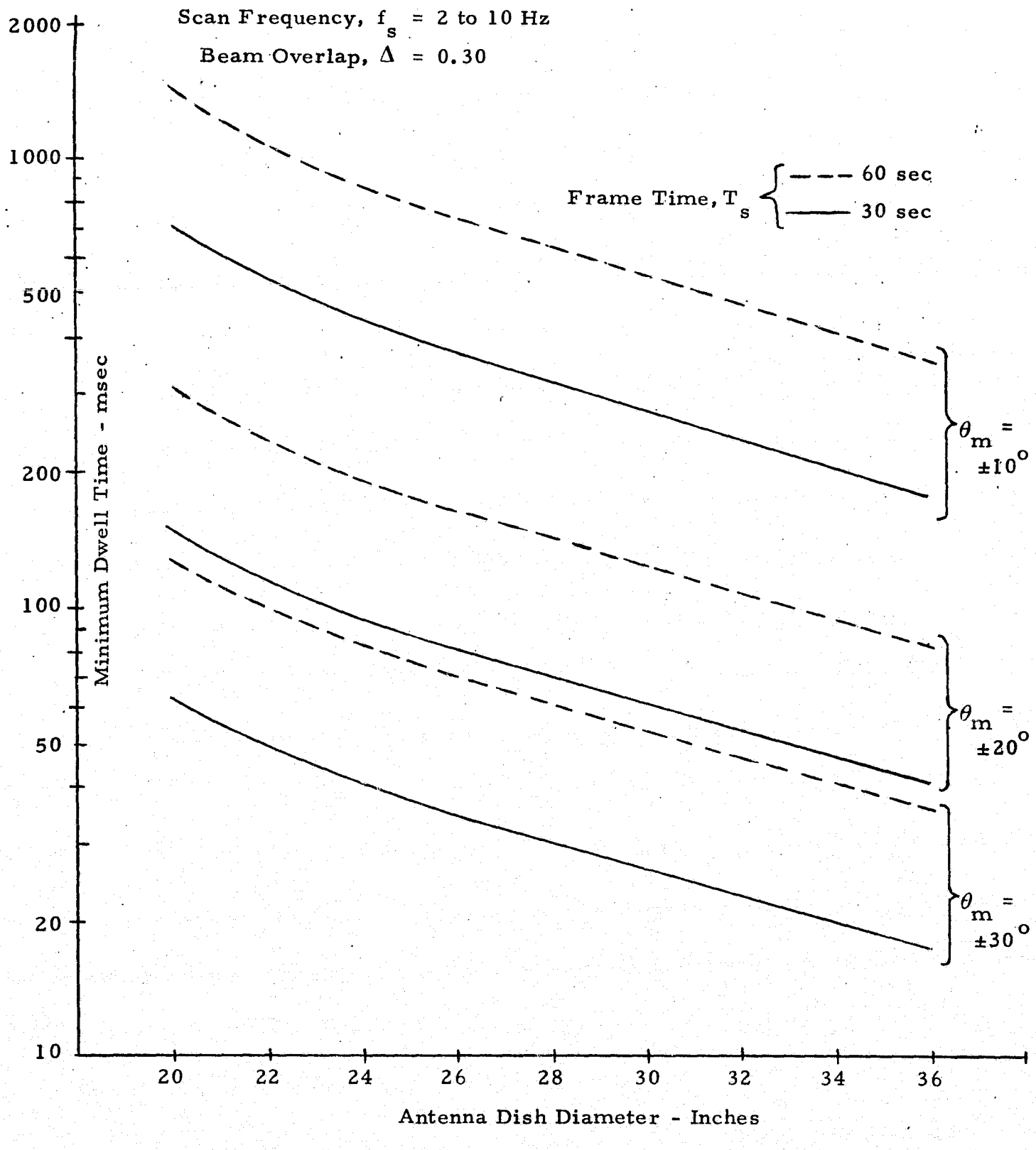


Figure 2. Minimum Dwell Time Versus Dish Diameter, Frame Time, and Maximum Scan Angle for  $f_s$  Range of 2 to 10 Hz

#### 4.0 POWER BUDGETS FOR PASSIVE TARGET DETECTION - PULSE DOPPLER RADAR

Having obtained the values for the dwell times available for the various modes of system operation, we have calculated the power budgets for passive target detection with the pulse doppler radar system (see Appendix N). The new budgets, as compared to the budgets reported in the final report for Phase I, include the following updates:

- (1) Hybrid spiral scan for angular search;
- (2) Passive target detection at 14.8 km (8 nmi).

The new power budgets also take into account such factors as variable system losses, mission-dependent parameters such as angular search limits ( $\pm \theta_m$ ), and the search frame time  $T_s$ .

Two basic mission-dependent modes are considered. These are:

- (1) Range = 22.2 km (12 nmi), search limit  $\theta_m = \pm 20^\circ$ .
- (2) Range = 14.8 km (8 nmi), search limit  $\theta_m = \pm 30^\circ$ .

In addition to these two basic modes of operation, another mode is considered in which the search limit is set at  $\pm 30^\circ$ , regardless of the range. It is shown that the latter mode imposes additional power requirements for detection at 22.2 km, particularly if the antenna dimensions are limited to a 20-inch diameter dish.

Consistent with the previously established criterion, the total detection time is assumed to be 60 seconds, the time which can be allotted either to a single scan or to two consecutive scans, each of 30 seconds duration. The total probability of detection for the 60-second interval is 0.99 and the average false alarm rate is one per hour. Centerline detection with a bank of doppler filters is used as the model for the target detector.

To make the results more general, the power requirements are estimated for several antenna sizes, ranging from 20 inches to 36 inches in diameter. Moreover, the results are presented in a format which accounts primarily for the losses associated with the pulse doppler radar

detection, and the peak power required for detection is determined in terms of all other additional total system losses. These additional system losses may consist of such terms as RF losses, field degradation, threshold loss, etc.

Figure 3 shows the relationship between the peak transmitter power required for passive target detection and the antenna dish diameter for several values of system loss. The curves shown are for a detection range of 22.2 km (12 nmi) and for a scan angle of  $\theta_m = \pm 20^\circ$ . Other pertinent parameters are as indicated in Figure 3. From this figure, it can be seen that, with a 20-inch diameter antenna dish and system losses of 5 dB, there are virtually no safety margins for satisfactory system operation for the conditions indicated. Larger dish diameters permit a more flexible tradeoff between the losses and the peak power margin. Additional detailed information for the case of  $\theta_m = \pm 20^\circ$  is given in Figure 2 of Appendix N.

For the case of  $\theta_m = \pm 30^\circ$ , the data shown in Figure 3 of Appendix N indicates that, with a 50-watt peak power limitation, detection at 22.2 km can be performed only with a 36-inch antenna if the system losses are as high as 7.5 dB. On the other hand, passive target detection at 14.8 km (8 nmi) can be accomplished with smaller dish sizes. Also, a greater flexibility exists at this range for the tradeoffs between system losses and safety margin values for the 50-watt peak power limitations.

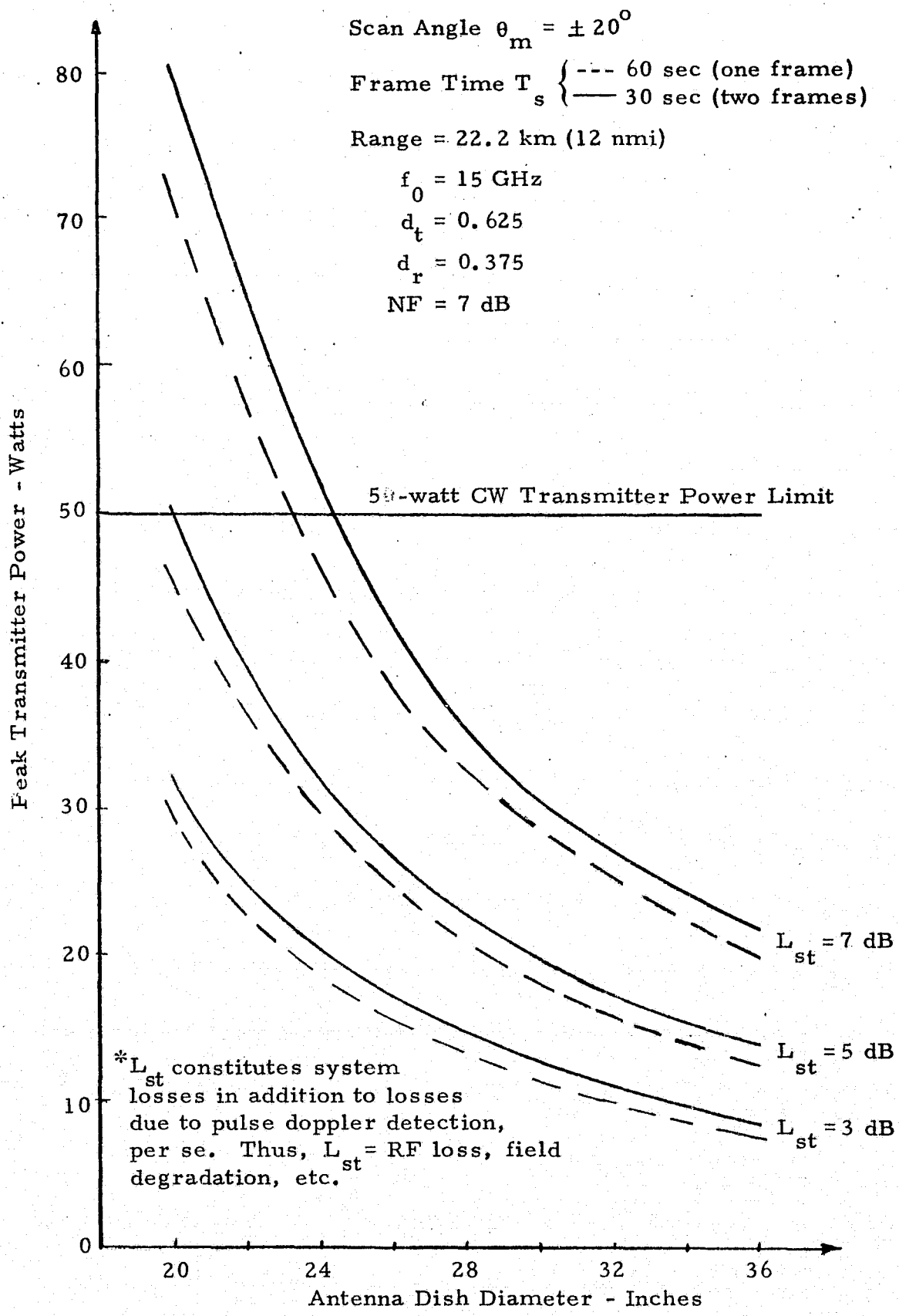


Figure 3. Peak Transmitter Power Required for Passive Target Detection vs. Antenna Dish Diameter and System Loss,  $L_{st}^*$  (Pulse Doppler System)

## 5.0 SIGNAL DESIGN CONSIDERATIONS FOR PULSE DOPPLER RADAR SYSTEM

For the pulse doppler radar system to be compatible with the 50-watt CW communication transmitter, the radar signal design must be such that the operation in all radar modes be compatible with the peak power limitation of the transmitter. This means that the average power of the radar signal can be up to 50 watts but that its peak power should not exceed this value.

The analysis of the signal design for the cooperative mode\* indicates that this peak power constraint can be met when the pulse doppler radar interrogator works with a compatible transponder. Consequently, in this report, we consider primarily the signal design for the passive mode radar operation. Appendix O presents the details of this signal design. The results are summarized below.

The operation in the passive mode can be logically subdivided into the following four modes applicable to the ranges shown:

- |                           |  |
|---------------------------|--|
| (1) Detection:            | 20.4 km (11 nmi) $\leq R \leq$ 22.2 km (8 nmi) |
| (2) Acquisition:          | 18.5 km (10 nmi) $\leq R \leq$ 20.4 km         |
| (3) Tracking:             | 2 km $\leq R \leq$ 18.5 km                     |
| (4) Short Range Tracking: | 30 m $\leq R \leq$ 2 km .                      |

(NOTE: The range division between Modes 3 and 4 is arbitrary. Also, the 22.2 km detection range requirement is the worst case.)

### 5.1 Detection Mode

In the detection mode, the driving parameter is the detection of the target with  $P_D = 0.99$  (cumulative) within a 60-second interval. The detection may be required at either 22.2 km (12 nmi) or 14.8 km (8 nmi), the former representing the worst case situation. Also, because of Swerling I

---

\* See Appendix E, Final Report (Phase I), "Study to Investigate and Evaluate Means of Optimizing the Radar Function," Axiomatix Report No. R7511-3, November 1975, under NASA Contract NAS 9-14614.

target statistics, frequency diversity is required to provide the 0.99 cumulative detection probability. In order to avoid the requirement for excessive frequency diversity gain, we assume that a two-frame (30 seconds per frame) scan with a 0.90 detection probability per scan is used to provide 0.99 cumulative probability for the 60-second detection.

To provide for nonambiguous velocity detection and subsequent readout, PRFs above 20 kHz must be used. Furthermore, to minimize the eclipsing loss, several different PRFs are used. Thus, in the passive mode, the antenna will typically scan over a  $\pm 20^\circ$  cone region starting at the 22.2 km range. Spiral scan is used and the transmit and receive duty cycle during the acquisition are 0.625 and 0.375, respectively. Detection is by means of the doppler filter bank. The PRF is cycled over four values ranging from 22.0 kpps to 31.8 kpps. The frequency is hopped over six positions separated by 50 MHz.

The corresponding time schedule of RF carrier frequencies and PRFs is shown in Figure 4. The numerical values shown are for a specific case and they vary according to the changes in the system parameters.

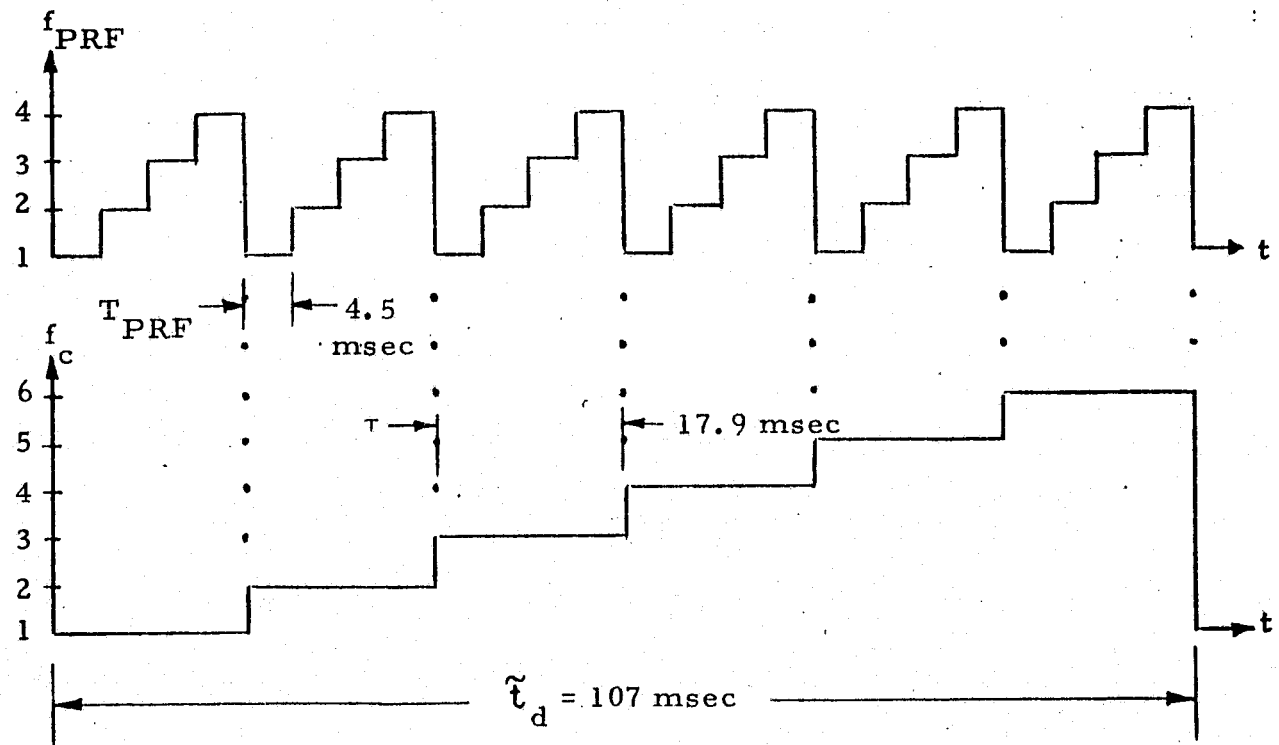
### 5.2 Acquisition Mode

Upon doppler detection, the angle acquisition and track are initiated. The frequency track and velocity readout will then commence. PRF cycling and six-step frequency diversity are still employed to reduce eclipsing and scintillation losses. The patterns are still the same as shown in Figure 4.

When the doppler (velocity) and angle acquisition are completed, the transmitter duty cycle is lowered to about 0.1 (pulse width about 3.5  $\mu$ sec) and the range acquisition and track are initiated. The velocity and range information readout commensurate with the specified accuracies are then provided at 18.5 km (10 nmi).

### 5.3 Tracking Mode

In the tracking mode, the doppler tracking continues based on the range-gated, low duty cycle information. The FRF cycling and frequency



Note: Numerical values shown are for 20" diameter dish,  $\theta_m = \pm 20^\circ$ , and the two 30-second frame scans. For other parameters, the durations of the dwells vary accordingly.

Figure 4. Time Schedule of RF Carrier Frequencies and PRFs.

diversity also continue. The transmitter pulse duration and the corresponding receiver range gate width are about 3.5 microseconds in this mode. As is shown in Appendix O, such a pulse width, combined with an average duty cycle of about 0.1, is sufficient to provide the required range and velocity information accuracies.

#### 5.4 Short Range Tracking Mode

At a range of about 2 km, the system will go into the short range mode. The pulse width is reduced to 0.1 microsecond and only the 31.8 kpps PRF is used. The signal strength is sufficient to continue accurate centerline tracking even with a much reduced duty cycle. Also, as a backup, range-differentiated  $\dot{R}$  tracking may be employed. With a pulse width of 0.1 microsecond, range tracking down to 30-meter stationkeeping positions will be possible. Frequency diversity will be retained at all ranges in the passive mode.

#### 5.5 Parameters Summary for Baseline Case

Table 1 presents a summary of the parameters for the pulse doppler system in the passive mode. Some of these parameters, however, apply only to the baseline system configuration, i.e., the 20-inch dish, and they will be different for larger dish diameters and other mission-dependent constraints. Other parameters, such as the number of RF frequencies, frequency steps, and the total frequency span, will be the same for all passive modes.

Table 1. Parameters Summary for Pulse Doppler Radar in the Passive Mode\* (Baseline Values)

Performance Characteristics

Detection Range	22.2 km ( $P_d = 0.99$ , Swerling I target)	
Acquisition Time	60 seconds	
Number of Scans	2	
Scan Duration	30 seconds	
Angular Search Coverage	$\pm 20^\circ$ cone	
Accuracy ( $1\sigma$ )	<u>Slowly varying (bias)</u>	<u>Fluctuating</u>
Range		
$R > 2$ km	5 m (all ranges)	10.5 m ( $R = 20.4$ km)
$R < 2$ km	0.14 m (all ranges)	0.04 m (all ranges)
Velocity	0.01 m/sec.	0.053 m/sec

System Characteristics (Baseline)

Operating Frequency	15 GHz	
<u>Antenna</u>		
Size	0.5 m diameter (20 inches)	
Beamwidth (one way)	$2.8^\circ$ (3 dB)	
Gain	35.4 dB	
Scan Program	Spiral	

Transmitter Characteristics

	Peak Power	PRF (kpps)	Pulse Width ( $\mu$ sec)	Duty Cycle	$P_{ave}$
Detection and Acquisition ( $18.5 \text{ km} \leq R \leq 22.5 \text{ km}$ )	50 w	22.0 - 31.8	28.4 - 19.7	0.625	31.3 w
Tracking ( $2 \text{ km} \leq R \leq 18.5 \text{ km}$ )	50 w	22.0 - 31.8	3.5	0.1(ave)	5 w
Tracking ( $30 \text{ m} \leq R \leq 2 \text{ km}$ )	50 w	31.8	0.1	0.00315	0.16 w
Number of RF Frequencies	6				
Frequency Step		50 MHz			
Total Frequency Span		250 MHz			
Dwell Time per Frequency		17.9 msec			

\* Some of these parameters will be different for other dish diameters and mission-dependent constraints.

## 6.0 GROUND RETURN ANALYSIS

The transient response of the ground return clutter was analyzed for the case of near-vertical incidence, and the relationship between the parameters influencing this response has been established. The details are given in Appendix P. The findings are consistent with the commonly established trend that the narrower pulse widths and smaller antenna beam-widths provide better clutter rejection. The use of pulse widths narrower than 0.1 microsecond may be questionable, however, because of the physical size of some of the larger targets, i.e., the 18-meter long Agena.

Sample calculations of the target power-to-clutter power ratio ( $P_s/P_c$ ) at the lowest orbital altitude of 185.3 km (100 nmi) indicate that, unless the incidence angle is restricted to a minimum value of  $10^\circ$ , there exists a possibility of clutter interfering with the passive target return at ranges as close as 2 km. The expected modes of interference are either the range gate or the doppler tracker stealing, or both, when the ground return falling in the particular tracker aperture exceeds the power of the passive target return being tracked.

Consequently, the use of ground clutter rejection techniques is recommended. The most promising method, particularly applicable to high PRF pulse doppler systems, appears to be that of frequency hopping and related variations thereof. Note that frequency hopping is required anyway for the purpose of target fluctuation reduction and, thus, the adaptation of the hopping pattern to clutter rejection should not impose excessive complications on the system design.

Specifically, the hopping pattern should be such that the radar operation is shifted to a different frequency when the ground return arrives at the receiver. The ultimate objective of the clutter rejection scheme should be to insure reliable radar operation with a passive target in all modes, including long-range detection and track initiation.

## 7.0 RADAR/COMMUNICATION SYSTEM BLOCK DIAGRAM - SUMMARIZING DESCRIPTION

The block diagram for the candidate integrated radar/communication system is shown in Figure 5. The proposed modulation for the radar mode is characteristic for coherent pulse doppler systems. In the communication mode, the transmission is either phase (Mode 1) or frequency (Mode 2) modulated. The received signal in the communication mode is phase-modulated and PN encoded to reduce its spectral density.

### 7.1 Transmitter

As shown in Figure 5, the TWTA which is used for the communication signal transmission is also used for the radar function. Assuming the radar operation is performed in the vicinity of the 15 GHz communication transmitter frequency, the transmitter bandpass filter (BPF) is connected permanently to the output of the TWTA. Such a connection will minimize the leakage of the TWTA's 13.8 GHz spur signals into the input of the communication receiver when the system is in the communication mode. During the radar mode, the CW output of the TWTA is keyed (gated) in accordance with the modulation formats required for the various modes of radar operation. Because of the relatively fast gating times required in the radar mode, a solid-state switch is used to provide signal keying. To minimize losses in the communication mode, the solid-state switch is bypassed.

In either the radar or the communication mode, the transmitted signal is fed via the rotary joint to the gimballed antenna assembly and ultimately to the feed of the main parabolic dish antenna. During the TDRS acquisition in the communication mode, the transmitter signal is temporarily switched to the widebeam horn to aid the TDRS in the detection of the Orbiter's signal.

To reduce the target signal fluctuations in the passive radar mode, transmitter frequency diversity is provided by the single sideband generator (SSG). The SSG offsets the nominal transmitter frequency by a number of preselected steps required to achieve the diversity span of 250 MHz. In the

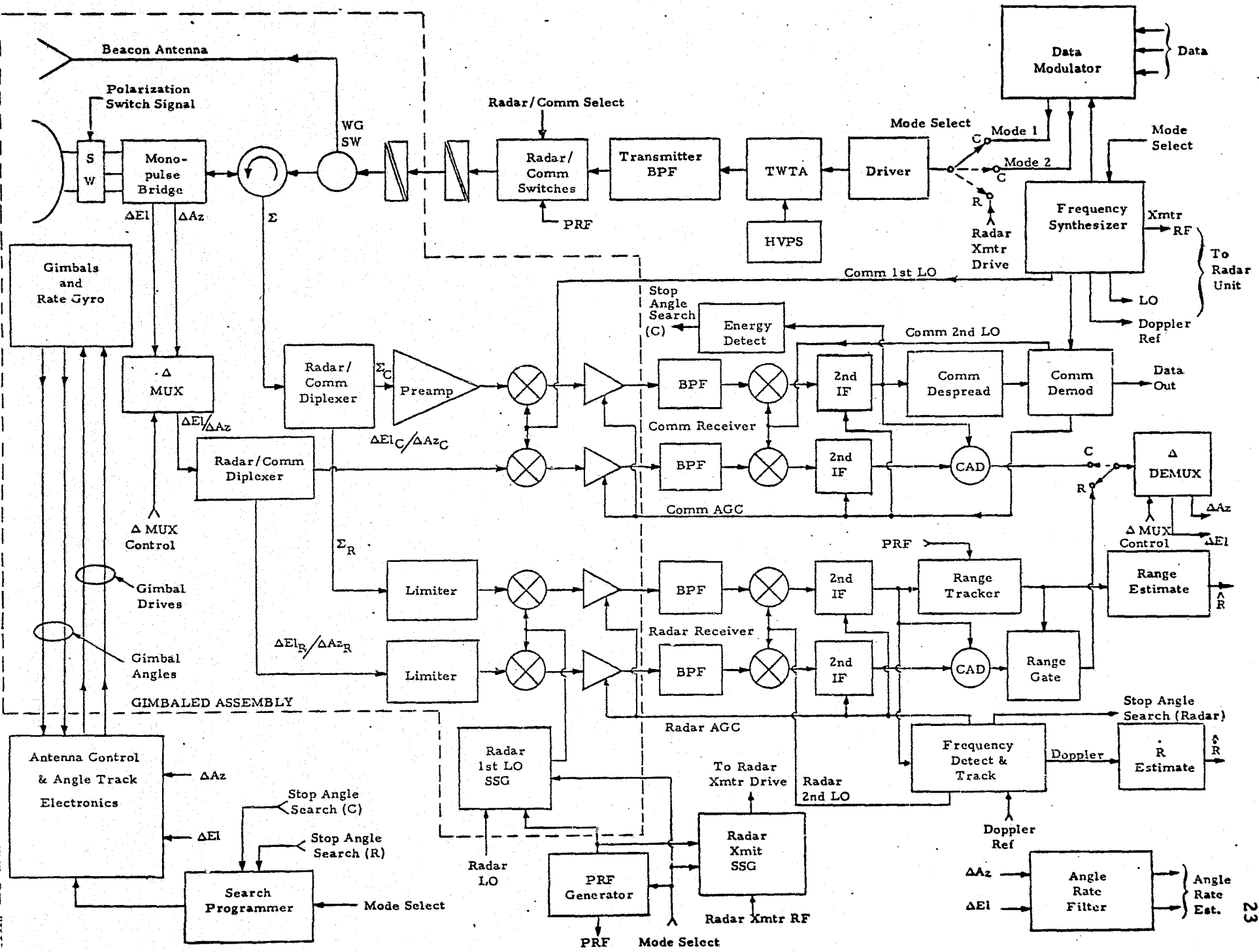


Figure 5. Block Diagram for a Candidate Integrated Radar/Communication System

cooperative (transponder-aided) mode, the transponder offsets the frequency of the return by the amount equal to the radar's first IF. Thus, in the cooperative radar mode, the transmitter and first LO signals are identical.

### 7.2 Antenna

The antenna is a parabolic dish, with a Cassegrain feed being the most likely candidate. For the radar mode, the transmit and receive polarizations are linear; for the communication mode, the simultaneous transmit and receive signals are circularly polarized. Thus, the antenna feed is designed to provide polarization selection.

The directivity pattern of the auxiliary "widebeam" ( $12^{\circ}$ ) horn is colinear with the directivity pattern of the main antenna. As explained earlier, this horn antenna is used only during the TDRS acquisition phase of the communication mode.

The received signals in both the radar and communication modes are applied to a monopulse bridge which develops the  $\Delta Az$  and  $\Delta El$  signals required for tracking. To eliminate the requirement for two separate delta receive channels, the two delta signals are time-multiplexed and thus can be handled by a single channel in both the radar and communication modes.

Antenna line-of-sight (LOS) stabilization, as well as the search and track functions required for the communication and radar modes, is performed by the Antenna Control and Angle Track assembly described in detail in Appendix L of this report.

### 7.3 Receivers

The sum channel signal and the multiplexed delta signals are applied, respectively, to two diplexer units. The function of the dippers is to separate the 15 GHz radar and the 13.8 GHz communication receive signals and to supply these signals to their respective channels. Note that the separation of the communication and radar receive functions facilitates the removal of the radar receive channel from the optional (Comm B) unit which requires only the communication function. Also note that the first

conversion is performed within the gimballed antenna assembly. This arrangement eliminates the requirement for a second rotary joint. The first LO signals are supplied to the gimballed assembly via cable wraps. Similarly, the first IF radar and communication signals are delivered to their respective second mixers via cable wraps.

Because the transmitter and LO signals for both the communication and radar modes are derived from a coherent synthesizer, the AFC is not required for the radar mode. In the passive radar mode, when frequency diversity is required, the radar's first LO signal is stepped in synchronism with the transmitted signal. A single sideband generator (SSG), similar to the one used to change the transmitter frequency, can be used for this purpose. In the cooperative radar mode, as was mentioned previously, the first LO frequency is the same as that of the transmitter.

### 7.3.1 Radar Mode

As shown in Figure 5, the two-channel radar receiver utilizes a mixer front end. To prevent receiver saturation during radar transmission, limiters are placed ahead of the first mixers. Additional isolation (if required) may be provided by gating the IF channels of the radar receiver.

The frequency detect and track unit of the radar receiver is similar to the one described in detail in Appendix G of the Phase I final report. In the passive target tracking mode, the target signal is detected by a bank of doppler filters. When the signal in one of the doppler filters exceeds a preset threshold, angular search is terminated and the frequency tracking commences. Because the passive mode coherency of the return may be destroyed by target characteristics, a discriminator and a VCO (internal to the unit) are used to perform the tracking. The output of the VCO is then compared against a fixed reference and the frequency difference caused by the doppler shift is used to estimate the range rate, i.e., the target velocity. In the cooperative mode, the transponder return is coherent and a phase-lock loop is used to acquire and track the frequency of the transponder's reply.

The range acquisition is performed by cycling the PRFs through four values to reduce eclipsing loss and to resolve the range ambiguity caused by the high values of these PRFs. The high PRF values are required to provide nonambiguous tracking of both passive and active (cooperative) target velocities. Once the range ambiguity is resolved by the application of the Chinese remainder theorem algorithm, split-gate target tracking in true range is initiated.

The sum channel of the radar receiver provides the reference signal to the coherent amplitude detector (CAD) which recovers the amplitude and polarity of the multiplexed delta error signals. These signals are then demultiplexed and applied to the angle tracking electronics unit which keeps the radar antenna pointed at the target.

### 7.3.2 Communication Mode

The communication receiver employs a preamplifier in the sum channel, thus providing an improved signal-to-noise ratio for this channel. The suppression of the 15 GHz communication transmitter signal at the receiver input is provided by the 13.8 GHz bandpass (or low pass) filtering action of the diplexers. The presence of the 15 GHz transmit signal at the inputs to the diplexers may be due to circulator leakage to the sum channel terminal and monopulse bridge leakage to the delta output terminals. As for the radar channel, the first conversion of the communication receive signal is performed within the gimballed antenna assembly.

Note that the sum and delta signals of the communication receiver carry the PN spread spectrum modulators. The PN modulation is removed from the sum channel by the communication despreader and the data are then recovered by the communication demodulator. The demodulator also performs the function of doppler search and tracking for the communication signal.

The angle tracking in the communication mode, however, is performed with an unspread signal, with the sum channel signal being the

reference input to the angle error recovery CAD. The feasibility of angle tracking with an unspread signal is supported by analysis in Appendix L.

During the TDRS search and acquisition phase, the antenna is scanned over the angular uncertainty region. When the TDRS signal is within the antenna beam, the energy of the unspread PN signal is detected and the "stop angle search" command is generated. TDRS angle track is then initiated and the PN despreader performs code search. The use of energy detection, rather than code detection, speeds up the angle search and acquisition in the communication mode.

## 8.0 CONCLUSION

Various investigations pertaining to the optimization of a rendezvous radar system design and an integrated radar/communication system configuration for the Space Shuttle have been presented in this report. Based on these investigations, a block diagram for the candidate integrated radar/communication system has been presented. The supporting analysis indicates that the radar system's performance requirements can be met with the 50-watt peak power limitation for the integrated radar/communication transmitter. Furthermore, it is shown that angle tracking subunits, which include the antenna and the associated servo controls, can be shared between the radar and the communications functions of the Ku-band equipment under consideration.

## APPENDIX L

### THE ORBITER MONOPULSE ANTENNA ANGULAR CONTROL SYSTEM

-- C. L. Weber

#### 1.0 INTRODUCTION

Various aspects of the angle tracking control system of the Ku-band communication system are considered. We verify that angle tracking of the TDRS PN spread communication signal received by the Orbiter can be carried out directly on the spread wideband waveform. Hence, PN despreading is not necessary in the angle tracking loop, thereby significantly simplifying the acquisition sequence of the TDRS waveform by the Orbiter Ku-band communication receiver.

A coherent amplitude comparison monopulse angle tracking system for the Ku-band communication signal from TDRS is proposed for the baseline system. A single channel of monopulse angle tracking is considered. The results are sufficiently optimistic, however, so as to allow more than ample safety margin for any crosstalk which may be encountered in a two-channel monopulse system. Specific characteristics of the baseline system (see Figure 1) which we propose are:

- (a) The monopulse angle tracking signal is derived directly from the PN spread received signal, with no spectrum compression and no data wipe-off;
- (b) A noncoherent AGC is used; and
- (c) A coherent amplitude phase detector (CAD) is employed to generate the angle error information. For this system, the RMS angle tracking error due to receiver front-end noise is shown to be

$$\sigma_{\Delta\epsilon} \approx 5 \times 10^{-3} \text{ degrees}$$

when the ratio of the average received power in the sum channel at bore-sight to the one-sided noise power spectral density is

$$\frac{P_{rec}}{N_0} = 73.2 \text{ dB-Hz} .$$

This result was determined when using conservative design values for the IF bandwidth, the antenna error angle gain characteristic, and the angle control system loop bandwidth.

This RMS error is very small compared to any realistic specification that is expected. This performance prediction is also more than an order of magnitude below the specification for the angle tracking of the Ku-band radar in both the skin-track and cooperative modes of operation.

In Section 2.0, the monopulse antenna control system is described in detail. The RMS error of the monopulse angle tracking system is developed in Section 3.0, and the results of numerical computations are presented in Section 4.0. The following cases are considered:

- I) No despreading and paramps in both the sum and difference channels.
- II) No despreading and a paramp in the sum channel only.

In the development of RMS error, the signal loss incurred in passing through the IF filters is taken into account.

In Section 5.0, we consider certain implementations, and in Section 6.0, the acquisition and transitions to tracking procedures are considered. In particular, operational procedures are recommended to overcome the problem of potential signal lock-up via an antenna sidelobe.

The development of effective choices of the system parameters is carried out in the Addendums.

In Addendum A, the inertial stabilization of the antenna system is considered, and the system parameters in the transfer function are determined.

The performance of the noncoherent AGC is determined in Addendum B, and in Addendum C, the noise power spectral density of the equivalent loop noise is developed.

The design points are chosen in Addendum D, from which the resulting loop gains are determined. For both of the cases described above, two design points are used, namely, an antenna angle control system loop bandwidth of 10 Hz and of 1 Hz.

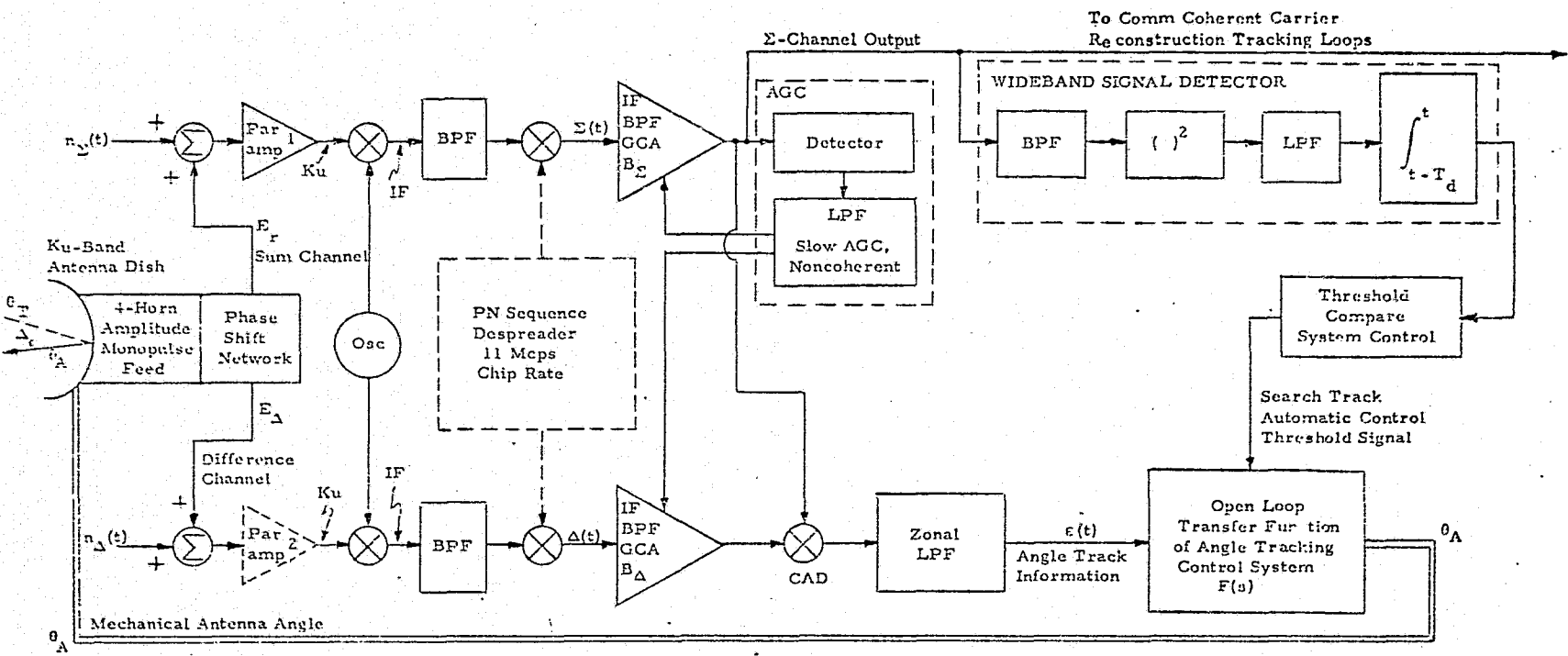
## 2.0 MONOPULSE ANTENNA SYSTEM DESCRIPTION

A system block diagram of the amplitude monopulse angle tracking system for the orbiter communication forward link is shown in Figure 1. For simplicity, only one difference channel is shown. The sum channel is designated by  $\Sigma(t)$  and the difference channel by  $\Delta(t)$ . In this part of the system evaluation, separate IF strips are assumed, although one IF could be employed by first multiplexing the azimuth and elevation angle error signals. Also shown are paramps in the sum and difference channels, and the PN sequence despreader operating on each channel. We shall determine angle tracking performance for the configuration shown, as well as with one or both paramps removed, and with the PN sequence despreader removed. The paramp in the difference channel, as well as the despreaders, are shown as dotted lines in Figure 1, since these components are not in the baseline system of the angle tracking control system. The development will be carried out for all cases, however, and we shall see that satisfactory angle tracking performance is obtained for all configurations.

With respect to the amplitude monopulse feed, sum and difference patterns of a 4-horn antenna system are usually determined experimentally in order to account for the effects of coupling between horns and of introduction of high-order transmission modes at the mouth of the horn assembly. Studies of actual parabolic antenna patterns [4-6] have shown that the normalized sum (voltage) pattern can be represented very closely by

$$E_s = \cos^2(1.18\Delta_\epsilon/\theta_B) \quad (1)$$

where  $\Delta_\epsilon$  is the angle off the boresight axis, and  $\theta_B$  is the 3 dB beamwidth. It is assumed that  $\Delta_\epsilon$  and  $\theta_B$  are given in the same units. This representation of the normalized sum pattern is excellent to well below 3 dB from the boresight axis of the main lobe and is therefore a convenient representation when evaluating antenna tracking performance. At the lower gain portions of the main lobe and over the sidelobes, the above representation is not useful.



- o All solid line components are included in our baseline configuration.
- o Dotted line components are alternatives which are considered.

Figure 1. System Block Diagram of Monopulse Angle Tracking for Orbiter Communication Forward Link (Only One Error Channel is Shown)

The measured difference (voltage) pattern for the same type parabolic antenna is well represented by

$$E_{\Delta} = 0.707 \sin(2.36 \Delta_{\epsilon}/\theta_B) \quad (2)$$

where the same comments given above apply. Differences between these approximations and actual patterns appear only at the edges of the main beam, well beyond the 3 dB beamwidth.

In the angle tracking design we are considering, as well as in most cases, only the variation within the 3 dB beamwidth is of interest, in which case the above approximations are very satisfactory. The actual error pattern is approximately linear to at least one-third of the beamwidth off the boresight. The normalized error pattern  $E_{\Delta}/E_s$  which results from the AGC operation in the receiver system (Figure 1) is linear over more than 0.6 of the beamwidth. The slope increases as the received signal approaches the half power point of the sum channel beam. The antenna error slope is designated as  $k_m$  and is approximately 1.67 for the representations given above. Within the linear region, the error voltage is

$$\text{Error Voltage} = \frac{E_{\Delta}}{E_s} = k_m (\Delta_{\epsilon}/\theta_B) \quad (3)$$

or, equivalently,

$$\Delta_{\epsilon}|_{\text{deg}} = \theta_B|_{\text{deg}}^{k_m^{-1}} \frac{E_{\Delta}}{E_s} \quad (4)$$

The actual value of the antenna error slope,  $k_m$ , varies over different monopulse antenna designs. A conservative interval is

$$1.2 \leq k_m \leq 1.9 \quad (5)$$

with typical values being  $1.55 \leq k_m \leq 1.6$ . The representation given in (1, 2) has a value of  $k_m$  equal to 1.67. In our computations, we use a somewhat more conservative value of 1.57.

## 2.1 Monopulse System Signal Descriptions

Referring again to Figure 1, the sum channel signal at the input to the sum channel IF strip is given by

$$\Sigma(t) = E_s \sqrt{2 P_{rec}} d(t) \cos(\omega_0 t + \theta_s) + n_\Sigma(t) \quad (6)$$

where  $E_s$  represents the effect of the sum of the four parts of the monopulse horn,

$\omega_0$  is the RF carrier in radians/second,

$\theta_s$  is the sum channel reference phase,

$P_{rec}$  is the average received signal power,

and  $d(t) = PRN(t) m(t)$  (7)

is the composite data signal. In (7),  $PRN(t)$  is a 11 Mcps PN sequence from an 11-stage generator. The signal is NRZ.  $m(t)$  is a 216 kbps Bi- $\phi$ -L data sequence. Both  $m(t)$  and  $PRN(t)$  fully modulate the carrier asynchronously.

The noise  $n_\Sigma(t)$  is assumed to have already been passed through an IF filter with noise bandwidth  $B_\Sigma$ . The narrowband noise [7] is represented by

$$n_\Sigma(t) = \sqrt{2} [n_1(t) \cos(\omega_0 t) + n_2(t) \sin(\omega_0 t)] \quad (8)$$

where  $n_1$  and  $n_2$  are independent zero mean Gaussian random processes; the autocorrelation functions and power spectral densities are given by

$$R_{n_\Sigma}(\tau) = 2 R_{L\Sigma}(\tau) \cos(\omega_0 \tau) \quad (9)$$

$$R_{L\Sigma}(\tau) = R_{n_1}(\tau) = R_{n_2}(\tau) \quad (10)$$

$$S_{n_\Sigma}(\tau) = S_{L\Sigma}(f - f_0) + S_{L\Sigma}(f + f_0). \quad (11)$$

These spectral densities are shown in Figure 2, in which

$N_{0\Sigma}$  = one-sided spectral density of the sum channel in watts/Hz

$B_{\Sigma}$  = noise bandwidth under the assumption of an ideal BPF, as shown in Figure 2.

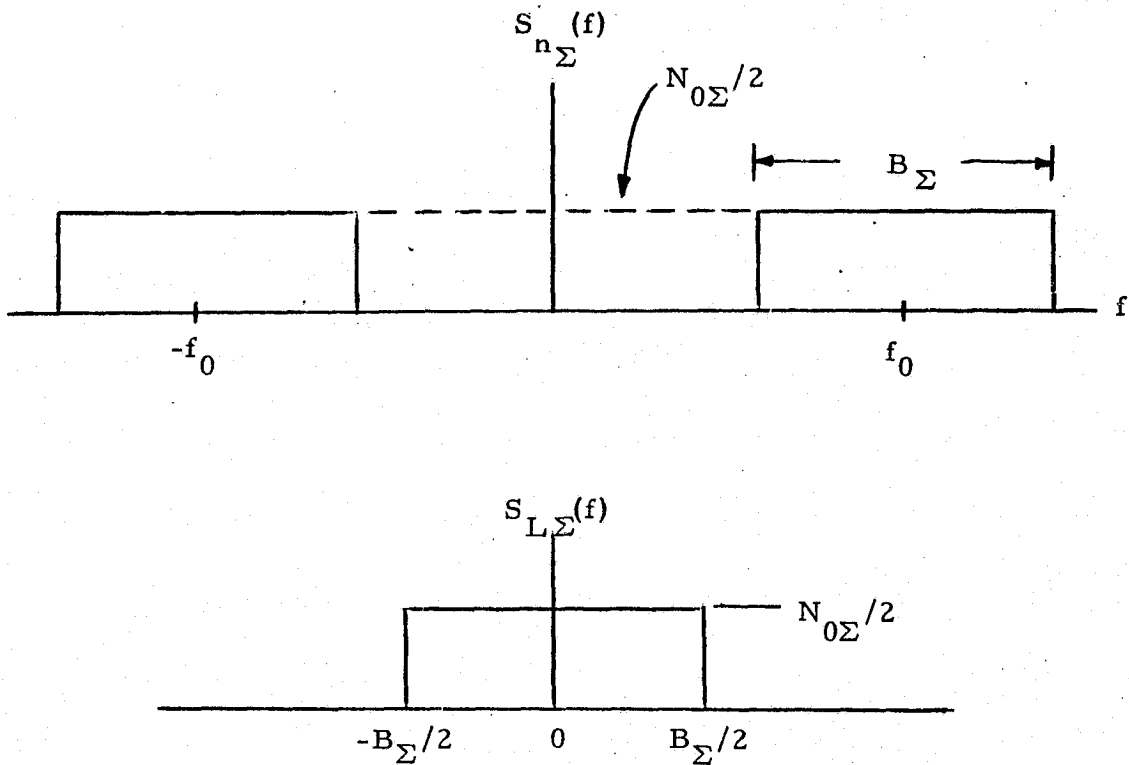


Figure 2. Sum Channel Noise Spectral Densities

The average power in  $n_1(t)$  and  $n_2(t)$  is  $N_{0\Sigma} B_{\Sigma}/2$  and the average power in  $n_{\Sigma}(t)$  is  $N_{0\Sigma} B_{\Sigma}$ .

The difference (or error) channel signal is similarly represented. In particular, at the input to the error channel bandpass filters:

$$\Delta(t) = E_{\Delta} \sqrt{2 P_{\text{rec}}} d(t) \cos(\omega_0 t + \theta_{\Delta}) + n_{\Delta}(t) \quad (12)$$

where  $E_{\Delta}$  is the difference channel error signal from the horn, and  $\theta_{\Delta}$  is the RF reference phase of the difference channel which ideally is equal to  $\theta_s$  in the sum or reference channel. The RF phase difference  $|\theta_{\Delta} - \theta_s|$  will be accounted for when evaluating performance.

The narrowband additive noise in the error channel,  $n_{\Delta}(t)$ , is modeled as

$$n_{\Delta}(t) = \sqrt{2} [n_3(t) \cos(\omega_0 t) + n_4(t) \sin(\omega_0 t)] \quad (13)$$

which is independent of  $n_{\Sigma}(t)$ . In (13),  $n_3$  and  $n_4$  are independent, and the autocorrelations and spectral densities are given by

$$R_{n_{\Delta}}(\tau) = 2 R_{L\Delta}(\tau) \cos(\omega_0 \tau) \quad (14)$$

$$R_{L\Delta}(\tau) = R_{n_3}(\tau) = R_{n_4}(\tau) \quad (15)$$

$$S_{n_{\Delta}}(f) = S_{L\Delta}(f - f_0) + S_{L\Delta}(f + f_0). \quad (16)$$

The spectral shape is the same as the sum channel in Figure 2, with the exception that the one-sided spectral density is  $N_{0\Delta}$  watts/Hz instead of  $N_{0\Sigma}$  watts/Hz, and the bandwidth is  $B_{\Delta}$  instead of  $B_{\Sigma}$ . The average power in  $n_3(t)$  and  $n_4(t)$  is  $N_{0\Delta} B_{\Delta}/2$  and the average power in  $n_{\Delta}(t)$  is  $N_{0\Delta} B_{\Delta}$ . This additional parameterization allows us to account for different noise levels in the sum and difference channels due to the presence or absence of the paramps.

Referring to Figure 1, both  $\Sigma(t)$  and  $\Delta(t)$  are passed through identically shaped IF bandpass filters with noise bandwidth  $B_{\Sigma}$  and  $B_{\Delta}$ , which are sufficiently large for us to assume that there is no signal distortion. These BPFs have gain controlled amplifiers, and we designate their gain as

$$\text{IF Gain} = \frac{1}{A_{GCA}}. \quad (17)$$

We consider the effects of the AGC on these IF amplifiers in Addendum B. Under the assumption of an ideal AGC from a noncoherent energy detector, we show that

$$(A_{GCA})^2 = E_s^2 P_{rec} + 2 R_{L\Sigma}(0) = E_s^2 P_{rec} + N_{0\Sigma} B_{\Sigma}. \quad (18)$$

The output of the coherent amplitude detector (CAD), also a phase detector, after being passed through a zonal low pass filter, is designated as  $\epsilon(t)$ , which is the angle error signal in the single channel system we are considering. This dynamic angle error is

$$\begin{aligned}
 \epsilon(t) &\triangleq \frac{\Delta(t)\Sigma(t)}{\left[A_{GCA}\right]^2} \Bigg|_{\substack{\text{Low} \\ \text{Pass}}} \\
 &= \left(\frac{1}{A_{GCA}}\right)^2 \left\{ \left[ E_\Delta \sqrt{2 P_{rec}} d(t) \cos(\omega_0 t + \theta_\Delta) + n_\Delta(t) \right] \right. \\
 &\quad \left. \cdot \left[ E_s \sqrt{2 P_{rec}} d(t) \cos(\omega_0 t + \theta_s) + n_\Sigma(t) \right] \right\} \\
 &= \left(\frac{1}{A_{GCA}}\right)^2 \left\{ E_\Delta E_s P_{rec} \cos \theta_E + n'_{eq}(t) \right\} \quad (19)
 \end{aligned}$$

where the difference in IF phase delays between the sum and difference channels is

$$\theta_E = \theta_\Delta - \theta_s \quad (20)$$

and the equivalent additive noise is given by

$$\begin{aligned}
 n'_{eq}(t) &= n_1(t)n_3(t) + n_2(t)n_4(t) \quad \left. \right\} N \times N \text{ terms} \\
 &\quad + \sqrt{P_{rec}} E_\Delta d(t) [(\cos \theta_\Delta) n_1(t) - (\sin \theta_\Delta) n_2(t)] \\
 &\quad + \sqrt{P_{rec}} E_s d(t) [(\cos \theta_s) n_3(t) - (\sin \theta_s) n_4(t)] \quad \left. \right\} S \times N \text{ terms} \quad (21)
 \end{aligned}$$

The terms in  $n'_{eq}(t)$  are designated as noise  $\times$  noise ( $N \times N$ ) terms and signal  $\times$  noise ( $S \times N$ ) terms as indicated in (21).

There may be some question as to whether the output of the CAD can truly be represented as the mathematical product of the two input waveforms when both inputs are broadband. In this case, with the despreaders absent, the bandwidth of each channel is  $B_\Sigma = B_\Delta = 40$  MHz, and with the

despreaders present in both channels, the bandwidth is approximately  $B_{\Sigma} = B_{\Delta} = 0.9 \text{ MHz}$  (216 kbps data rate bi-Φ-L signal). In all cases, there is no spectral component in either signal. To our knowledge, if the signal level of one of the inputs is kept substantially higher than the other, say by a factor of 10, then the CAD will act as an ideal multiplier independent of the bandwidth of either input waveform.

From (19), the angle error signal may be expressed as

$$\begin{aligned}
 \epsilon(t) &= \frac{\frac{E_{\Delta} E_s P_{\text{rec}} \cos \theta_E}{(A_{\text{GCA}})^2} + \frac{n'_{\text{eq}}(t)}{(A_{\text{GCA}})^2}} \\
 &= \frac{\frac{E_{\Delta} E_s P_{\text{rec}} \cos \theta_E}{E_s^2 P_{\text{rec}} + N_0 \Sigma B_{\Sigma}} + \frac{n'_{\text{eq}}(t)}{(A_{\text{GCA}})^2}} \\
 &= \frac{E_{\Delta}}{E_s} \left[ \frac{\cos \theta_E}{1 + \frac{N_0 \Sigma B_{\Sigma}}{E_s^2 P_{\text{rec}}}} \right] + \frac{n'_{\text{eq}}(t)}{(A_{\text{GCA}})^2} \\
 &= k_m \frac{\Delta \epsilon}{\theta_B} \left[ \frac{\cos \theta_E}{1 + \frac{N_0 \Sigma B_{\Sigma}}{E_s^2 P_{\text{rec}}}} \right] + \frac{n'_{\text{eq}}(t)}{(A_{\text{GCA}})^2} \\
 &= K_{\text{eq}} [\Delta \epsilon + n'_{\text{eq}}(t)] \tag{22}
 \end{aligned}$$

where

$$K_{\text{eq}} = \frac{k_m}{\theta_B} \left[ \frac{\cos \theta_E}{1 + \frac{N_0 \Sigma B_{\Sigma}}{E_s^2 P_{\text{rec}}}} \right] \tag{23}$$

and  $n'_{\text{eq}}(t) = K_{\text{eq}}^{-1} (A_{\text{GCA}})^{-2} n'_{\text{eq}}(t)$  . (24)

The amplitude sensing monopulse antenna control system has been described. This baseline system includes

- (a) amplitude sensing
- (b) noncoherent AGC
- (c) coherent amplitude detector (CAD).

We now calculate the tracking performance by predicting RMS error.

### 3.0 MONOPULSE SYSTEM TRACKING PERFORMANCE - RMS ERROR

A block diagram of the linearized antenna angle control system is shown in Figure 3, where

$\theta_T$  = angle to target with respect to an inertial reference

$\theta_A$  = antenna angle with respect to an inertial reference

$$\Delta\epsilon = \theta_T - \theta_A$$

$\epsilon_n(t) = \Delta\epsilon + n_{eq}(t)$  = normalized error signal

$\epsilon(t) = K_{eq} \epsilon_n(t)$  = the angle error signal after the AGC action  
which is the input to the open loop antenna angle con-  
trol system transfer function

and

$F(s)$  = the open loop antenna transfer function including  
inertial stabilization which is developed in Adden-  
dum A of this report. From Addendum A, it is  
shown that

$$F(s) = \frac{K_L}{s[1 + b_1 s + b_2 s^2]} \quad (25)$$

where

$K_L$  = loop gain

$b_1 = 0.045016$

$b_2 = 0.001013$

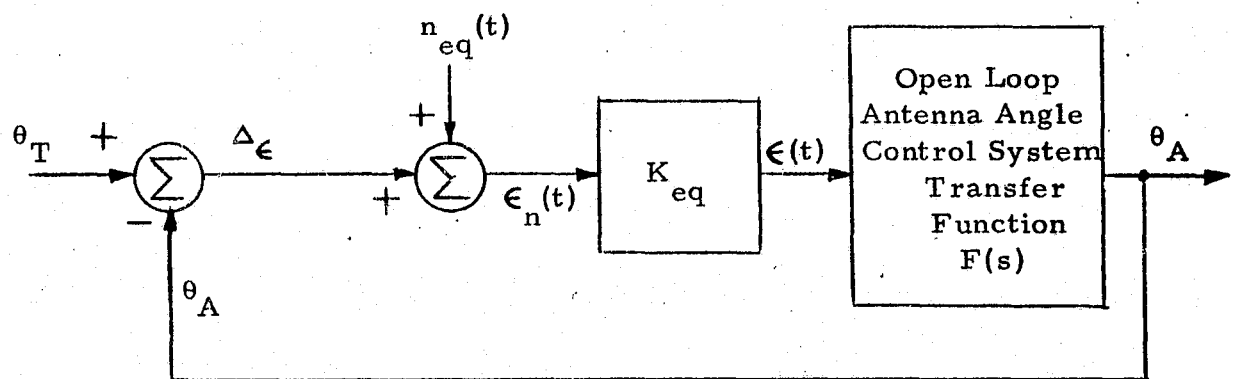


Figure 3. Linearized Diagram for Antenna Angle Control

From linear tracking loop theory [8], the variance of the angle error due to thermal noise is given by

$$\sigma_{\Delta\epsilon}^2 = \int_{-\infty}^{\infty} H_a(f)^2 S_{n_{eq}}(f) df \quad (26)$$

where  $H_a(f)$  is the closed loop transfer function of the monopulse antenna angle control system in Figure 3 and  $S_{n_{eq}}(f)$  is the two-sided spectral density of equivalent loop noise.

When the bandwidth of the noise is very large with respect to the noise bandwidth of the antenna angle control, the variance of the angle error is given by

$$\sigma_{\Delta\epsilon}^2 = N_{eq} B_a \quad (27)$$

where  $N_{eq}$  is the one-sided spectral density of the equivalent loop noise  $n_{eq}(t)$  and  $B_a$  is the one-sided noise bandwidth of the angle control loop:

$$B_a \triangleq \int_0^{\infty} |H_a(f)|^2 df. \quad (28)$$

Equivalently stated, the requirement is  $B_a \ll B_{\Sigma}$ , and  $B_a \ll B_{\Delta}$ . This is clearly the case here since  $B_{\Delta}$  and  $B_{\Sigma}$  are of the order of megahertz, while  $B_s$  is of the order of hertz.

From (24), the one-sided spectral density of  $n_{eq}(t)$  is given in terms of that of  $n'_eq(t)$  by

$$N_{eq} = \frac{N'_{eq}}{K_{eq}^2 (A_{GCA})^4}. \quad (29)$$

In Addendum C, we show that the one-sided spectral density of  $n'_eq(t)$  is given by

$$N'_{eq} = P_{rec} N_{0\Sigma} \left[ \frac{N_{0\Sigma} B_{\Sigma}}{2 P_{rec}} + \left( \frac{N_{0\Delta}}{N_{0\Sigma}} \right) \left( \frac{N_{0\Delta} B_{\Delta}}{2 P_{rec}} \right) + \gamma E_s^2 \left( \left( \frac{E_{\Delta}}{E_s} \right)^2 + \frac{N_{0\Delta}}{N_{0\Sigma}} \right) \right]. \quad (30)$$

where  $\gamma = 0.81$  when the PN sequence despreader is absent and  $\gamma = 1$  when the despreader is present.

Upon substituting (30) into (29), and (18), (23), and (29) into (27), the RMS angle error due to thermal noise is given by

$$\begin{aligned}
 \sigma_{\Delta\epsilon} &= [N_{eq} B_a]^{1/2} \\
 &= \frac{[N'_{eq} B_a]^{1/2}}{K_{eq} (A_{GCA})^2} \\
 &= \frac{\theta B}{k_m \cos \theta E} \left( \left( \frac{N_{0\Sigma} B_a}{P_{rec}} \right) \left[ \frac{N_{0\Sigma} B_\Sigma}{2 P_{rec}} \right. \right. \\
 &\quad \left. \left. \times \left\{ 1 + \left( \frac{N_{0\Delta}}{N_{0\Sigma}} \right)^2 \left( \frac{B_\Delta}{B_\Sigma} \right) \right\} + \gamma \left\{ \left( \frac{E_\Delta}{E_s} \right)^2 + \frac{N_{0\Delta}}{N_{0\Sigma}} \right\} \right] \right)^{1/2} \text{ radians} \\
 &\quad (31)
 \end{aligned}$$

where we have consolidated  $E_s$  into  $P_{rec}$  by setting  $E_s = 1$ .

The received power and AGC also affect the closed loop noise band width,  $B_a$ , of the antenna control system. This variation is determined in Addendum D, where a nominal value of  $B_a = 10$  Hz is chosen as a design point at  $P_{rec}/N_{0\Sigma} = 73.2$  dB-Hz. The other values chosen at the design point are based on most recent available circuit margin information [3], and on design values arrived at in other sections of this report. In Addendum D, we show that

$$B_a = \frac{K}{4} [1 - 0.0025K]^{-1}; \quad K < 44.4 \quad (32)$$

where the open loop gain is given by

$$K = K_{eq} K_L. \quad (33)$$

The restriction on  $K$  keeps the closed loop poles in the left half s-plane.

The gain  $K_L$  is a fixed amplifier gain, which is designed to be equal to

$K_L = 1.622$  in Addendum D. The equivalent loop gain  $K_{eq}$  is given by (23).

The variation of  $B_a$  with respect to  $P_{rec}/N_{0\Sigma}$  is discussed in Addendum D.

For small values of K,  $B_a \approx K/4$ , which agrees with the noise bandwidth for a first order tracking loop.

#### 4.0 COMPUTATIONS

The RMS phase error due to thermal noise as given in (31) has been evaluated under various conditions, including the present baseline configuration.

The constants used in the computation are:

##### 1. Tracking Loop Bandwidth

$$B_a = 10 \text{ Hz}$$

at design point 1, as discussed in Addendum D. This is considered a relatively conservative value since the angular motion of the Orbiter Vehicle with respect to the TDRS is expected to be very small.

##### 2. 3 dB Antenna Beamwidth

$$\theta_B = 2.8 \text{ degrees}$$

Using the rule-of-thumb

$$\theta_B \approx 70 \lambda / D \quad (34)$$

for paraboloid (circular aperture) antenna dishes, where  $\lambda$  = RF wavelength and  $D$  = antenna diameter, if we set

$$\lambda = 0.02 \text{ m} \quad (f_0 = 15 \text{ GHz}) \quad (35)$$

and  $D = 20 \text{ inches}$ , (36)

then  $\theta_B = 2.8 \text{ degrees}$ . (37)

A diameter of 20 inches is the smallest dish of those being considered for the baseline system. If the system can be shown to perform satisfactorily for the 20 inch dish, the larger dishes will have better tracking performance.

3. We shall assume that the paramp improves the noise figure by 6 dB with respect to RF balanced diode mixers at Ku-band. This agrees well with [9, Ch. 5]. Typical noise figures for paramps at Ku-band are 2-3 dB and 6-8 dB for balanced diode mixers at Ku-band.

4. Based on the discussion above, and in Addendum C, the IF filter bandwidth is chosen to be

30.78 MHz for the PN spread waveform

0.864 MHz for the despread waveform .

5. The antenna error slope is set at

$$k_m = 1.57 \quad (38)$$

which is in the center of the interval of typical values for circular apertures.

6. The initial computations are performed assuming the RF phase delay of the error channel with respect to the sum channel is  $\theta_E = 0$ . The effect of  $\theta_E$  on RMS angle error is considered later.

7. The ratio of  $E_\Delta/E_s$  is bounded by its maximum value of  $|E_\Delta/E_s| = 1$ .

With these constants, the RMS angle error shown in Figure 4 versus the sum channel  $P_{rec}/N_{0\Sigma}$  either at the input to the paramp or at the input to the balanced diode mixer, if the paramp is not in the tracking loop.

Considering the performance curves individually, we note the following:

Case I. This performance curve assumes the same noise figures in all channels. It also assumes that no despreading takes place in the angle tracking loop. Therefore,

$$B_\Delta = B_\Sigma = 30.78 \text{ MHz}$$

$$N_{0\Delta} = N_{0\Sigma}$$

$$\gamma = 0.81 \quad (\text{See Equation (31) and Addendum C.}) \quad (39)$$

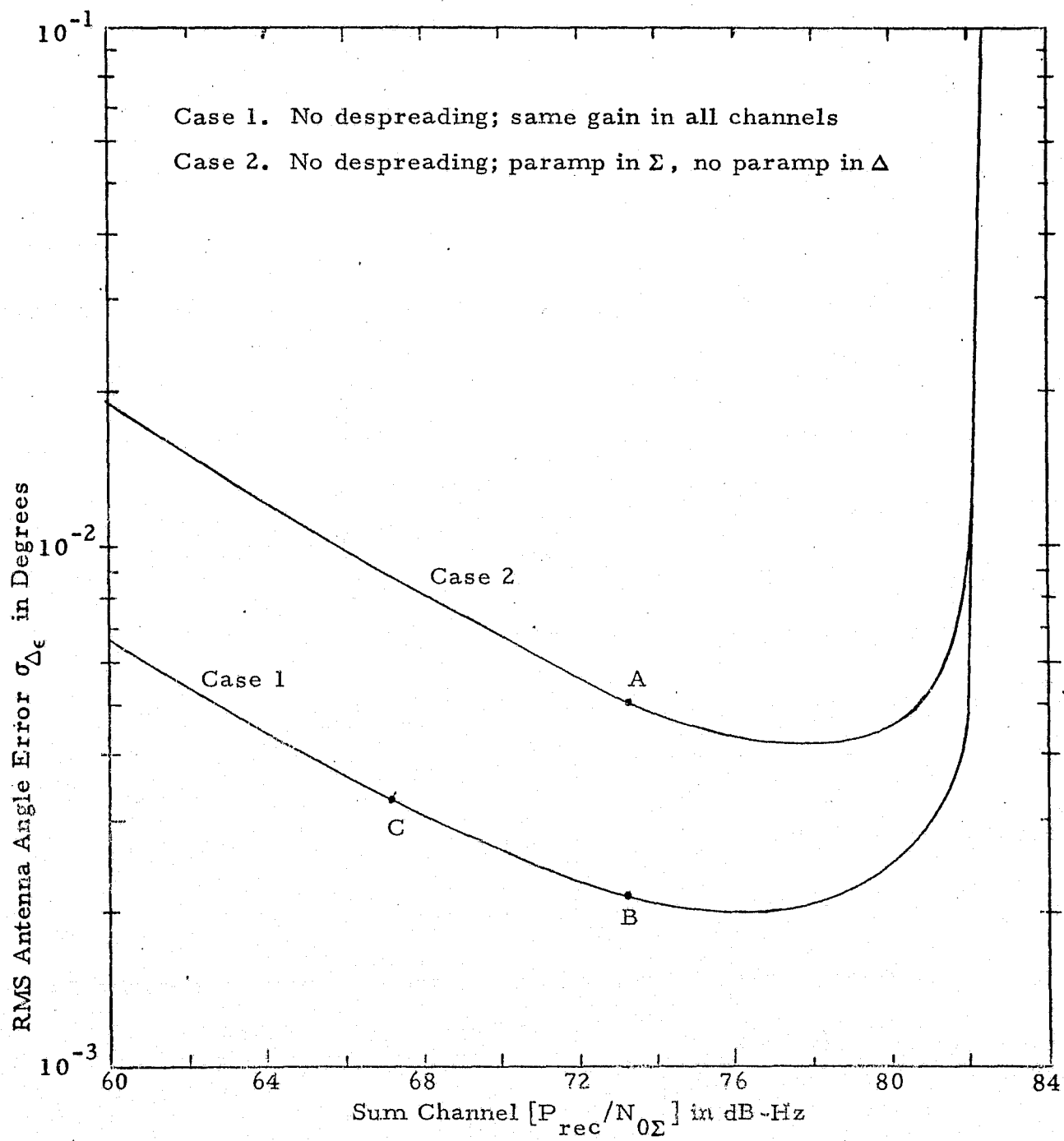


Figure 4. - RMS Angle Error Versus  $P_{\text{rec}}/N_{0\Sigma}$

Point B of Case I is at  $P_{rec}/N_{0\Sigma} = 73.2 \text{ dB-Hz}$ , which is the presently quoted value [3] when the paramp is present. Point B therefore represents the predicted performance when a paramp is present in all channels (difference, as well as sum), and there is no PN despreading of the signal.

Alternately, if there is no paramp present in any of the three channels the performance is predicted by Point C when there is no despreading. This corresponds to  $P_{rec}/N_{0\Sigma} = 67.2 \text{ dB-Hz}$ , or 6 dB-Hz lower than Point B.

Any alterations in the present power budget could easily be taken into account by choosing the appropriate values of  $P_{rec}/N_{0\Sigma}$ .

The present system configuration has two modes of operation [1-2].

Mode 1. Normal operation, in which

$$\frac{P_{rec}}{N_{0\Sigma}} = 73.2 \text{ dB-Hz}$$

under the assumption the paramp is present in the sum channel. This corresponds to a value of 48 dBW for the EIRP from TDRS, which could be as low as 43 dBW.

Mode 2. S-Band Aided [2, p. 44-45], in which the EIRP could be as low as 39 dBW during acquisition. This would lower the carrier-to-noise ratio to

$$\frac{P_{rec}}{N_{0\Sigma}} = 64.2 \text{ dB-Hz}.$$

It is clear from the performance curves in Figure 4, that the system will angle track very effectively in both modes of operation.

The most striking characteristic of the performance curves in Figure 4 is the fact that the RMS phase error bottoms out. This is a result of the fact that we are operating with a third-order tracking loop which is not compensated in the main loop. Recall from Addendum A that the inertial stabilization inner loop is designed to have critically damped closed loop poles. This inner loop is independent of the gain and

the signal-to-noise ratio in the outer loop. The outer loop is not compensated. As pointed out in Addendum D, if the loop gain,  $K = K_L K_{eq}$ , becomes greater than  $\approx 44.4$ , the closed loop poles move into the right-half plane.

The gain at which this occurs can be significantly increased if a lead-lag network were placed in front of the gyro torquer (see Addendum A).

In the present configuration without compensation, as the signal-to-noise ratio is increased, the loop gain increases. This occurs because the noncoherent AGC is not effective at the low IF signal-to-noise ratios (less than 0 dB) we incur in this system. At low gain, the bandwidth increases linearly (see Figure D-3 in Addendum D). At higher values of  $P_{rec}/N_{0\Sigma}$ , due to the operation of the third-order loop, the gain increases at rates much faster than linearly, as can be observed from the Design Point 1 curve in Figure D-3. This increases at a rate higher than  $(P_{rec}/N_{0\Sigma})^{-1}$ , which reduces the RMS phase error. The net effect is that the RMS phase error reaches a minimum at about 77 dB-Hz for Case I in Figure 4.

Again, this situation can be resolved by proper compensation of the transfer function of the angle control system.

If Design Point 2 (see Addendum D) is used in Case I, so that  $B_a = 1 \text{ Hz at } P_{rec}/N_{0\Sigma} = 73.2 \text{ dB-Hz}$ , then the RMS phase error is

$$\sigma_{\Delta\epsilon} = 0.00069 \text{ degrees ,} \quad (40)$$

which is much smaller than the 10 Hz of Design Point 1. This is to be expected.

It should be noted that RMS phase error is well below any expected specification throughout the anticipated range of sum channel  $P_{rec}/N_{0\Sigma}$ .

The key recommendation is that a lead-lag compensation network be added to the antenna angle control system to avoid this instability at high values of  $P_{rec}/N_{0\Sigma}$ .

Case II. Here again, there is no PN sequence despreading. In this case, a paramp is in the sum channel and no paramp is present in the difference channels. This corresponds to the present baseline configuration, as shown in Figure 1. For Case II,

$$B_{\Delta} = B_{\Sigma} = 30.78 \text{ MHz}$$

$$\frac{N_{0\Delta}}{N_{0\Sigma}} = 4 \quad (6 \text{ dB})$$

$$Y = .081 \quad (41)$$

Point A on the Case II curve corresponds to the present design point of the present baseline configuration, namely,

$$P_{\text{rec}}/N_{0\Sigma} = 73.2 \text{ dB-Hz} \quad (42)$$

At Design Point 2 ( $B_a = 1 \text{ Hz}$  at  $P_{\text{rec}}/N_{0\Sigma} = 73.2 \text{ dB-Hz}$ ), for Case II,

$$\sigma_{\Delta_e} = 0.00159 \text{ degrees},$$

at  $P_{\text{rec}}/N_{0\Sigma} = 73.2 \text{ dB-Hz}$ .

We see that Case II is also well below any anticipated angle tracking specification, provided we keep the signal-to-noise ratio below that which would put the system into oscillation.

It can be seen that all design points that have been considered have an RMS angle error substantially less than  $10^{-2}$  degrees.

One might ask why the RMS angle error due to thermal noise is so small. The reason is that the  $P_{\text{rec}}/N_{0\Sigma}$  (signal power to noise spectral density) is very large because of the requirements due to the wideband digital signal. The result is an abundance of signal-to-noise ratio for angle tracking purposes.

Finally, it should be noted that if the noise did go identically to zero, then

$$K_{\text{eq}} \rightarrow \frac{k}{\theta_B} \cos \theta_E = \text{constant}$$

from which we would find that

$$\frac{B}{a} = \text{constant}$$

and the RMS phase error would indeed go to zero. This would be the case, and in addition instability would not be a problem, because in this ideal situation, the noncoherent AGC is now operating on signal only, and therefore performs ideally.

The PN sequence despread cases were not plotted in Figure 4. The reason is that when the assumption is made that the angle tracking loop locks up either after, or simultaneously with, the PN despreader, the resulting gain is sufficiently high that the present angle tracking configuration becomes unstable at the design point of  $P_{\text{rec}}/N_{0\Sigma} = 73.2 \text{ dB-Hz}$ . The despread case must necessarily have compensation before additional computations can be made.

Finally, it is highly unlikely that  $P_{\text{rec}}/N_{0\Sigma}$  is suddenly going to increase by 10 dB at any time. This provides good reason to operate the antenna angle control system in its present uncompensated baseline configuration and operate directly on the received spread waveform from TDRS.

#### Effect of RF Phase Error

In order to obtain a measure of additional RMS angle error due to RF phase differences between sum and error IF channels, we compute

$$\sigma_0 \triangleq [\cos \theta_E]^{-1} \quad (43)$$

which is plotted in Figure 5. Because of the  $\cos \theta_E$  function, the effect on RMS angle error is very small for  $|\theta_E|$  less than 20 degrees.

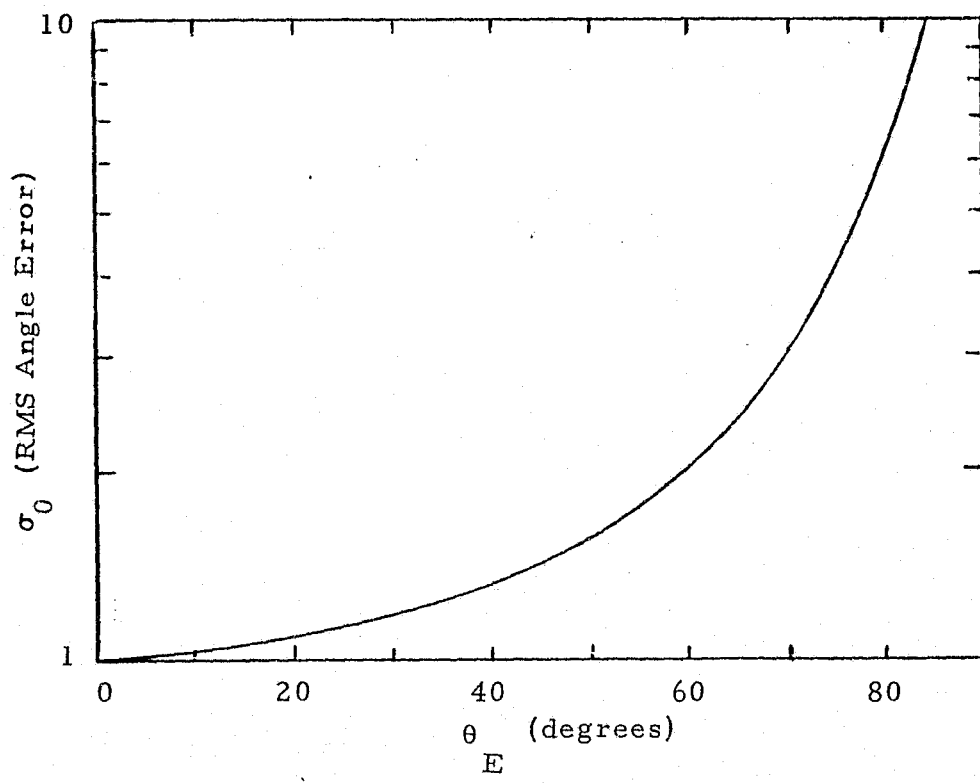


Figure 5. Angle Error Versus RF Phase Difference Between Sum and Error IF Channels

## 5.0 IMPLEMENTATION CONSIDERATIONS

The above system performance evaluation was carried out under the assumption that there are three separate IF channels for the angle tracking loops.

One possible alternative implementation which has also been proposed for the Japanese Broadcast Satellite is shown in Figure 6.

The two error channels are multiplied by PN sequences which are either different sequences or shifted versions of the same sequence. The outputs of these mixers are then added and combined with part of the power from the sum channel, which in turn is processed by a single IF strip which will have a somewhat wider bandwidth. At the end of the IF amplification strip, the signals are demultiplexed in the same manner in which they were multiplexed. The coherent amplitude detection is then carried out in each channel.

More quantitatively, the input to the single channel IF is

$$x(t) = \Sigma(t) + PRN_E(t) \Delta_E(t) + PRN_A(t) \Delta_A(t) , \quad (44)$$

where the sum channel signal is described by (6) and each error channel is described by (12).

Considering the azimuth channel only:

$$\begin{aligned} y_A(t) &= x(t) PRN_A(t) \\ &= \Delta_A(t) + \Sigma(t) PRN_A(t) + \Delta_E(t) PRN_E(t) PRN_A(t) \\ &= \Delta_A(t) + \Sigma(t) PRN_A(t) + \Delta_E(t) PRN'_E(t) \end{aligned} \quad (45)$$

where

$$PRN'_E(t) = PRN_E(t) PRN_A(t) \quad (46)$$

is a shifted version of  $PRN_E(t)$ .

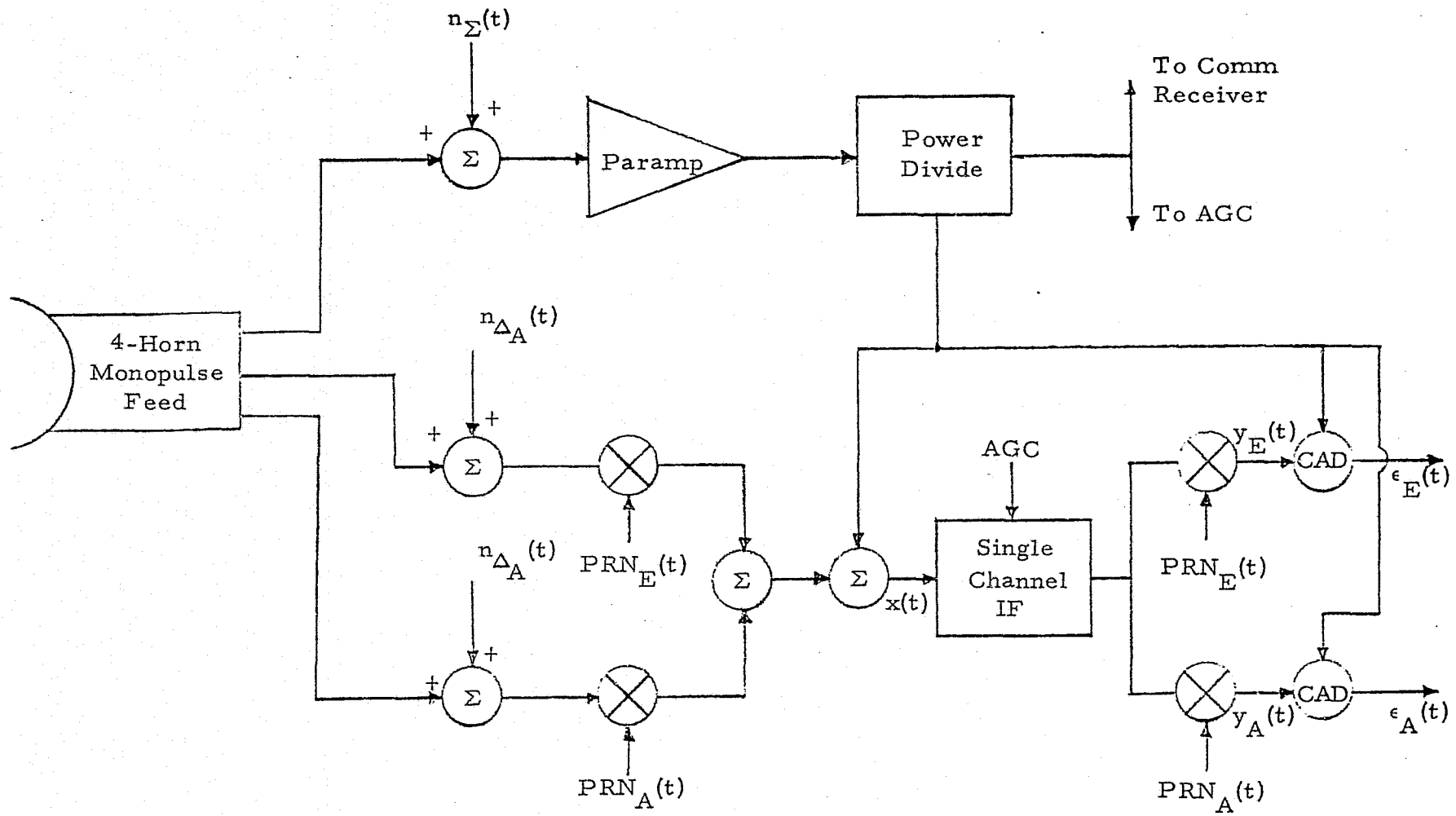


Figure 6. One Possible Single Channel IF Implementation of Communication Angle Track From TDRS

The output of the CAD for the azimuth channel is then given by

$$\epsilon_A(t) = \Delta_A(t) \Sigma(t) + [\Sigma(t)]^2 PRN_A(t) + \Delta_E(t) \Sigma(t) PRN'_E(t) . \quad (47)$$

The first term in (47) is the desired output, as given by (19). The remaining two terms are additional noise (self-noise and cross-modulation) terms which resulted from the multiplexing and demultiplexing operations, so as to implement a single IF strip.

Neglecting the effect of the AGC, the low frequency portion of  $\epsilon_A(t)$  in (47) is given by

$$\begin{aligned} \epsilon_A(t) &= E_{\Delta_A} E_r P_{rec} \\ &\quad + n_1(t) n_3(t) + n_2(t) n_4(t) \quad \left. \right\} 1 \\ &\quad + \frac{E_{\Delta A}}{\sqrt{2}} [A_c d_c(t) n_1(t) + A_s d_s(t) n_2(t)] \quad \left. \right\} 2 \\ &\quad + \frac{E_r}{\sqrt{2}} [A_c d_c(t) n_3(t) + A_s d_s(t) n_4(t)] \quad \left. \right\} 3 \\ &\quad + PRN_A(t) \left\{ E_r^2 P_{rec} + n_1^2(t) + n_2^2(t) \right. \\ &\quad \quad \left. + \sqrt{2} E_r [A_c d_c(t) n_1(t) + A_s d_s(t) n_2(t)] \right\} \\ &\quad + PRN'_E(t) \left\{ E_{\Delta E} E_r P_{rec} + n_1(t) n_5(t) + n_2(t) n_6(t) \right. \\ &\quad \quad \left. + \frac{E_{\Delta E}}{\sqrt{2}} [A_c d_c(t) n_1(t) + A_s d_s(t) n_2(t)] \right\} \\ &\quad + \frac{E_r}{\sqrt{2}} [A_c d_c(t) n_5(t) + A_s d_s(t) n_6(t)] \quad \left. \right\} 4 \end{aligned} \quad (48)$$

where  $n_5(t)$  and  $n_6(t)$  have the same statistics as  $n_3(t)$  and  $n_4(t)$ , and we have assumed two channels of data. All noises are statistically independent.

- In (48):
- (1) is the desired error signal;
  - (2) is the  $n'_{eq}(t)$  noise described by (21);
  - (3) is noise, self-noise, and cross-modulation, all spread by  $PRN_A(t)$ . This is the  $[\Sigma(t)]^2 PRN_A(t)$  term in (47);
  - (4) is noise, self-noise, and cross-modulation, all spread by  $PRN'_E(t)$ .

As the PN housekeeping sequences have decreased chip time, the spectral densities of the self-noise terms decreases. This, however, forces the IF bandwidth to be increased, thereby increasing the power in the noise terms in (48). There is an optimal choice of IF bandwidth and PN sequence chip time which will maximize the signal-to-noise ratio in the angle tracking loop. This optimization has not been performed. It is anticipated, however, that an IF bandwidth and PN sequence chip time can be chosen so that the resulting degradation in RMS angle tracking error is not significant and that the resulting RMS error is still well below any anticipated specifications.

#### 6.0 ACQUISITION COMMENTS

This appendix has been concerned primarily with antenna angle tracking performance under a variety of conditions. This has been carried out under the assumption that proper search detection and acquisition has taken place. The optimal search procedure for the Orbiter Ku-band communications system has been determined by Udalov [10].

The transition from detection to tracking by the antenna angle tracking control system is normally a straightforward procedure. There is, however, the possibility of detecting the presence of the TDRS signal on a sidelobe of the Orbiter antenna as illustrated in Figure 7. This is potentially a problem in any search/track transition. The sidelobes are usually sufficiently low in gain and the total clutter present via the sidelobe is sufficiently great to preclude the possibility of locking onto the signals through a sidelobe.

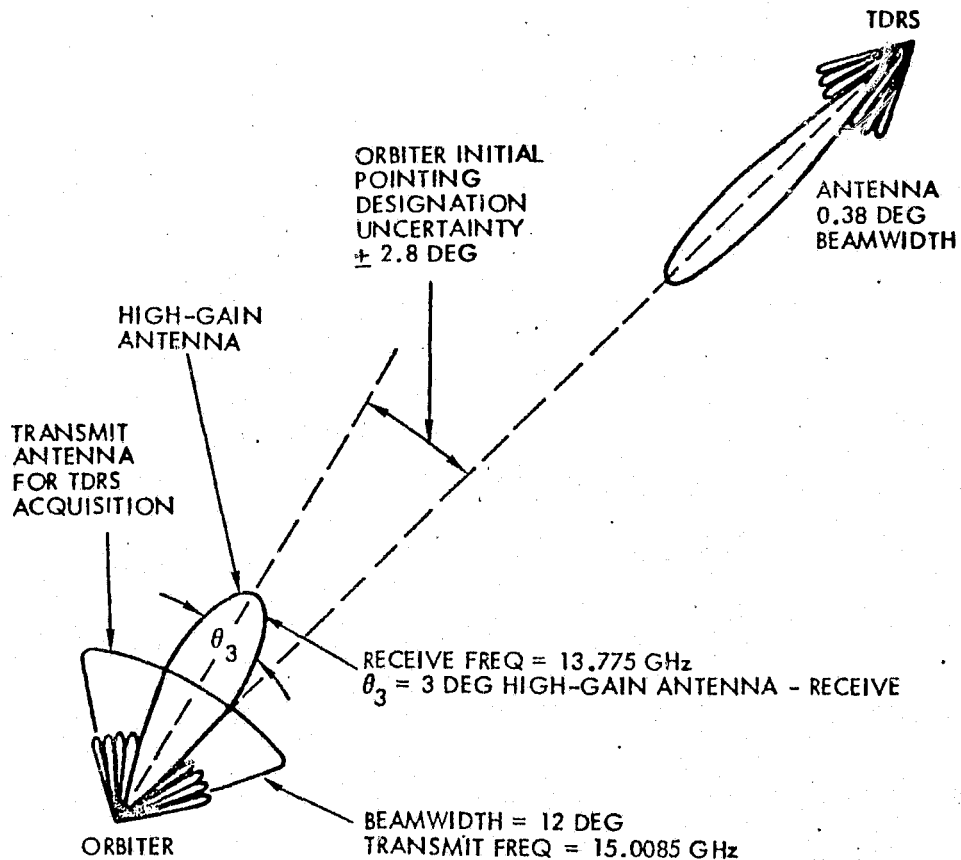


Figure 7. TDRS/Orbiter Antenna Beam Geometry for Acquisition [1]

In the case of the Orbiter Ku-band communication system when looking toward the TDRS, the clutter is negligible. If sufficient signal strength is present in the sidelobe, the detection threshold would be exceeded, and signal would be declared present.

Sidelobes are usually 15-25 dB down from the mainlobe. The circuit margin of the antenna angle control system is sufficiently high, as we have demonstrated here, that sidelobe lock could indeed take place. However, the PN sequence despreader, the RF tracking loop, and the symbol synchronization tracking loop have nowhere near 15-25 dB circuit margin. Therefore, if the antenna control system did indeed acquire and initiate

tracking on a sidelobe, the remaining subsequent tracking loops would not be able to detect and track.

If the search procedure is indeed halted, the present position and direction of the antenna in the search path should be recorded by the master control. If the position of detection is through a sidelobe, not all of the remaining tracking loops will be able to lock and initiate track. When this is noted, the system directs the antenna control system to break lock and reactivate search from the same position at which search was interrupted. This procedure avoids the situation of locking up and tracking on the sidelobe every time. This could be the case if the search procedure started over after a lockup takes place via a sidelobe.

The time for the remaining loops to declare if they are able to initiate track is short compared to the time constants associated with the angle tracking loop. Therefore, if angle search is interrupted because of a detection through a sidelobe, this interruption would be very short, and the search path would be interrupted only momentarily.

In an ideal antenna, the sidelobe would be doughnut-shaped and there would be some drifting or wobbling around the sidelobe. Practical antenna patterns often have peaks in the sidelobes, however. This allows the possibility of satisfactory two-channel angle tracking on a somewhat pencil-beam-shaped lobe on the sidelobe. If this peak of the sidelobe is 15-25 dB down from the mainlobe, this should not present a problem if the above operational procedure is followed.

Even though the sidelobe lock possibility is more acute at higher values of signal-to-noise ratio, which is the case here, if the above operational procedure is followed, sidelobe lock will not be a problem.

## REFERENCES

1. "Shuttle Orbiter Ku-Band Radar/Communications Subsystem Bidders Seminar," Rockwell International/Space Division, 13-14 August 1975, Contract NAS 9-14000.
2. "Integrated Communications and Radar Equipment, Ku-Band," Amendment, Rockwell International/Space Division Document MC409-0025, March 15, 1976.
3. "Space Shuttle RF Link Circuit Margins," NASA-JSC, May 1976.
4. D. K. Barton, Radar System Analysis, Prentice-Hall, 1964
5. P. W. Hannan, "Optimum Feeds for All Three Modes of a Monopulse Antenna," IRE Trans. Ant. Prop., Vol AP-9, No. 5, September 1961, pp. 444-461.
6. S. F. George and A. S. Zannamaker, "Multiple Target Resolution of Monopulse vs. Scanning Radars," Proc. NEC, No. 15, 1959, pp. 814-823.
7. J. B. Thomas, An Introduction to Communication Theory, Wiley, 1970.
8. A. J. Viterbi, Principles of Coherent Communication, McGraw-Hill, 1966.
9. M. Skolnik, Radar Handbook, McGraw-Hill, 1970.
10. S. Udalov, "Signal Detection and Angular Search Procedure for Shuttle Ku-Band Communication System," Axiomatix Report R7510-3, October 1975 (see also Final Report, under NASA Contract No. NAS 9-14614, Exhibit B).

## ADDENDUM A

### TRANSFER FUNCTIONS FOR AN INERTIALLY STABILIZED ANTENNA

This addendum describes transfer functions for an inertially stabilized antenna. A similar development is given in references 1 and 2. The search and track modes of operation are considered, as well as the transition from search to track. A deterministic design of the parameters is carried out, which is applicable to the Orbiter antenna control system. This design is used in our performance analysis of the antenna control system in the presence of receiver front end thermal noise.

We first consider the operation of gyros and how they establish the inertially stabilized reference. The results apply to both the communication and radar functions of the Orbiter system.

#### A.1 TYPES OF GYROS

There are generally considered to be two types of gyros, attitude gyros and rate gyros. An attitude gyro, or gyroscopic compass, is usually free to move with respect to the gyro case such that, when the case is rigidly attached to a vehicle, the attitude of the vehicle with respect to the gyroscopic spin axis (inertial space) can be determined by measuring the angles of the spin axis with respect to the gyro case.

#### A.2 RATE GYROS

The second type of gyro is termed "rate gyro" and is almost always a single-degree-of-freedom instrument. That is, the motion is restrained to a single degree of freedom with respect to the gyro case.

There are essentially two classes of rate gyros. In the most common class, the motion in the single-degree-of-freedom direction is restrained with a spring and the gyro is termed a "spring restrained rate gyro." In the spring restrained rate gyro, the output sensor measures the angular deflection of the gyro from its null position. Since the

restoring force from the spring is proportional to the angular deflection, the output sensor directly measures the angular rate of the gyro case.

### A.3 SINGLE-DEGREE-OF-FREEDOM RATE INTEGRATING GYRO

The second class of rate gyros is the single-degree-of-freedom rate integrating gyro. This is the gyro to be used for the inertially stabilized antenna search and tracking system. This gyro has the components shown in Figure A-1.

We now consider the various functions of a rate integrating gyro. In all functions described, the gyro case is mounted on the back of the antenna. The gyro case therefore represents the antenna position.

### A.4 FUNCTIONS OF A RATE INTEGRATING GYRO

When operating as part of a control system, a rate integrating gyro can perform several functions. We now discuss those functions which are utilized in the antenna search and tracking control system. In all cases, the inertial reference capability of the rate integrating gyro is utilized.

#### A.4.1 Function 1 for Rate Integrating Gyro: Measurement of Rotational Rate

A block diagram of a rate integrating gyro used for measurement of rotational rate is shown in Figure A-2. The input is a mechanical rotation whose rate is represented by  $\dot{\theta}_{in}$  radians/sec. The output sensor of the gyro unit is fed directly into an amplifier, which in turn drives the torquer such that the angular rate,  $\Delta\dot{\theta}$ , is driven to zero. The closed loop transfer function relating  $\dot{\theta}_{out}$  to  $\dot{\theta}_{in}$  is

$$\frac{\dot{\theta}_{out}}{\dot{\theta}_{in}} = \frac{(K_T)^{-1}}{\tau s + 1}$$

where  $\dot{\theta}_{in}$  = input mechanical rotational rate (radians/sec)

$\dot{\theta}_{out}$  = output (in volts, but representing radians/sec)

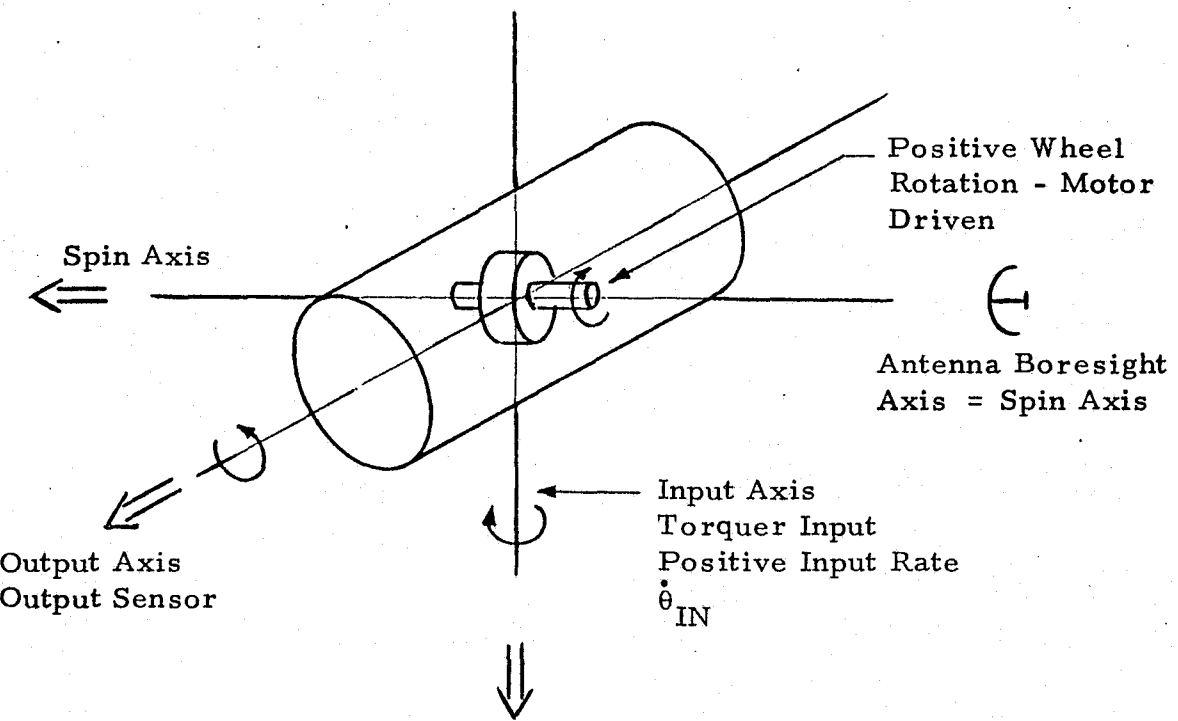


Figure A-1. Axis Orientation for a Single-Degree-of-Freedom Rate Integrating Gyro

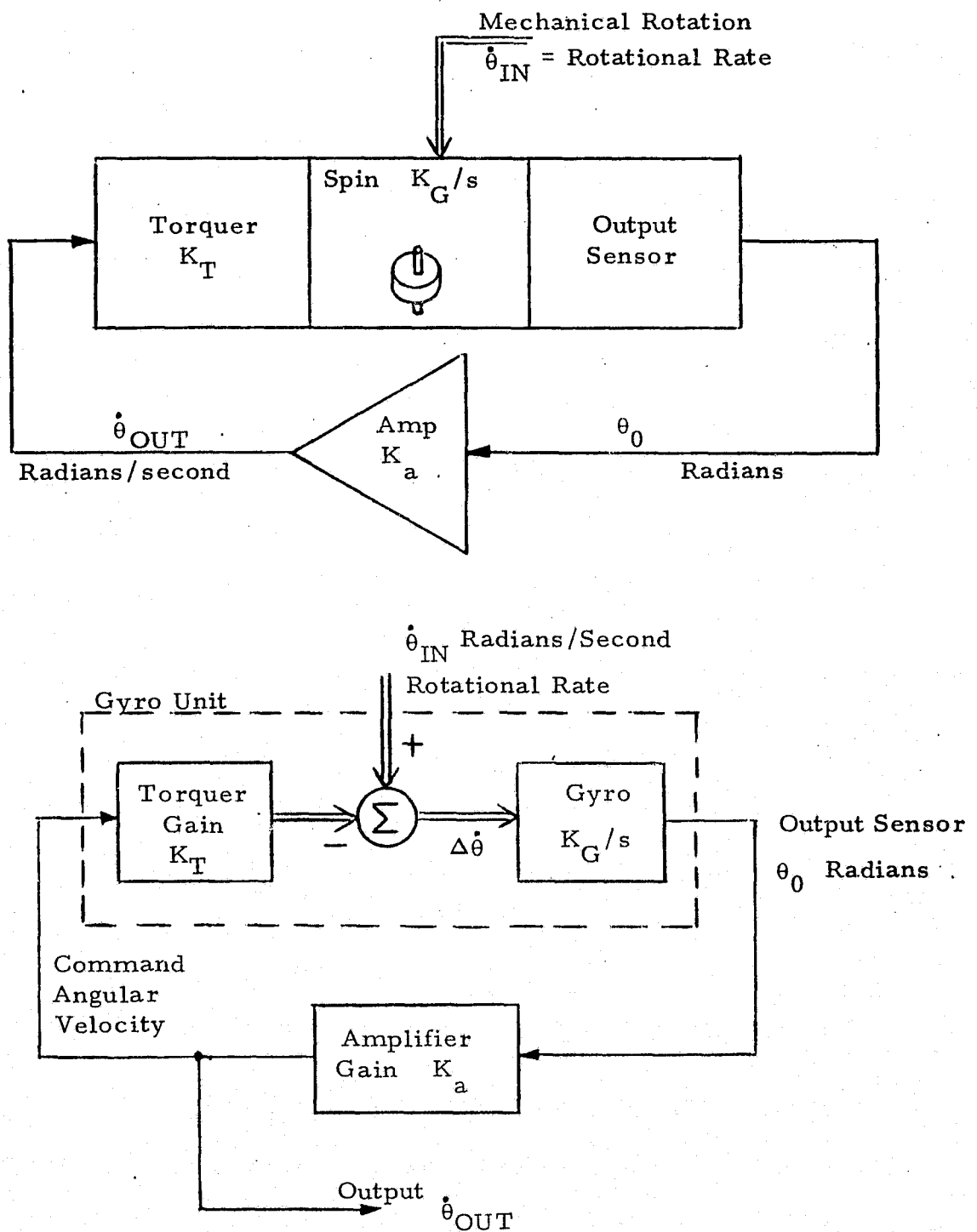


Figure A-2. Function 1 for Integrating Gyro: Measurement of Rotational Rate

$$\tau = \frac{1}{K_G K_a K_T} = \text{time constant (seconds)}$$

$K_G$  = gyro gain (radians/radians)

$K_a$  = amplifier gain ( $\frac{\text{radians/sec (in volts)}}{\text{radians}}$ )

$K_T$  = torquer input gain ( $\frac{\text{radians/sec}}{\text{radians/sec (in volts)}}$ )

Therefore, the output,  $\dot{\theta}_{\text{out}}$ , is a filtered (first-order) and attenuated (by  $K_T^{-1}$ ) version of  $\dot{\theta}_{\text{in}}$ . The amplifier gain  $K_2$  can be designed to make the time constant any desired value.

An equivalent model of the integrating gyro is shown in Figure A-3. The integrating function is taken to be part of the input torquer, rather than part of the gyro unit itself. This agrees with the concept that the torquer itself is a motor and therefore an integrator. When this is assumed, the input mechanical rotation rate must be integrated as shown in Figure A-3 before being summed in the gyro.

We shall use the model in Figure A-2. When this is done, angular outputs are differentiated before being summed, since these inputs are now angular rates.

#### A.4.2 Function 2 for Rate Integrating Gyro: Scan Control

A block diagram of a rate integrating gyro used for scan control is shown in Figure A-4. In this case, the input is a deterministic programmed command rate,  $\dot{\theta}_c$ . For scan control, we assume the vehicle is in a fixed known position. The gyro is torqued to a desired position or in a desired path relative to inertial space. The closed loop transfer function relating the input command angular rate,  $\dot{\theta}_c$ , to the output motor position,  $\theta_m$ , is given by

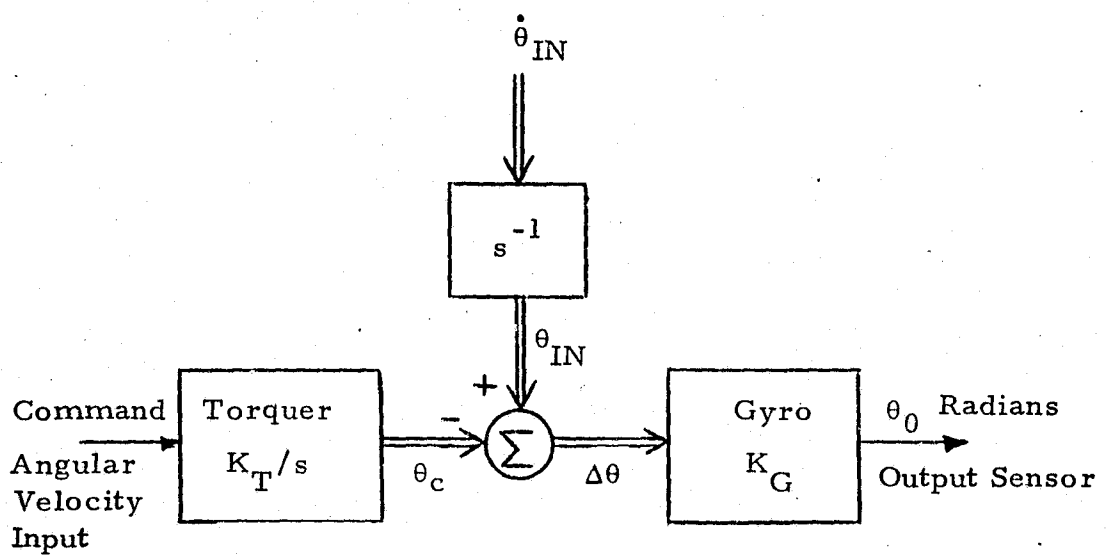


Figure A-3. Equivalent Model of Integrating Gyro

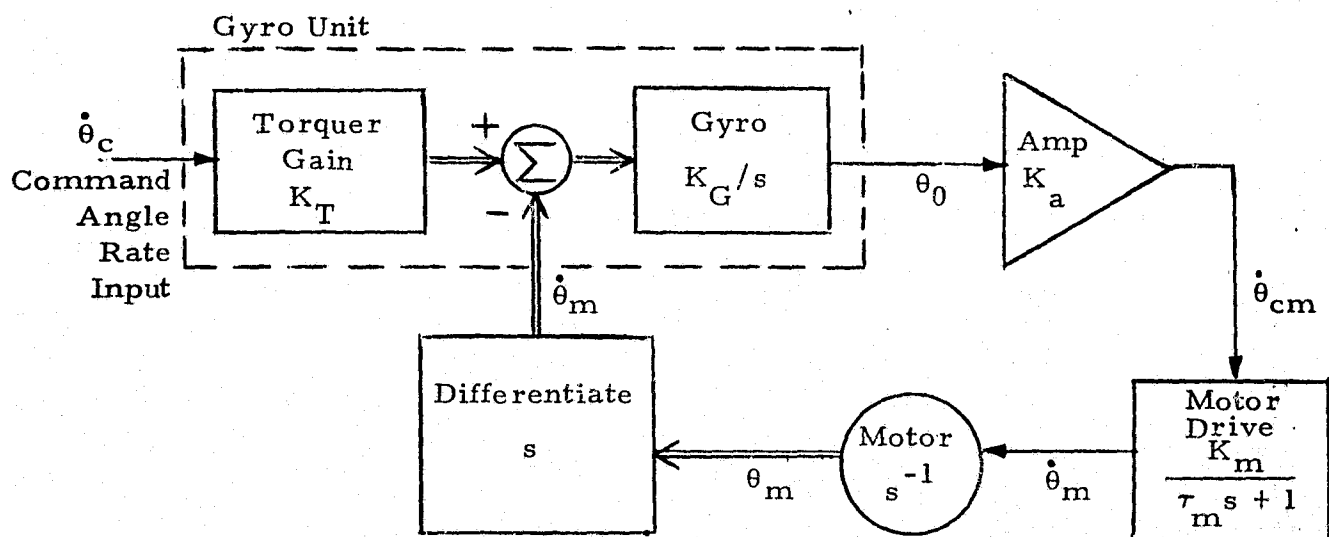
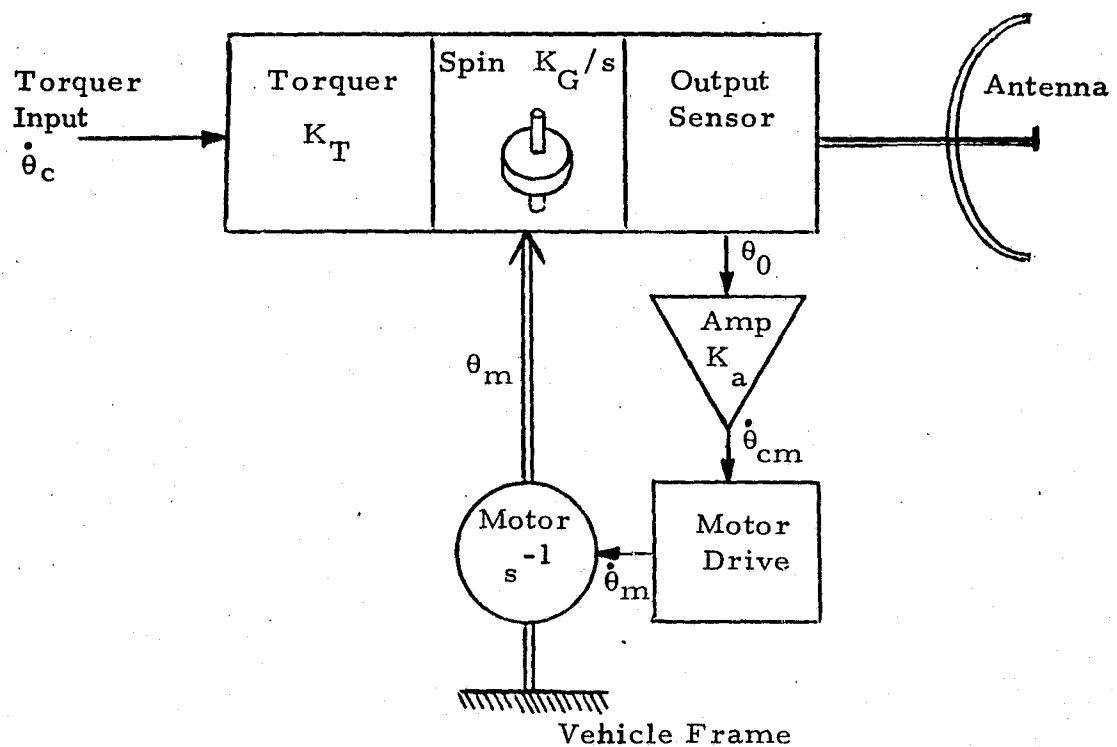


Figure A-4. Function 2 for a Rate Integrating Gyro: Scan Control

$$\frac{\dot{\theta}_m}{\dot{\theta}_c} = \frac{1}{s} \left[ \frac{K_T}{1 + \frac{s}{K_G K_a K_m} + \frac{s^2 \tau_m^2}{K_G K_a K_m}} \right]$$

$$= \frac{K_T}{s} \left[ \frac{1}{1 + \frac{2\zeta s}{\omega_n} + \frac{s^2}{\omega_n^2}} \right]$$

where

$\dot{\theta}_c$  = torquer command voltage representing angular rate (radians/sec)

$\theta_m$  = motor output angle (radians) (we are neglecting gear ratios), with respect to some fixed reference

$K_m$  = motor drive gain

$\omega_n$  = natural frequency (radians/sec)

$$= \left[ \frac{K_G K_a K_m}{\tau_m} \right]^{1/2} = \left( \frac{K}{\tau_m} \right)^{1/2}$$

$\zeta$  = damping constant

$$= \frac{\omega_n}{2} \frac{1}{K_G K_a K_m} = \frac{1}{2} \left[ \frac{1}{\tau_m K} \right]^{1/2}$$

and  $K_T$ ,  $K_a$ ,  $K_G$  have the same designation and units as in Function 1.

The output,  $\theta_m$ , also represents the antenna/gyro-case position under the assumption that the vehicle angle is known and set to zero. In this case, it is seen that the antenna/gyro-case position will be driven to the position represented by the integral of the input command signal,  $\dot{\theta}_c$ .

This is essentially a second-order closed-loop transfer function. The loop gains and motor time constant can be chosen such that the natural frequency and damping factor are equal to any set of chosen values. In particular,

$$\tau_m = \frac{1}{2\zeta\omega_n}$$

and

$$K = \frac{\omega_n}{2\zeta}$$

where

$$K = K_G K_a K_m.$$

The parameters describe not only the gyro and its case, but also the antenna dish. These parameters therefore account for the inertia of the antenna when describing the capability of the dish to follow a prescribed path.

#### A.4.3 Function 3 for Rate Integrating Gyro: Inertial Stabilization

A block diagram of a rate integrating gyro used for inertial stabilization (without tracking of any target) is shown in Figure A-5. In this case, the input to the target is open. When the vehicle moves with respect to an inertial reference, the motor output,  $\theta_m$ , follows the movement so that the antenna position, given by  $\theta_A$ , returns to its original steady-state position. The transfer function between  $\theta_m$  and  $\theta_v$  is given by

$$\frac{\theta_m}{\theta_v} = H_{IS}(s) = \frac{1}{1 + \frac{s}{k} + \frac{\tau_m}{K} s^2} = \frac{1}{1 + \frac{2\zeta s}{\omega_n} + \left(\frac{s}{\omega_n}\right)^2}$$

where the desired antenna position is

$$\theta_A = \theta_m - \theta_v = 0.$$

In the above transfer function,

$\theta_v$  = angular position of the vehicle with respect to an inertial source (radians)

$\theta_A$  = antenna position, where the desired position is  $\theta_A = 0$  (radians)

and  $K$ ,  $\zeta$ , and  $\omega_n$  are as previously defined.

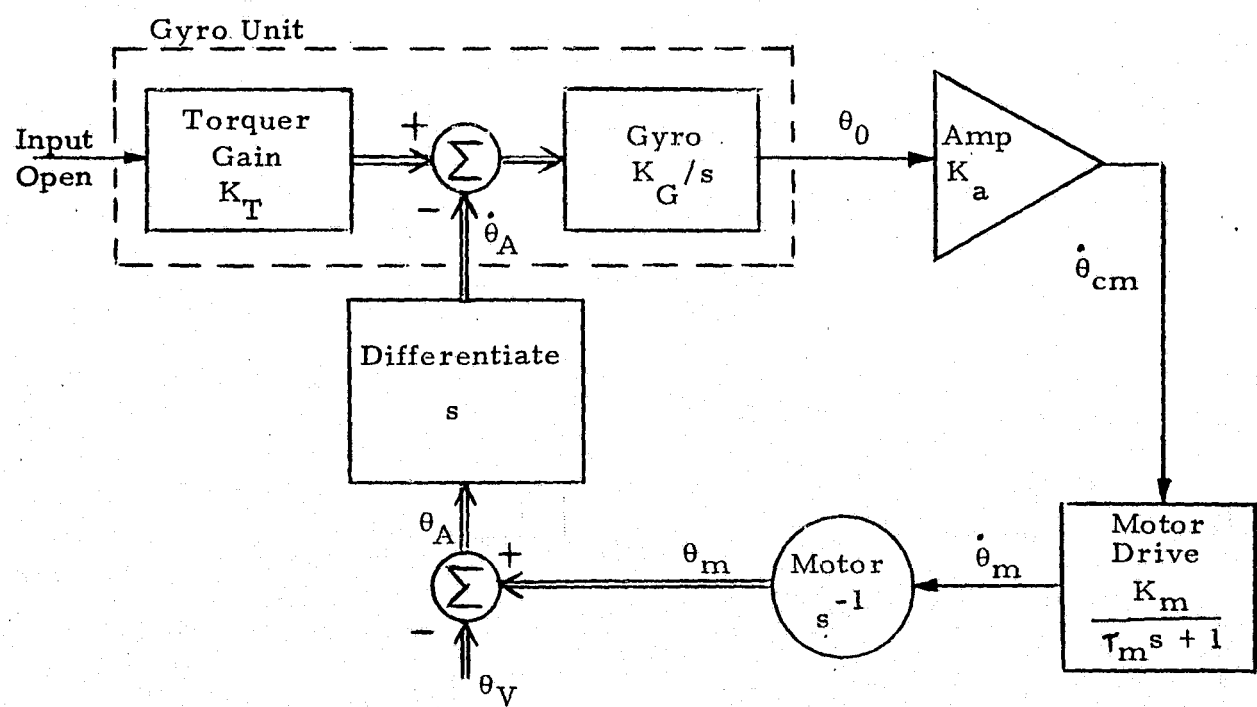
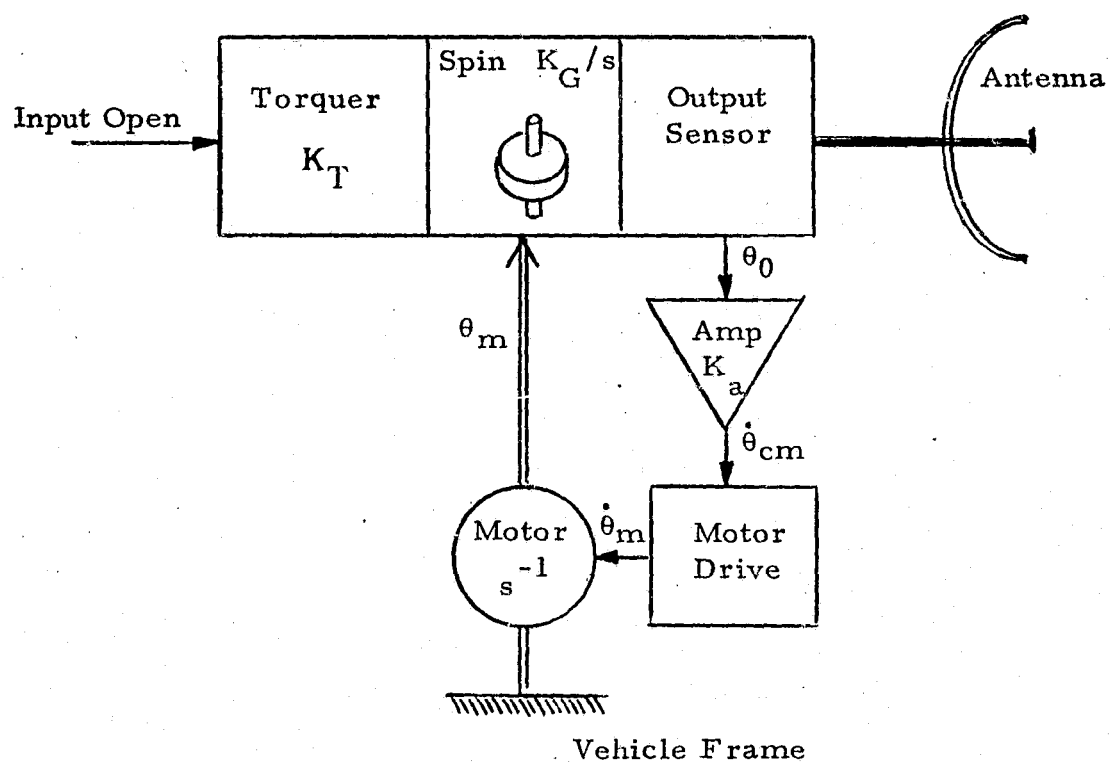


Figure A-5. Function 3 for Rate Integrating Gyro: Inertial Stabilization

Note that this second-order transfer function is identical to that of scan control. Therefore, the transient response for inertial stabilization is identical to that of scan control.

We now combine these various functions of a rate integrating gyro into an antenna angle control system which is inertially stabilized.

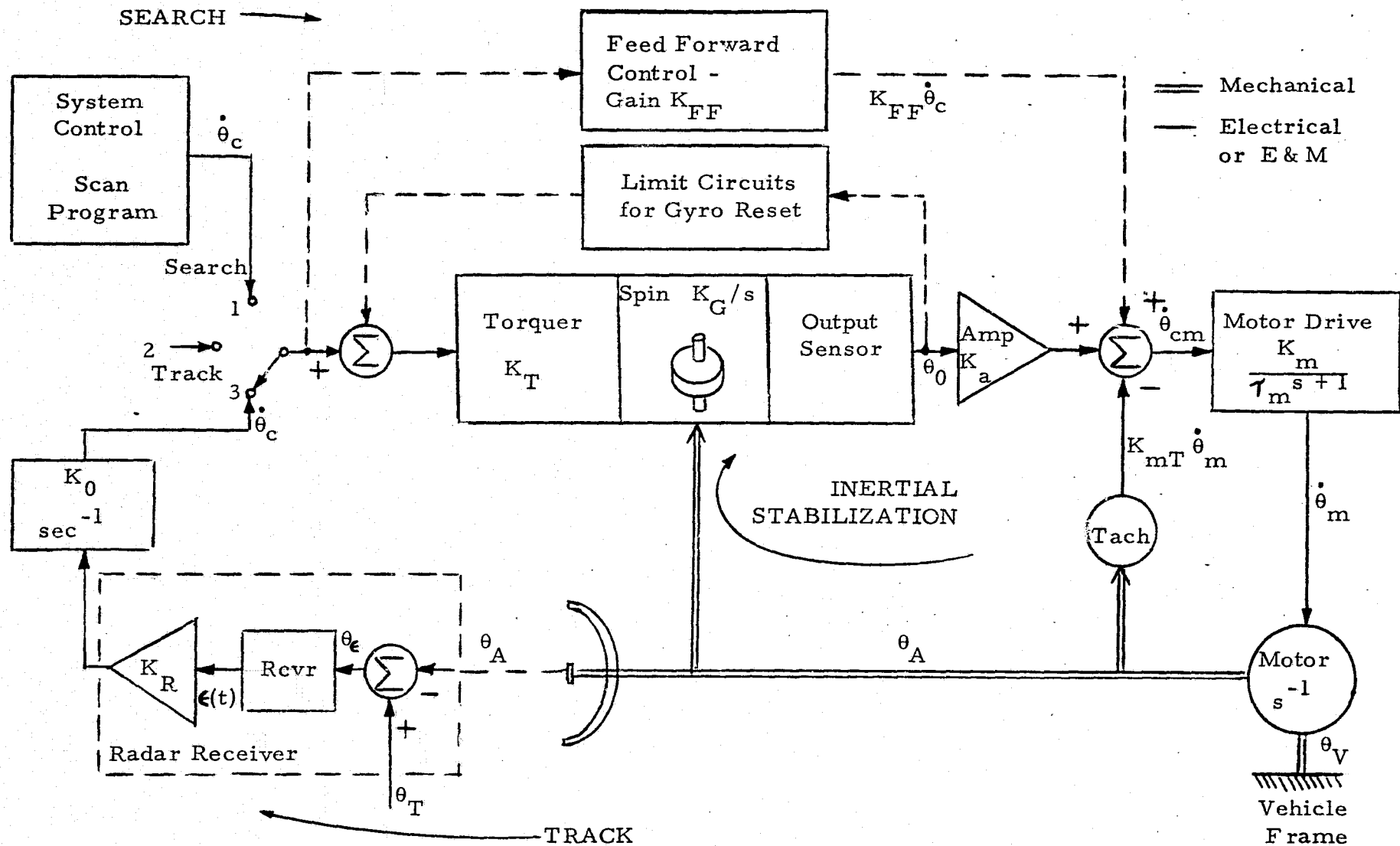
#### A.5 ANTENNA ANGLE CONTROL WITH RATE INTEGRATING GYRO

A simplified sketch of a single-axis antenna control system which uses a rate integrating gyro for inertial stabilization is shown in Figure A-6. The control switch is shown in the track mode. During the following discussion, only one axis is described. Since the other axis is essentially the same, the discussion serves to explain its operation also.

In the upper or search position, the inputs are controlled from the computer search algorithm and the operation is as described in section A.4.2. Both spiral and raster search patterns have been studied [5]. With the overall search volume to be illuminated being conically shaped, the spiral search algorithm is more efficient from the standpoint of maximizing the dwell time on target. This is the case both in communication and radar operation of the system.

In the search mode, the search algorithm activates the torquer of the gyro. The gyro case and antenna dish then follow the gyro via the transfer function described in section A.4.2. The second-order transfer function describes the capability of the antenna dish to follow the path prescribed by the search algorithm. This transfer function includes the parameters of the gyro, as well as the inertia of the antenna. The gyro is moved by the torquer, and the antenna and gyro case are locked to the gyro via the second-order transfer function.

When a target is detected, the search algorithm stops and the switch position is temporarily set in position 2. The antenna should stabilize itself in inertial space within the cone required for target pull-in when target tracking is initiated.



$\theta_A$  = Antenna Angle = Boresight Axis;

$\theta_T$  = Target Angle;  $\theta_\epsilon$  = Tracking Error Angle

Figure A-6. Sketch of a Single Axis Antenna Angle Control System With Rate Integrating Gyro

By staying in position 2 for a short period, we allow time for transients in the antenna due to terminating the search algorithm to die out before the tracking operation is initiated. The antenna position at which the target is detected should be memorized by the search algorithm. The reason is that, when tracking is initiated, if the target is not within the antenna's main lobe, target tracking will not begin and the control system must return to the search algorithm. When such is the case, the proper position to reactivate the search algorithm is at the position where the search algorithm was interrupted. This approach will minimize pull-in transients when tracking is initiated.

The antenna and gyro case are slaved with respect to an inertial reference. This operation (inertial stabilization) is described in section A.4.3. Note that, in all cases, the inertial reference is utilized. At any time the spacecraft is maneuvered, the antenna automatically retains its inertial reference.

In the tracking position of the control switch in Figure A-6, the error signal,  $\theta_\epsilon$ , is amplified and the resulting signal is applied to the torquer. As in the search mode, the error signal moves the gyro, and the antenna dish is slaved to the gyro.

The limit circuits for gyro reset limit the overall motion of the gyro as described in references 1 and 2. The feed forward control gain provides one way of reducing the tracking loop time constants. These are shown in dotted lines since they are not considered in the design.

The tracking position uses the monopulse antenna and radar receiver. For the present discussion, this is modeled as a receiver gain,  $K_R$ . The effect of the antenna and radar receiver is quantitatively discussed in the body of this report. The output of the receiver is an error signal,  $\epsilon(t)$ , proportional to the angular pointing error to the target. The command signal to the antenna in all cases is a command rate,  $\dot{\theta}_c$ . We have therefore placed a gain  $K_0 = 1$  with units of [seconds]<sup>-1</sup> in the tracking loop. Note that the amplifier,  $K_a$ , also has units of [seconds]<sup>-1</sup>.

The paths of the primary control loops for search, track, and inertial stabilization are shown in Figure A-6. A block diagram of the antenna angle control system with a rate integrating gyro is shown in Figure A-7, in which the limit circuits have been deleted.

The inertial stabilization loops prevent vehicle body motions from affecting antenna position so that target tracking accuracy of the radar antenna can be properly maintained.

A tachometer feedback has been placed around the motor drive to control the time constant of the motor itself.

The parameters in Figures A-6 and A-7 are described as follows.

$K_R$  = receiver tracking gain (radians/radians)

$K_0$  =  $1 \text{ (sec)}^{-1}$

$K_T$  = torquer amplifier gain ( $\frac{\text{radians/sec}}{\text{radians/sec}}$ )

$K_G$  = output gain of rate integrating gyro ( $\frac{\text{radians/sec}}{\text{radians/sec}}$ )

$K_m$  = gain of motor control amplifier and motor  
( $\frac{\text{radians/sec}}{\text{radians/sec}}$ )

$K_a$  = amplifier gain ( $\text{sec}^{-1}$ )

$K_{mt}$  = gain of motor tachometer feedback ( $\frac{\text{radians/sec}}{\text{radians/sec}}$ )

$\epsilon(t)$  = angle track error information which is the input to the antenna angle control system (radians)

$\theta_\epsilon$  =  $\theta_T - \theta_A$  = actual tracking error (radians)

$\theta_T$  = target angle (radians)

$\theta_A$  = antenna angle (radians) =  $\theta_m - \theta_v$

$\theta_m$  = rotational angle of motor (radians)

$\theta_v$  = vehicle angle with respect to an inertial reference (radians), which is assumed to be zero

$\dot{\theta}_t$  = inertial precessional rate of gyro in axis of freedom due to torquer (radians/sec)

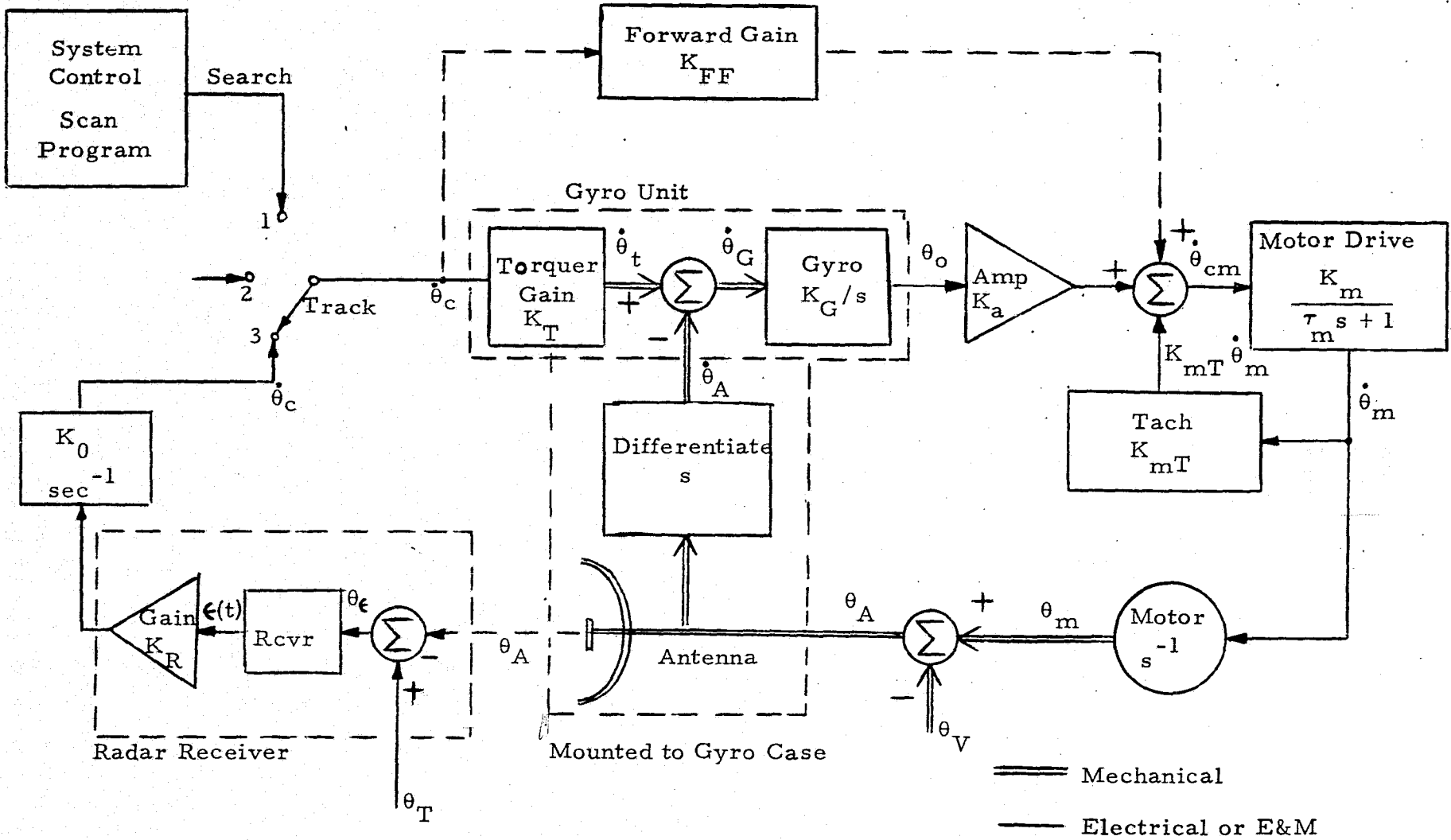


Figure A-7. Block Diagram of a Single Axis Antenna Angle Control System With Rate Integrating Gyro

$\dot{\theta}_G$  = rate of change of gyro output = difference between  
rate of change of spin axis and rate of change of  
case (radians/sec)

$\theta_0$  = output of rate integrating gyro (volts representing  
radians)

This block diagram is now used to develop a simplified block diagram of a single-axis antenna control system, design the system parameters, and determine the control system transfer function from the error signal,  $\epsilon(t)$ , to the antenna angle,  $\theta_A$ .

#### A.6. SIMPLIFIED BLOCK DIAGRAM AND RESULTING TRANSFER FUNCTIONS

A simplified block diagram of a single axis antenna angle control system in the tracking mode is shown in Figure A-8. We have assumed the vehicle is not rotating and that  $\theta_v \equiv 0$ .

The motor drive and tachometer feedback have been consolidated into the single transfer function:

$$\frac{K_a}{\tau_a s + 1}$$

where  $K_a$  = combined motor amplifier, motor and gear train gains =  $K_m / (1 + K_m K_{mt})$

$\tau_a$  = resulting drive system time constant  
=  $\tau_m / (1 + K_m K_{mt})$

The total tracking closed-loop transfer function, assuming the receiver is modeled by 1, is given by

$$\frac{\theta_A}{\theta_T} = \frac{1 + \tau_\beta s}{1 + a_1 s + a_2 s^2 + a_3 s^3}$$

where  $\tau_\beta$  = time constant of closed-loop zero =  $\frac{K_{FF}}{K_T K_G K_a}$

$K_{FF}$  = feed forward control gain

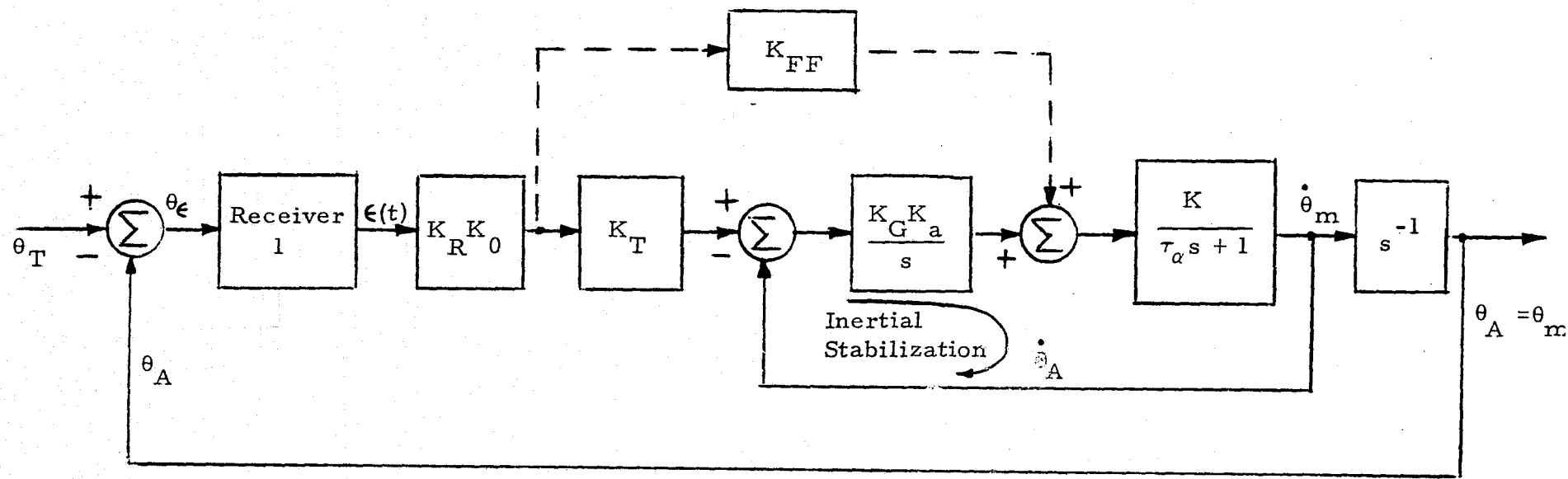


Figure A-8. Simplified Block Diagram of a Single Axis Antenna Angle Control System in the Tracking Mode

$$a_1 = \frac{1}{K_R K_T K_G} \left[ \frac{K_{FF} K_R}{K_a} + \frac{K_G}{K_0} \right]$$

$$a_2 = [K_R K_0 K_T K_G K_a K_a]^{-1} = (K)^{-1}$$

$$a_3 = \tau_a / K$$

$K$  = total open loop gain .

This system always has a steady-state angular error of zero.

The open loop transfer function from the radar receiver error signal,  $\epsilon(t)$ , to the antenna angle,  $\theta_A$ , is given by

$$F(s) = \frac{K_R K_0 K_T}{s} \left[ \frac{1 + \tau_\beta s}{1 + b_1 s + b_2 s^2} \right]$$

where  $b_1 = [K_G K_a K_a]^{-1}$

$$b_2 = \tau_a [K_G K_a K_a]^{-1}$$

and  $\tau_\beta$  is defined above .

These constants are now evaluated to provide proper inertial stabilization.

#### A.6.1 Inertial Stabilization Closed-Loop Transfer Function

Inspection of Figure A-7 shows that the open loop transfer function for the inertial stabilization loop consisting of gyro, motor driver, and differentiator is given by

$$\frac{K_G K_a K_a}{s(\tau_a s + 1)}$$

The corresponding closed loop transfer function is

$$\begin{aligned}
 H_{IS}(s) &= \frac{1}{1 + \frac{s}{K_G K_a K_a} + \frac{\tau_a s^2}{K_G K_a K_a}} \\
 &= \frac{1}{1 + \frac{2\zeta}{\omega_i} s + \left(\frac{s}{\omega_i}\right)^2} \\
 &= \frac{1}{1 + b_1 s + b_2 s^2}.
 \end{aligned}$$

Gyro loops have bandwidths typically equal to 1 Hz to 10 Hz. A common design for an inertial stabilization loop which is satisfactory is to have the natural frequency  $\omega_i/2\pi = 5$  Hz and have the loop critically damped, so that  $\zeta_i = 0.707$ . Then,

$$\zeta_a = \frac{1}{2\zeta_i \omega_i} = 0.0225 \text{ sec}$$

and  $K_G K_a K_a = \frac{\omega_i}{2\zeta_i} = 22.21 [\text{sec}]^{-1}$ .

A value of  $\tau_a = 0.0225$  corresponds to a tachometer loop 3 dB bandwidth of approximately 7 Hz. The tachometer gain,  $K_{mt}$ , can be increased in order to increase this bandwidth, if necessary.

Typical component characteristics [1, 2] are:

$$K_T = 0.004$$

$$K_G = 7.5$$

$$\tau_m = 0.02 \text{ sec.}$$

With  $\tau_m \approx \tau_a$ , we can assume  $K_{mt} = 0$ , thus eliminating the need for the tachometer feedback. Also, the amplifier  $K_a$  can be easily chosen so that the inertial stabilization open loop gain is approximately 22.2.

### A. 6.2 Effect of Vehicle Body Motion on Angle Tracking Capability

Referring to section A.4.3, note that the closed-loop transfer function for inertial stabilization developed here is the same as that which relates vehicle motion to  $\theta_m$ . We can therefore determine the effects of vehicle body motion on angle tracking capability.

One simple evaluation is by use of the final value theorem of the Laplace transform. The steady-state bias error of the antenna which is tracking a target and simultaneously subjected to vehicle motion is given by

$$\begin{aligned}\text{Steady State Error} &= \lim_{s \rightarrow 0} V(s) [H_{IS}(s) - 1] s \\ &= \lim_{s \rightarrow 0} V(s) \left[ \frac{2\zeta_i}{\omega_i} s + \left( \frac{s}{\omega_i} \right)^2 \right] s\end{aligned}$$

where  $V(s)$  is the Laplace transform of the vehicle angular motion.

It is seen that a constant angular motion of the vehicle will have a steady-state error of zero on the tracking error. An angular acceleration of vehicle motion given by  $1/2 K_a t^2$  would have a steady-state bias in angular tracking error given by

$$\text{Steady State Error} = \frac{K_a \zeta_i}{\omega_i} = 0.045 K_a$$

where  $K_a$  is the angular acceleration in radians/sec<sup>2</sup>.

Since vehicle angular acceleration is expected to be small, the resulting bias error will be very small with respect to the main lobe beamwidth. This bias error has therefore been neglected in the analysis.

### A. 6.3 Open Loop Transfer Function

We shall use an open loop transfer function under the assumption  $K_{FF} = 0$ . The transfer function from  $\epsilon(t)$  to  $\theta_A$  in Figure A-7 is then given by

$$F(s) = \frac{K_R K_0 K_T}{s} H_{IS}(s) = \frac{K_L}{s} \left[ \frac{1}{1 + b_1 s + b_2 s^2} \right]$$

where  $\tau_\beta$  is now zero. The constants  $b_1$  and  $b_2$  are

$$b_1 = \frac{2\zeta_i}{\omega_i} = 0.045016$$

$$b_2 = \omega_i^{-2} = 0.001013 .$$

With  $K_T$  on the order of 0.004, and  $K_0 = 1$ , we will design  $K_T$  sufficiently large to have the desired properties of the closed loop transfer function at the design point. This is carried out in the body of the appendix.

## REFERENCES

1. "Study to Investigate and Evaluate Means of Optimizing the Radar Function for the Space Shuttle," prepared by D<sup>2</sup>C, Escondido, California, for NASA-JSC, under Contract NAS 9-14615, December 23, 1975.
2. "Investigate and Evaluate Means of Integrating and Optimizing the Combined Radar/Communication Functions," Progress Report #8, prepared by D<sup>2</sup>C, Escondido, California, under Contract NAS 9-14615, February 15, 1976.
3. P. H. Savet, Gyroscopes: Theory and Design, McGraw-Hill, 1961.
4. W. Wrigley, W. Hollister, and W. Genhard, Gyroscopic Theory Design, and Instrumentation, M.I.T. Press, 1969.
5. S. Udalov, "Signal Detection and Angular Search Procedure for Shuttle Ku-Band Communication System," Axiomatix Report No. R7510-3, October 1975.

ADDENDUM B  
AUTOMATIC GAIN CONTROL CONSIDERATIONS

A typical noncoherent AGC is shown in Figure B-1. The input is  $\Sigma(t)$  as shown in Figure 1 and described in equation (6). The noncoherent detector is modeled as a square law device followed by a zonal lowpass filter. The gain controlled amplifier has gain  $A_{GCA}^{-1}(t)$ , so that the AGC output signal is given by

$$v_{AGC}(t) = [A_{GCA}(t)]^{-1} \Sigma(t) . \quad (A-1)$$

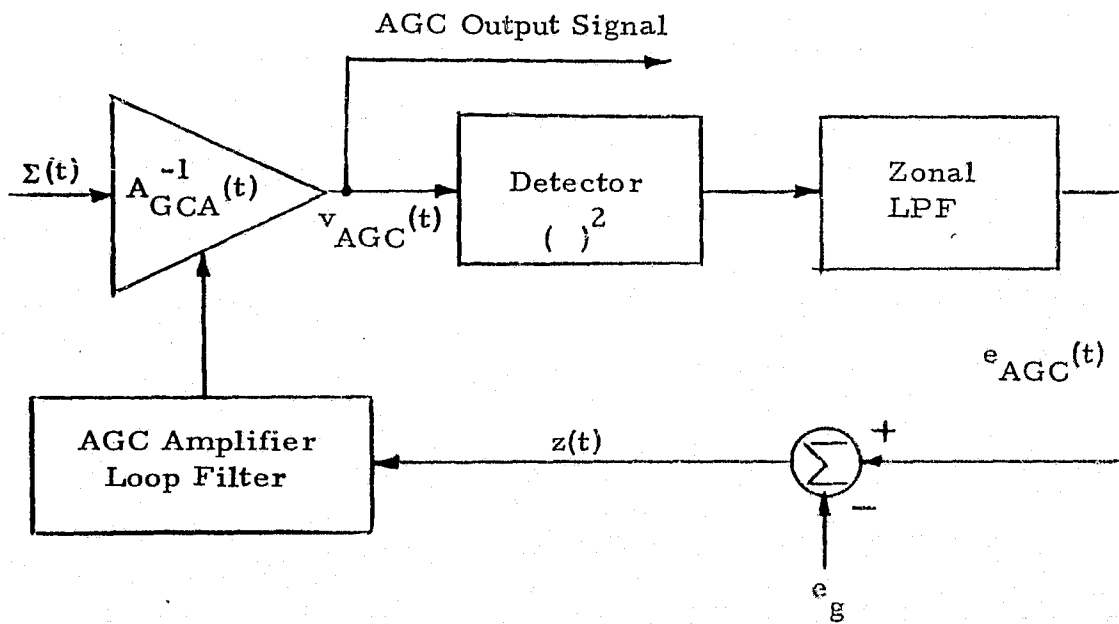


**Figure B-1.** Noncoherent Automatic Gain Control (AGC)

In a slowly varying AGC, the control voltage is essentially given by the DC value of  $e_{AGC}(t)$ , which is

$$e_{AGC}(t) = [A_{GCA}]^{-2} [\Sigma(t)]^2 . \quad (B-2)$$

In both the radar and communication applications of the AGC, the targets, and hence the signal levels, will be sufficiently slowly varying that the above assumption is entirely satisfactory.

From (6), the baseband part of  $[\Sigma(t)]^2$  is given by

$$[\Sigma(t)]^2 \Big|_{\substack{\text{base} \\ \text{band}}} = E_s^2 P_{rec} + n_1^2(t) + n_2^2(t) + 2 E_s \sqrt{P_{rec}} d(t) n_1(t) . \quad (B-3)$$

The average value of  $[\Sigma(t)]^2$  is

$$\begin{aligned} E [\Sigma(t)]^2 &= E_s^2 P_{rec} + 2 R_{L\Sigma}(0) \\ &= E_s^2 P_{rec} + N_0 \Sigma B_\Sigma . \end{aligned} \quad (B-4)$$

In the ideal noncoherent AGC which has unlimited range of operation, an excellent approximation for  $A_{GCA}$  is

$$\begin{aligned} A_{GCA}^2 &= E [\Sigma(t)]^2 \\ &= E_s^2 P_{rec} + N_0 \Sigma B_\Sigma . \end{aligned} \quad (B-5)$$

As expected in a noncoherent AGC, the AGC amplification is based on the sum of the signal power and noise power. Therefore, at low signal-to-noise ratios, the AGC is primarily noise dependent, and at high signal-to-noise ratios, it is primarily signal dependent.

This is the relationship used in the performance prediction to evaluate angle tracking capability of the Ku-band communication signal from TDRS and the Ku-band radar. More sophisticated analyses of AGC could have indeed been carried out. In view of the design margin in the result, however, any small deterioration in performance due to non-ideal AGC will still result in an RMS angle error well below any anticipated specification.

## ADDENDUM C

NOISE POWER SPECTRAL DENSITY OF EQUIVALENT  
LOOP NOISE

In this appendix, the one-sided noise spectral density of the equivalent loop noise,  $n'_{eq}(t)$ , as given by Equation (21) is determined. The auto-correlation function of  $n'_{eq}(t)$  is

$$\begin{aligned} R_{n'_{eq}}(\tau) &= R_{L\Sigma}^2(\tau) + R_{L\Delta}^2(\tau) \\ &\quad + P_{rec} R_d(\tau) [E_\Delta^2 R_{L\Sigma}(\tau) + E_s^2 R_{L\Delta}(\tau)]. \end{aligned} \quad (C-1)$$

The Fourier transform of the first two terms in (C-1) is designated as  $S_1(f)$ . This spectral density evaluated at  $f=0$  is

$$S_1(0) = \left(\frac{N_{0\Sigma}}{2}\right)^2 B_\Sigma + \left(\frac{N_{0\Delta}}{2}\right)^2 B_\Delta. \quad (C-2)$$

The contribution to the spectral density of  $n'_{eq}(t)$  from the last term in (C-1) is designated as  $S_2(f)$ . It is the Fourier transform of

$$\begin{aligned} &P_{rec} R_d(\tau) [E_\Delta^2 R_{L\Sigma}(\tau) + E_s^2 R_{L\Delta}(\tau)] \\ &= P_{rec} R_{PRN}(\tau) R_m(\tau) [E_\Delta^2 R_{L\Sigma}(\tau) + E_s^2 R_{L\Delta}(\tau)] \end{aligned} \quad (C-3)$$

where  $R_{PRN}(\tau)$  is the autocorrelation function of the PN sequence and  $R_m(\tau)$  is the autocorrelation function of the digital message sequence  $m(t)$ .

We compute  $S_2(0)$  for two cases: (I) the PN sequence is present in the angle control system, i.e., not removed by the despread. The despread must obviously be present in the receiver, but in this case, it is not a part of the angle control loop. This is the present baseline configuration. (II) the PN sequence is absent, i.e., the despread in Figure 1 is present and does remove the PN sequence ideally.

Case I. PN Sequence Present in All Channels, and Not Despread

In Figure C-1, the autocorrelation functions of the Bi- $\phi$ -L data sequence and the PN sequence are shown. Since  $T_c \ll T_s$ , we make the approximation that

$$R_{m_s}(\tau) = R_{m_c}(\tau) \approx 1 \quad \text{for } |\tau| \leq T_c \quad (\text{C-4})$$

where  $T_c$  is the PN sequence chip time. We also employ the triangular approximation for  $R_{PRN}(\tau)$  shown in Figure C-1. This also is an excellent approximation, due to (C-4). Then,

$$\begin{aligned} S_2(f) &= \mathcal{F} \left\{ P_{rec} R_{PRN}(\tau) [E_\Delta^2 R_{L\Sigma}(\tau) + E_s^2 R_{L\Delta}(\tau)] \right\} \\ &= P_{rec} \left\{ E_\Delta^2 S_{PRN}(f) * S_{L\Sigma}(f) + E_s^2 S_{PRN}(f) * S_{L\Delta}(f) \right\} \end{aligned} \quad (\text{C-5})$$

and

$$\begin{aligned} S_2(0) &= P_{rec} \left\{ E_\Delta^2 \int_{-B_\Sigma/2}^{B_\Sigma/2} \frac{N_0\Sigma}{2} S_{PRN}(f) df \right. \\ &\quad \left. + E_s^2 \int_{-B_\Delta/2}^{B_\Delta/2} \frac{N_0\Delta}{2} S_{PRN}(f) df \right\}. \end{aligned} \quad (\text{C-6})$$

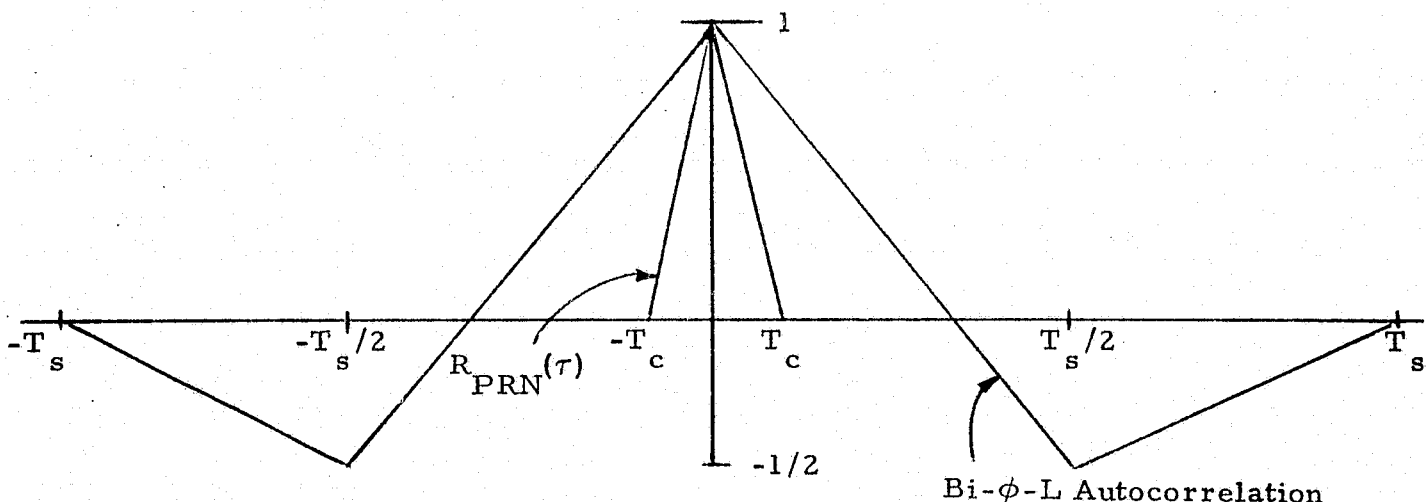


Figure C-1. Autocorrelation Functions of Bi- $\phi$ -L and PN Sequence Waveforms

In Figure C-2, the PN power spectral density and IF bandwidths are shown. The PN sequence of the present baseline system has a chip time of  $T_c = [11.232 \times 10^6]^{-1}$ . Under the assumption of an ideal BPF, the output signal-to-noise ratio is maximized when [C.1]:

$$T_c B_\Sigma / 2 = 1.37$$

so that  $B_\Sigma = 30.78$  MHz. The signal loss incurred by using an ideal BPF as opposed to a matched filter is -0.9 dB (which corresponds to a multiplicative scale factor of 0.81). With

$$S_2(0) = \gamma \frac{P_{\text{rec}}}{2} [E_\Delta^2 N_{0\Sigma} + E_s^2 N_{0\Delta}] \quad (\text{C-7})$$

where  $\gamma = 0.81$ . This loss could have been reduced to approximately 0.5 dB by using a Gaussian assumption for the IF filter shape.

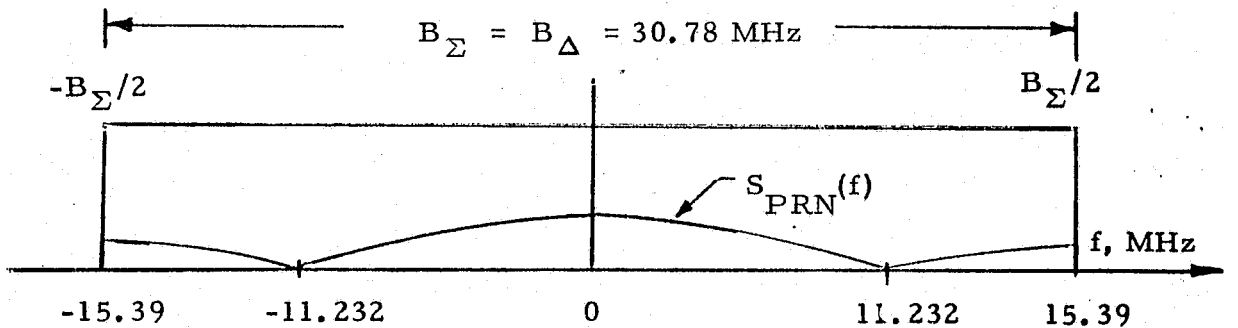


Figure C-2. PN Sequence Spectrum and IF Filter

#### Case II. PN Sequence Despread Ideally in All Channels

When the PN sequence has been despread, then

$$S_2(f) = \mathcal{F} \left\{ P_{\text{rec}} [E_\Delta^2 R_{L\Sigma}(\tau) + E_s^2 R_{L\Delta}(\tau)] \right\} . \quad (\text{C-8})$$

The data rate of the Bi- $\phi$ -L waveform is 216 kbps. This spectrum is shown in Figure C-3.

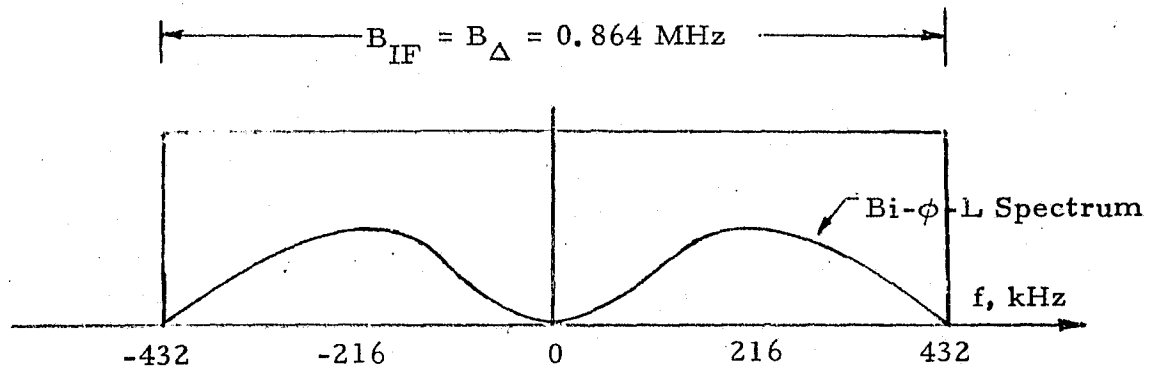


Figure C-3. Bi- $\phi$ -L Data Spectrum and IF Filter

In this case, the IF filter bandwidths can be chosen much smaller. For the sake of simplicity, we choose the bandwidth to be twice the data rate and make the assumption that the signal passes without any power loss and without distortion. In this case, the resulting RMS error is going to be so very low anyhow that these additional factors become unimportant.

The transform in (C-8) can then be evaluated at  $f=0$ , with the result that

$$S_2(0) = \frac{P_{\text{rec}}}{2} [E_{\Delta}^2 N_{0\Sigma} + E_s^2 N_{0\Delta}] \quad (\text{C-9})$$

which is the same as in Case I, except for the scale factor  $\gamma$ . The value of the IF bandwidths  $B_{\Sigma}$  and  $B_{\Delta}$  are very different, however.

Upon addition of (C-7) or (C-9) and (C-2), we have that

$$\begin{aligned} N'_{\text{eq}} &= 2 S_{n_{\text{eq}}} (0) = 2 [S_1(0) + S_2(0)] \\ &= P_{\text{rec}} N_{0\Sigma} \left[ \frac{N_{0\Sigma} B_{\Sigma}}{2 P_{\text{rec}}} + \left( \frac{N_{0\Delta}}{N_{0\Sigma}} \right) \left( \frac{N_{0\Delta} B_{\Delta}}{2 P_{\text{rec}}} \right) + \gamma E_s^2 \left( \left( \frac{E_{\Delta}}{E_s} \right)^2 + \frac{N_{0\Delta}}{N_{0\Sigma}} \right) \right]. \end{aligned} \quad (\text{C-10})$$

where

$$\gamma = \begin{cases} 0.81 & \text{for Case I } (-0.9 \text{ dB}) \\ 1 & \text{for Case II} \end{cases}$$

We can absorb  $E_s$  into  $P_{rec}$  by assuming  $E_s = 1$  without any loss of generality. The result of (C-10) is equation (30), which is used to compute the RMS angle error due to thermal noise.

### Reference

- C.1 M. Schwartz. Information Transmission, Modulation and Noise,  
2nd ed., McGraw-Hill, 1970.

## ADDENDUM D

NOISE BANDWIDTH AND DESIGN POINT  
OF ANTENNA CONTROL SYSTEM

The noise bandwidth  $B_a$  for the closed loop transfer function of the antenna control system is defined in equation (28). The linearized diagram of the angle control system in Figure 3 can be redrawn as shown in Figure D-1, where  $K_{eq}$  is the equivalent gain of the radar receiver and  $F(s)$  is the open loop control system transfer function developed in Addendum A. The equivalent gain  $K_{eq}$  of the radar receiver takes into account variations in gain due to:

- (a)  $P_{rec}$  due to the dynamic range of TDRS (or of a target in the radar mode), or due to TDRS antenna off boresight, etc.
- (b) noncoherent AGC
- (c) antenna difference channel gain  $k_m$
- (d) RF phase differences between sum and difference channels.

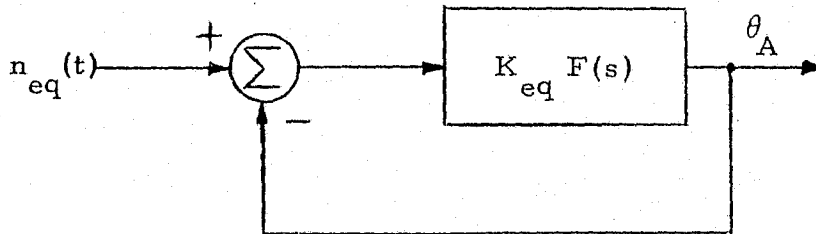


Figure D-1. Linearized Diagram of Angle Control System

The AGC and equivalent gain  $K_{eq}$  affect the RMS phase error directly via the noise spectral density  $N_{eq}$  in (29) and also via the noise bandwidth  $B_a$  of the antenna control system.

The closed loop transfer function of the linearized antenna control system in Figure D-1 is

$$H_a(s) = \frac{K_{eq} F(s)}{1 + K_{eq} F(s)} \quad (D-1)$$

where  $F(s)$  is the open loop transfer function.  $F(s)$  is given by (25) by

$$F(s) = \frac{K_L}{s(1 + b_1 s + b_2 s^2)} \quad (D-2)$$

where, from Addendum A,

$K_L$  = receiver loop gain

$b_1 = 0.045016$

$b_2 = 0.001013$ .

The constants  $b_1$  and  $b_2$  are chosen so that the open loop poles are as shown in Figure D-2. It can be seen that, for small values of loop gain, all closed loop poles will be on the  $\sigma$ -axis, so that the system will behave as a sequence of three first-order filters. Being a third-order system with no zeros, at high values of loop gain, the system will become unstable.

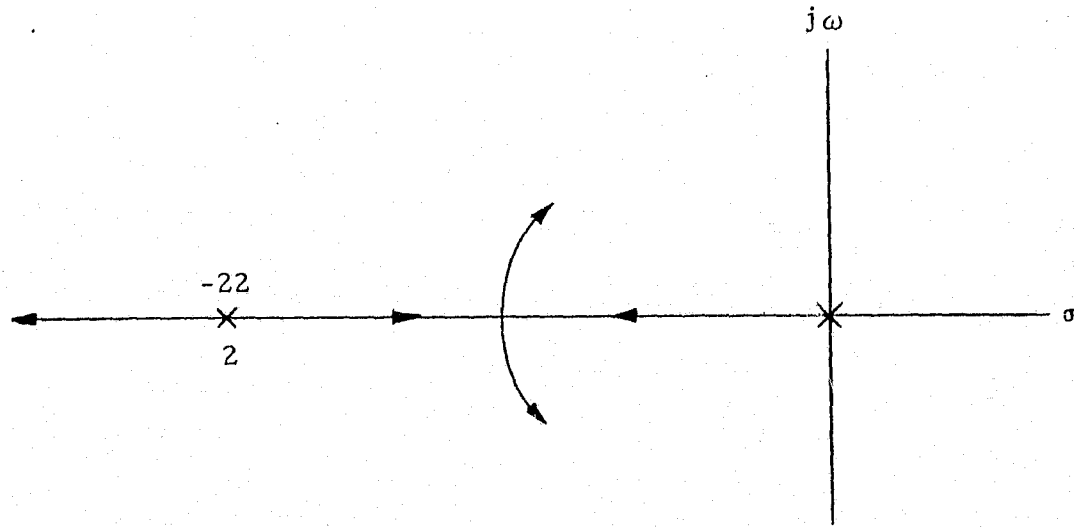


Figure D-2. s-Plane for Antenna Linear Control System

Even though  $P_{rec}$  may vary over a large range, we will see that the loop gain variation is reduced due to the operation of the noncoherent AGC, particularly at high values of signal-to-noise ratio.

The closed loop transfer function can be expressed as

$$H_a(s) = \frac{1}{1 + a_1 s + a_2 s^2 + a_3 s^3} \quad (D-3)$$

where

$$a_1 = (K_{eq} K_L)^{-1}$$

$$a_2 = b_1 (K_{eq} K_L)^{-1}$$

$$a_3 = b_2 (K_{eq} K_L)^{-1}.$$

By using [D-1], the noise bandwidth  $B_a$  can be evaluated as

$$\begin{aligned} B_a &\triangleq \int_0^\infty |H_a(j2\pi f)|^2 df \\ &= \frac{K}{4} \left[ 1 - \frac{K b_2^2}{b_1} \right]^{-1} \text{ Hertz} \end{aligned} \quad (D-4)$$

where  $K \triangleq K_{eq} K_L$ . (D-5)

Upon substitution,

$$B_a = \frac{K}{4} [1 - 0.0225K]^{-1} \text{ Hertz}, \quad K < 44.4. \quad (D-6)$$

where the restriction on  $K$  is to keep all closed loop poles in the left half of the  $s$ -plane.

With the design of the transfer function carried out as in Addendum A, the noise bandwidth is a function only of the overall loop gain  $K$ . For small values of  $K$ ,  $B_a \approx K/4$ , which agrees with the noise bandwidth for a first-order tracking loop.

The closed loop bandwidth at the design point is chosen to be  $B_a = 10 \text{ Hz}$  at Design Point 1. This corresponds to a loop gain of

$$K = 21.053 \quad (\text{D-7})$$

at Design Point 1.

The remaining parameter to be chosen at the design point is the amplifier gain  $K_L$ . This can be chosen when  $K_{eq}$  is determined at the design point. Based on the May 1976 Circuit Margins [3], the design point parameters are

$$(1) \quad \frac{P_{rec}}{N_0} = 73.2 \text{ dB-Hz} \quad (\text{D-8})$$

This could go as low as 68.2 dB-Hz, but we use the nominal value in (D-8) as the design point.

$$(2) \quad \theta_B = 2.8^\circ = 48.9 \text{ mrad} \quad (\text{D-9})$$

This corresponds to a 20" diameter antenna dish which is the smallest of those being considered.

$$(3) \quad B_\Sigma = B_\Delta = 30.78 \text{ MHz} \quad (\text{D-10})$$

This choice of IF filter bandwidth is based on the discussion in Addendum D. It is the optimal choice of IF bandwidth when the PN sequence despreaders are assumed to not be present in the angle tracking control system.

$$(4) \quad k_m = 1.57 \quad (\text{D-11})$$

This assumes nominal antenna performance.

$$(5) \quad \cos \theta_E = 1 \quad (\text{D-12})$$

The RF phase variation between the sum and difference channels is assumed to be negligible when choosing the design point parameters.

Substituting these values into (23), the receiver equivalent gain at Design Point 1 is

$$K_{eq} \Big|_{\substack{\text{Design} \\ \text{Point 1}}} = 12.98 . \quad (\text{D-13})$$

Therefore, the amplifier loop gain, discussed in Addendum A, is

$$K_L = K/K_{eq} = 1.622 \quad (\text{D-14})$$

for Design Point 1.

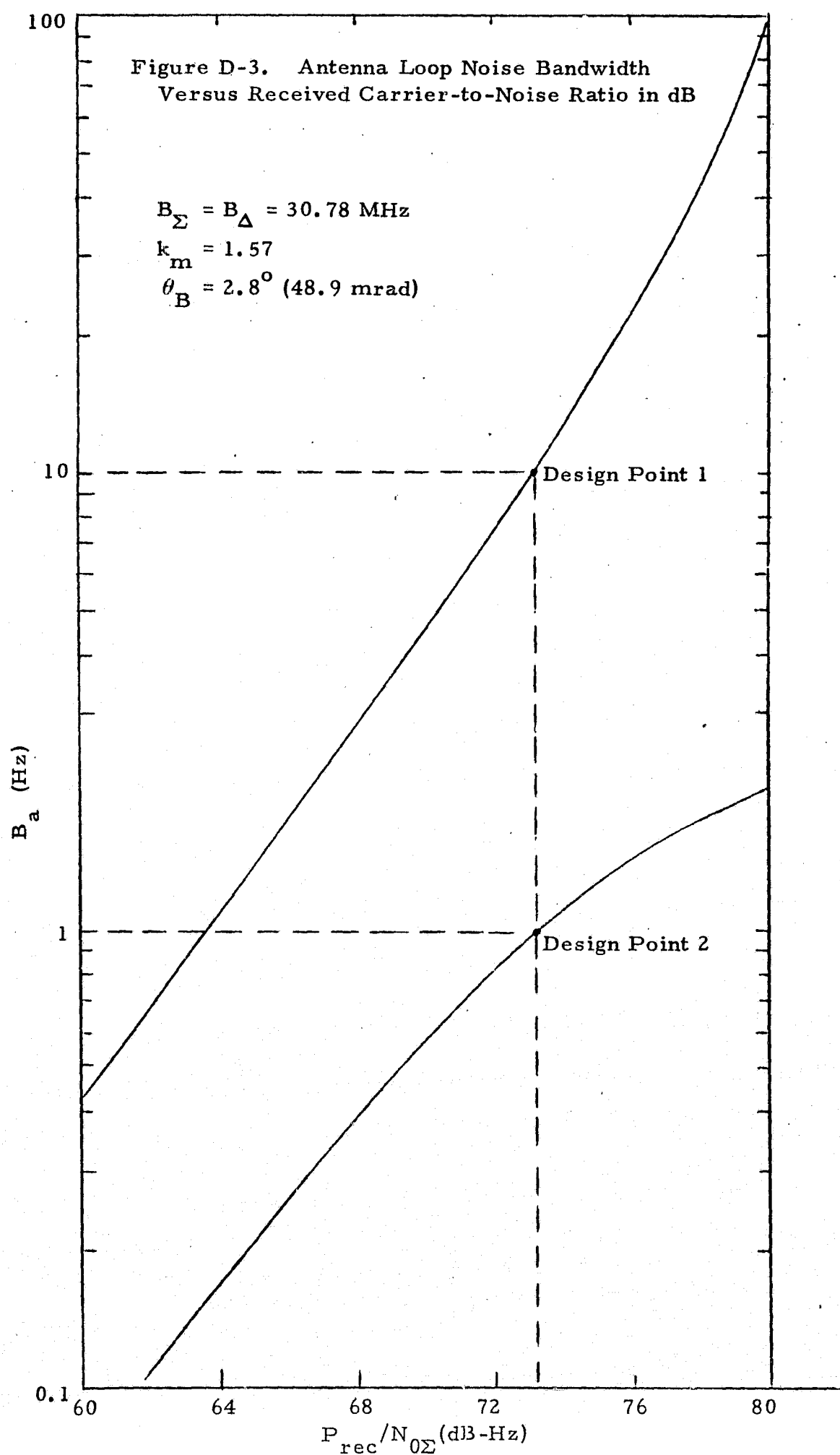
The variation of the antenna closed loop noise bandwidth  $B_a$  versus the received carrier-to-noise ratio  $P_{rec}/N_{0\Sigma}$  is shown in Figure D-3. It should be noted that, even with the AGC, there is still substantial variation of  $B_a$  with respect to  $P_{rec}/N_{0\Sigma}$ . For Design Point 1, the noise bandwidth was chosen relatively high since the carrier-to-noise ratio may undergo fades by as much as 5 dB. At  $P_{rec}/N_{0\Sigma} = 67.2$  dB-Hz, a 5 dB drop from the design point, the closed loop noise bandwidth is 2.29 Hz. This is still a satisfactory bandwidth. Smaller values of  $B_a$  would also be acceptable, since target and TDRS motion are expected to be very small.

Note that the inertial stabilization capability is not affected by variations in  $P_{rec}/N_{0\Sigma}$  (see Addendum A).

The value of  $B_a = 10$  Hz was conservatively chosen. By demonstrating that excellent tracking performance can be expected with  $B_a = 10$  Hz and a 20" diameter antenna, larger antenna diameter and smaller noise bandwidth will provide better tracking performance.

The variation of  $B_a$  in Figure D-3 gives the appearance that the AGC is not functioning. The large variation is due to the fact that the AGC is noncoherent and is operating at low values of signal-to-noise ratio. For example, at  $P_{rec}/N_{0\Sigma} = 73.2$  dB-Hz and  $B_\Sigma = 30.78$  MHz, the IF signal-to-noise ratio is  $P_{rec}/(N_{0\Sigma} B_\Sigma) = -1.68$  dB. At this point and at lower values of  $P_{rec}/N_{0\Sigma}$ , the AGC is operating primarily on the noise alone. At higher values of 1F SNR, the noise bandwidth would vary negligibly.

Figure D-3. Antenna Loop Noise Bandwidth  
Versus Received Carrier-to-Noise Ratio in dB



A second design point is also shown in Figure D-3, namely,  $B_a = 1 \text{ Hz}$  at  $P_{\text{rec}}/N_{0\Sigma} = 73.2 \text{ dB-Hz}$ . In this case,  $K_L = 0.2827$ , and the variation in  $B_a$  is not as great. At higher values of  $P_{\text{rec}}/N_{0\Sigma}$ , the effect of the AGC can be seen. Again because the noncoherent AGC is operating at low values of SNR, its effect is negligible. For Design Point 2, the overall loop gain is lower, so that the effects of the additional poles in the open loop antenna transfer function are not as effective as for Design Point 1. This also explains why the AGC appears to never be effective for Design Point 1.

In this Addendum, the variation of the antenna closed loop noise bandwidth with respect to the received carrier-to-noise ratio is determined. The variation is about a design point which is chosen based on the most recent circuit margin [3] available.

#### Reference

- D.1. Gradshteyn and Ryzhitz. Table of Integrals, Series and Products, Academic Press, 1965, p. 218.

## APPENDIX M

## SPIRAL SCAN ANALYSIS

by

Gaylord K. Huth  
Sergei Udalov

This appendix analyzes the relationship between the dwell time, the total scan time, and the scan rate for the following types of spiral scans:

- (1) spiral scan with constant rotational velocity;
- (2) spiral scan with constant tangential velocity;
- and (3) hybrid scan which starts out with constant rotational velocity and then switches over to constant tangential velocity.

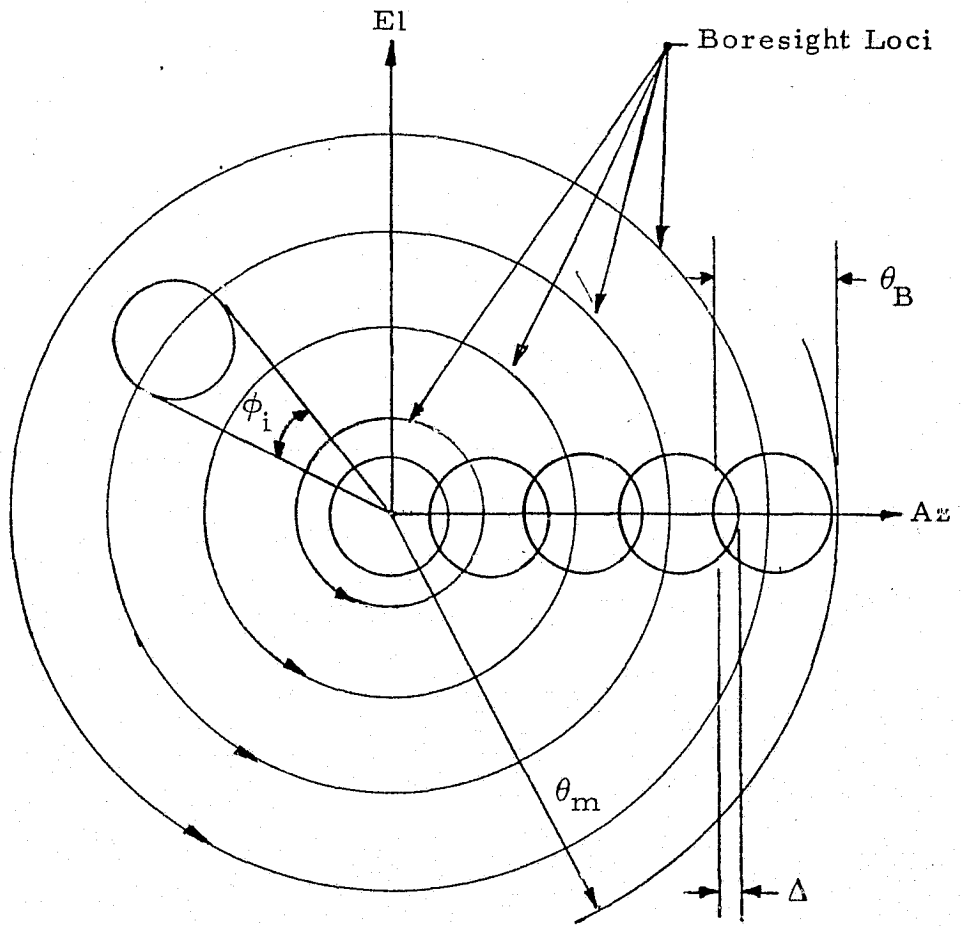
It will be shown that the hybrid spiral scan offers the best compromise between the antenna servo power requirements and the dwell time. Several numerical examples pertinent to the Shuttle Ku-band radar/communication system are provided.

## 1.0 INTRODUCTORY ANALYSIS - STEPPED CIRCULAR SCAN

Before considering the spiral scan, it is instructive to develop first the relationship between the major parameters for the stepped circular scan, which is a discrete approximation of the continuous spiral scan. Figure 1 defines the basic parameters of the stepped circular scan. After each complete rotation about boresight, the antenna is stepped to the next radius for the next rotation. The number of complete rotations  $N$  can be found by noting that

$$\theta_m = \frac{\theta_B}{2} + N\theta_B(1 - \Delta) \quad (1)$$

where  $\theta_m$  is maximum scan limit,  $\theta_B$  is the antenna beamwidth, and  $\Delta$  is the scan overlap. Equation (1) can be rewritten to determine  $N$ :



$\theta_B$  = beamwidth (3 dB)

$\theta_m$  = maximum scan limit

$\Delta$  = beam overlap

$\phi_i$  = angle of antenna dwell  
on ith rotation

Figure 1. Stepped Circular Scan Increases the Dimensions of Boresight Loci by Discrete Increments

$$N = \left\lceil \frac{\theta_m - \frac{\theta_B}{2}}{\theta_B(1 - \Delta)} \right\rceil \quad (2)$$

where  $[x]$  is the largest integer greater than  $x$ .

The dwell time on the  $i^{\text{th}}$  rotation is denoted by  $t_{d_i}$  and is given by

$$t_{d_i} = \frac{\phi_i}{f_i 2\pi} = \frac{4}{f_i 2\pi} \sin^{-1} \frac{\theta_B}{4i\theta_B(1 - \Delta)} = \frac{2}{f_i \pi} \sin^{-1} \frac{1}{4i(1 - \Delta)} \quad (3)$$

where  $f_i$  is the rotational frequency (i.e., revolutions per second) for the  $i^{\text{th}}$  revolution and the radius of the  $i^{\text{th}}$  revolution is  $i\theta_B(1 - \Delta)$ . Note that, for reasonable values of  $\Delta$  (i.e., 30% or less), equation (3) can be rewritten as

$$t_{d_i} \approx \frac{1}{f_i 2\pi i(1 - \Delta)} \quad (4)$$

with only a 2.2% error or less for  $i=1$  and 0.5% error or less for  $i=2$ .

The total scan time  $T_s$ , i.e., the time required to reach the scan limit boundary  $\theta_m$  is

$$T_s = t_{d_0} + \sum_{i=1}^N \frac{1}{f_i} + N\tau \quad (5)$$

where  $t_{d_0}$  is the dwell time on the beamwidth at boresight and  $\tau$  is the time to step between scan radii. For constant rotational velocity  $f_c$ ,

$$T_s = t_{d_0} + N\left(\frac{1}{f_c} + \tau\right) = t_{d_0} + \frac{\theta_m - \frac{\theta_B}{2}}{\theta_B(1 - \Delta)} \left(\frac{1}{f_c} + \tau\right). \quad (6)$$

For constant tangential velocity,

$$t_{d_0} = t_{d_i} \approx \frac{1}{f_i 2\pi i(1 - \Delta)} \quad (7)$$

or

$$f_i \approx \frac{1}{t_{d_0} 2\pi i(1 - \Delta)} \quad (8)$$

$$\text{Therefore, } T_s = t_{d_0} \left[ 1 + 2\pi(1 - \Delta) \sum_{i=1}^N i \right] + N\tau$$

$$= t_{d_0} \left[ 1 + \pi(1 - \Delta) N(N+1) \right] + N\tau . \quad (9)$$

But, using equation (2) for N,

$$N(N+1) = \frac{\theta_m^2 - \theta_m \theta_B \Delta - \frac{\theta_B^2}{4}(1 - 2\Delta)}{\theta_B^2(1 - \Delta)^2} . \quad (10)$$

Hence, for constant tangential velocity,

$$T_s = t_{d_0} \left[ 1 + \pi \left( \frac{\theta_m^2 - \theta_m \theta_B \Delta - \frac{\theta_B^2}{4}(1 - 2\Delta)}{\theta_B^2(1 - \Delta)} \right) \right] + \frac{\theta_m - \frac{\theta_B}{2}}{\theta_B(1 - \Delta)} \tau . \quad (11)$$

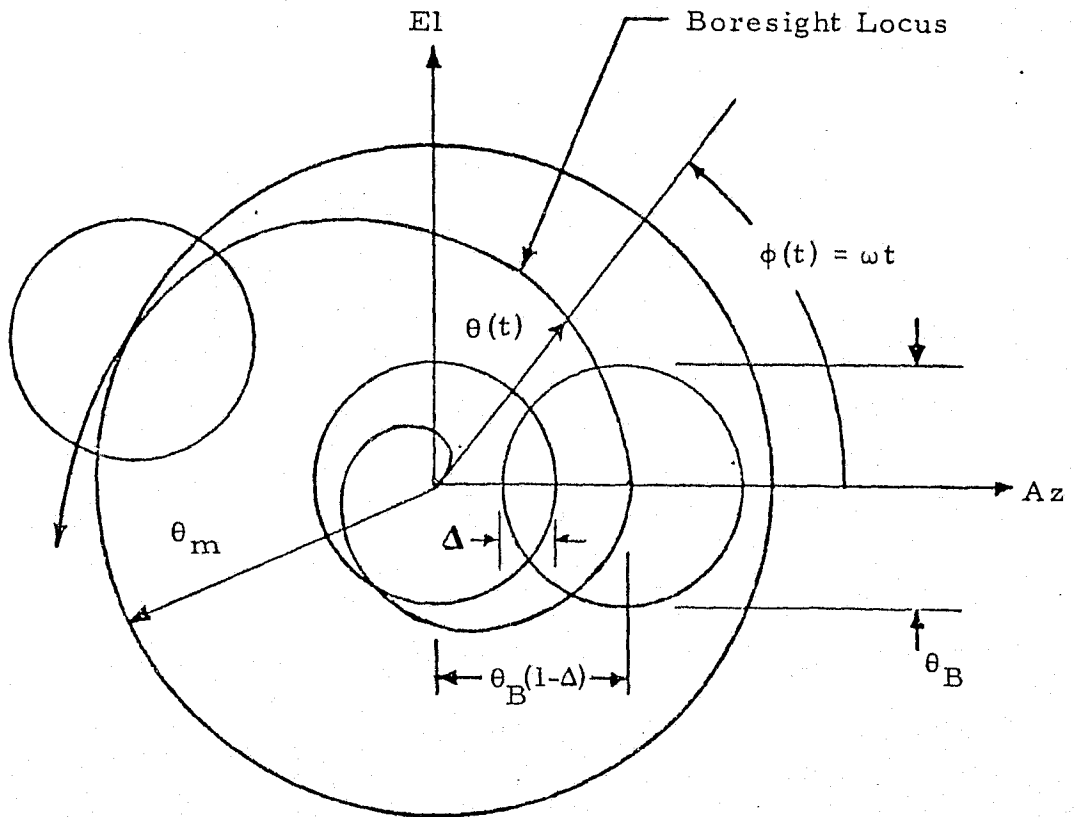
## 2.0 CONSTANT ROTATIONAL VELOCITY SPIRAL SCAN

With the antenna axis and the monopulse comparator arranged for tracking along two orthogonal axes, such as Az and El, the spiral scan can be implemented by driving each axis with an orthogonal sinusoid of progressively increasing amplitude. The boresight displacement along each of the orthogonal axes is then

$$\begin{aligned} \Delta Az &= \theta(t) \cos \omega t \\ \Delta El &= \theta(t) \sin \omega t \end{aligned} \quad (12)$$

where  $\theta(t)$  is the time-dependent function which determines radial boresight displacement and  $\omega = 2\pi f_s$  = angular rate of boresight displacement. The  $f_s$  will be referred to henceforth as the "scan frequency." This frequency may be equal to or may be smaller than the servo bandwidth, but it should not exceed the latter.

In polar coordinates, the boresight locus is defined by a spiral  $\theta(t) < \phi(t)$  shown in Figure 2. In Figure 2,  $\theta_B(1 - \Delta)$  is the boresight displacement per one complete turn of  $\phi(t)$ .



$$\theta_B(1 - \Delta) = \text{deg/rev}$$

$\theta_B$  = beamwidth (3 dB)

$\theta_m$  = maximum scan limit

$\Delta$  = beam overlap

Figure 2. Spiral Scan Increases the Dimension of the Boresight Locus in a Continuous Manner

Let  $\theta(t)$  be proportional to  $\phi(t)$ . Then,  $\theta(t)$  is given by

$$\theta(t) = \frac{\theta_B(1-\Delta)}{2\pi} \phi(t) = \frac{\theta_B(1-\Delta)}{2\pi} \omega t = \theta_B(1-\Delta) f_s t. \quad (13)$$

From (13), we can determine the time  $T_s$  required to spiral out the boresight to any given maximum angular (conical) limit,  $\theta_m$ . Thus,

$$T_s = \frac{\theta_m - \frac{\theta_B}{2}}{f_s \theta_B(1-\Delta)}. \quad (14)$$

Equation (14) can be used directly only if  $f_s$  (i.e., scan frequency) is constant. Note that (14) is very close to (6) for the stepped circular scan with  $\tau$  equal to 0. Thus, (14) applies to a constant angular velocity scan. For a constant tangential velocity,  $f_s$  is time-dependent and (14) has to be modified accordingly, as explained in Section 3.0.

As the boresight position spirals out toward a given maximum limit, the dwell time decreases if the  $\omega$  is held constant. The dwell time can be computed by considering the tangential\* velocity along the spiral at the corresponding value of  $\theta(t)$ . Thus,

$$V_t = \theta(t) \omega. \quad (15)$$

The dwell time is then considered as the time required by a predetermined antenna beamwidth contour,  $\theta_B$  (-1 dB or -3 dB, etc.) to traverse a direction in space as the boresight moves across that direction with velocity  $V_t$ ,

$$t_d = \frac{\theta_B}{V_t} = \frac{\theta_B}{\theta(t) \omega} = \frac{\theta_B}{\theta_B(1-\Delta) f_s \omega t} = \frac{1}{2\pi} \frac{\theta_B}{\theta_B(1-\Delta)} \left(\frac{1}{f_s}\right)^2 \frac{1}{t}. \quad (16)$$

Of particular importance is the dwell time available at the position where the boresight reaches the maximum scan limit  $\theta_m$ . The expression

---

\* The radial component due to spiraling out is not included here because it is generally low compared to the tangential component of the total velocity along the spiral.

for the value of this dwell time is obtained by substituting (14) into (16):

$$t_{dm} = \frac{1}{2\pi} \frac{\theta_B}{\theta_B(1-\Delta)} - \frac{1}{2} \frac{\theta_B(1-\Delta)}{\theta_m - \frac{\theta_B}{2}} = \frac{1}{2\pi f_s} \frac{\theta_B}{\theta_m - \frac{\theta_B}{2}} . \quad (17)$$

Equations (13) and (16) can be used to plot the angle scanned and the corresponding dwell time as a function of time and scan frequency,  $f_s$ . Correspondingly, equations (14) and (17) can be used to plot the maximum time to reach the scan limit,  $\theta_m$ , and the corresponding  $t_{dm}$  as the function of  $f_s$ .

### 3.0 CONSTANT TANGENTIAL VELOCITY SPIRAL SCAN

For a spiral scan with constant tangential velocity  $V_t$ , from (15) with  $\omega = 2\pi f_s$ ,

$$V_t = 2\pi f_s \theta(t) \quad (18)$$

where  $\theta(t)$  is the instantaneous radius given by (13). Hence,

$$V_t = 2\pi \theta_B(1-\Delta) f_s^2 t . \quad (19)$$

The total scan time  $T_s$  can be found from (5) for the circular scan by letting  $\tau$  equal zero and the sum be an integral over the continuously changing  $\theta(t)$ . Therefore, note that maximum value of  $\theta(t)$  is

$$\max \theta(t) = \theta_m - \frac{\theta_B}{2} . \quad (20)$$

The instantaneous number of turns completed,  $n$ , is the total radius the spiral has reached divided by the advance per turn. That is,

$$n = \frac{\theta(t)}{\theta_B(1-\Delta)} \quad (21)$$

and the incremental increase is

$$dn = \frac{d\theta(t)}{\theta_B(1-\Delta)} . \quad (22)$$

Thus, the sum in (5) becomes the integral

$$T_s = \int_0^{\theta_m - \theta_B/2} \frac{1}{f_s} \frac{d\theta(t)}{\theta_B(1-\Delta)} . \quad (23)$$

Neglecting the radial component due to spiraling out, then from (16),

$$t_d = \frac{\theta_B}{V_t} = \frac{\theta_B}{2\pi f_s \theta(t)} \quad (24)$$

or

$$f_s = \frac{\theta_B}{2\pi t_d \theta(t)} . \quad (25)$$

Substituting (25) into (23) results in

$$T_s = \frac{2\pi t_d}{\theta_B^2(1-\Delta)} \int_0^{\theta_m - \theta_B/2} \theta(t) d\theta(t) . \quad (26)$$

Also, note that by substituting (25) into (13), one obtains

$$\theta^2(t) = \frac{\theta_B^2(1-\Delta)t}{2\pi t_d} . \quad (27)$$

Therefore,

$$\theta(t) d\theta(t) = \frac{\theta_B^2(1-\Delta) dt}{4\pi t_d} \quad (28)$$

and by rearranging (27),

$$t = \frac{2\pi t_d \theta^2(t)}{\theta_B^2(1-\Delta)} . \quad (29)$$

The maximum value of  $t$  is

$$\max t = \frac{2\pi t_d (\theta_m - \theta_B/2)^2}{\theta_B^2(1-\Delta)} . \quad (30)$$

Substituting (28) and (30) into (26) gives

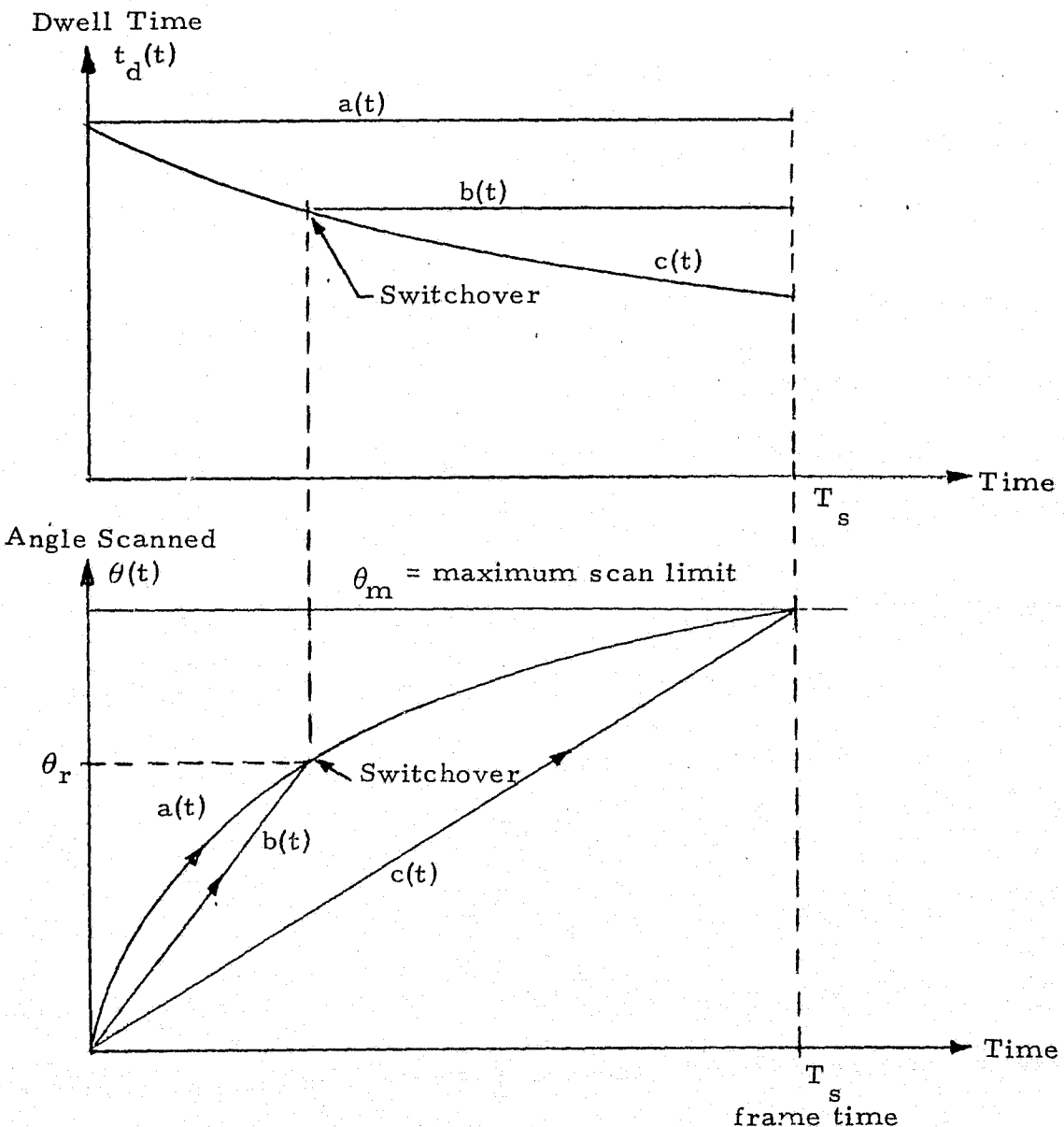
$$\begin{aligned} T_s &= \frac{1}{2} \int_0^{\max t} dt \\ &= \frac{\pi t_d (\theta_m - \theta_B/2)^2}{\theta_B^2(1-\Delta)} \end{aligned} \quad (31)$$

which is very close to the result for stepped circular scan with  $\tau$  equal to zero.

#### 4.0 HYBRID SPIRAL SCAN

The design of a scan procedure typically requires the maximization of the dwell time for a given total scan time  $T_s$ . Figure 3 compares the dwell time for a spiral scan with constant rotational velocity [i.e., scan  $c(t)$ ] and constant tangential velocity [i.e., scan  $a(t)$ ]. It can be seen that constant tangential velocity maximizes the dwell time but at  $\theta(t) = 0$ , it requires infinite rotational velocity as predicted by (25). Therefore, to overcome the infinite rotational velocity at  $\theta(t)$  and to increase the dwell time from that obtained by constant rotational velocity, a hybrid scan technique is proposed. The hybrid scan is shown in Figure 3 [i.e., scan  $b(t)$ ] where initially the scan is performed at a constant rotational velocity and then is switched over to constant tangential velocity. To compute the total scan time of the hybrid scan, let the constant rotational velocity scan switch over to the constant tangential velocity scan at  $\theta_r$ . Therefore, the radius at switchover is

$$\theta_s(t) = \theta_r - \frac{\theta_B}{2} . \quad (32)$$



Scan  $a(t)$ :  $f_s(0)$  infinite and then progressively decreases to maintain constant  $t_d$ .

Scan  $b(t)$ :  $f_s$  constant until switchover, then decreased to maintain constant  $t_d$  for the remaining portion of the scan.

Scan  $c(t)$ :  $f_s$  constant to  $T_s$  but  $t_d$  decreased continuously.

Figure 3. Scanned Angle and Dwell Time for Constant Tangential Velocity  $a(t)$ , Hybrid  $b(t)$ , and Constant Rotational Rate  $c(t)$  Spiral Scans

The total scan time  $T_s$  is composed of the constant rotational velocity scan time  $T_{sr}$  and the constant tangential velocity scan time  $T_{sv}$ . From (14) and (26),

$$\begin{aligned} T_s &= T_{sr} + T_{sv} \\ &= \frac{\theta_r - \frac{\theta_B}{2}}{\theta_B(1-\Delta)f_s} + \frac{2\pi t_d}{\theta_B^2(1-\Delta)} \int_{\theta_r - \theta_B/2}^{\theta_m - \theta_B/2} \theta(t) d\theta(t). \end{aligned} \quad (33)$$

Making the substitutions similar to equations (27) to (31),

$$T_s = \frac{\theta_r - \frac{\theta_B}{2}}{\theta_B(1-\Delta)f_s} + \frac{\pi t_d}{\theta_B^2(1-\Delta)} [(\theta_m - \theta_B/2)^2 - (\theta_r - \theta_B/2)^2]. \quad (34)$$

For any given initial constant rotational velocity  $f_s$  and any final dwell time the following boundary condition from (17) must hold

$$t_d = \frac{1}{2\pi f_s} \frac{\theta_B}{\theta_r - \frac{\theta_B}{2}} \quad (35)$$

or

$$\theta_r - \frac{\theta_B}{2} = \frac{\theta_B}{2\pi f_s t_d}. \quad (36)$$

Therefore, for given  $f_s$  and  $t_d$ , the half-cone angle reached at switchover is

$$\theta_r = \frac{\theta_B}{2} \left[ \frac{1}{\pi f_s t_d} + 1 \right] \quad (37)$$

Substituting (36) into (34)

$$T_s = \frac{1}{4\pi(1-\Delta)f_s^2 t_d} + \frac{\pi t_d (\theta_m - \theta_B/2)^2}{\theta_B^2(1-\Delta)}. \quad (38)$$

Note that the second term in (38) is the same as (31). Thus, for a given  $t_d$ , the hybrid scan requires a total scan time greater than the constant tangential velocity scan by the addition of the first term in (38). If  $f_s = \infty$ , then (38) becomes the constant tangential velocity result in (31). Alternatively,  $t_d$  can be found for a given  $T_s$  by rewriting (38) as

$$\frac{\pi(\theta_m - \theta_B/2)^2}{\theta_B^2(1 - \Delta)} t_d^2 - T_s t_d + \frac{1}{4\pi(1 - \Delta) f_s^2} = 0 \quad (39)$$

and solving this quadratic equation for  $t_d$ . It is important to point out that solution of (39) for  $t_d$  depends not only on  $T_s$  but also on such parameters as  $\theta_m$ ,  $\theta_B$ , and  $f_s$ . Because  $T_s$  and  $\theta_m$  are generally fixed for a given mission, maximizing  $t_d$  for a particular value of  $\theta_B$  can be performed by analyzing the relationship between  $t_d$  and  $f_s$ . Such analysis reveals the minimum value of  $f_s$  yielding an acceptable value of  $t_d$ . In the next section, several numerical examples of such an analysis are presented, with particular emphasis on Shuttle Ku-band radar/communication system parameters.

## 5.0 NUMERICAL EXAMPLES

In the preceding sections, the analytical relationships for various spiral scan strategies were developed. It was shown that the hybrid scan provides an optimum compromise between excessive servo requirements and dwell time. We will now use the analytical results to obtain numerical data pertinent to hybrid spiral scan such as may be employed by Shuttle Ku-band radar/communication equipment during acquisition. Specifically, we will use equation (39) to obtain the values of dwell time  $t_d$  as a function of  $f_s$  for a set of various mission-dependent parameters  $T_s$  and  $\theta_m$  and for antenna sizes ranging from 20 inches to 36 inches in diameter. Specific mission-dependent parameters for Shuttle Ku-band equipment are:

$$(1) \quad \theta_m = \pm 30^\circ$$

$$(2) \quad \theta_m = \pm 20^\circ$$

$$(3) \quad \theta_m = \pm 10^\circ$$

The first two are characteristic of radar acquisition for a passive target. The third ( $\theta_m = 10^\circ$ ) scan limit parameter is typical of cooperative target acquisition in the radar mode and TDRS acquisition in the communication mode.

Figures 4 through 7 show the solution of (39) for  $t_d$  as a function of the scan frequency  $f_s$  and the mission-dependent parameters  $T_s$  and  $\theta_m$ . The most significant result evident from these figures is that, at the scan frequency of 2 Hz, the dwell times for all cases considered are near their maxima and exhibit only an insignificant increase at higher values of  $f_s$ .

As can be expected, the case of  $\theta_m = \pm 30^\circ$  and  $T_s = 30$  seconds sets the lower limit on  $f_s$  for all dish sizes considered. This is because, in this case, the antennas have to scan the maximum value within the minimum allotted time. Hence, the  $f_s$  has to be relatively "fast" to spiral the beams across the scan volume determined by the  $\theta_m$  limits.

Figure 8 shows the minimum dwell time available from the hybrid scan versus antenna dish size and the sets of mission-dependent parameters used. Essentially, these "minimum" dwell times are taken at  $f_s = 2$  Hz, because above this frequency there is no significant gain in the dwell time. The 2 Hz frequency, however, is within the operating range of typical antenna servo drives.

## 6.0 CONCLUSIONS

Analytical expressions for various types of spiral scans have been derived and the hybrid scan appears to be most efficient from the standpoint of minimizing servo loop loading required to achieve "best" (i.e., longest) dwell times for any given set of parameters. Specific numerical examples

indicate that a 2 Hz scan frequency should meet the dwell time optimization requirements for most missions performed by Shuttle Ku-band radar/communication equipment.

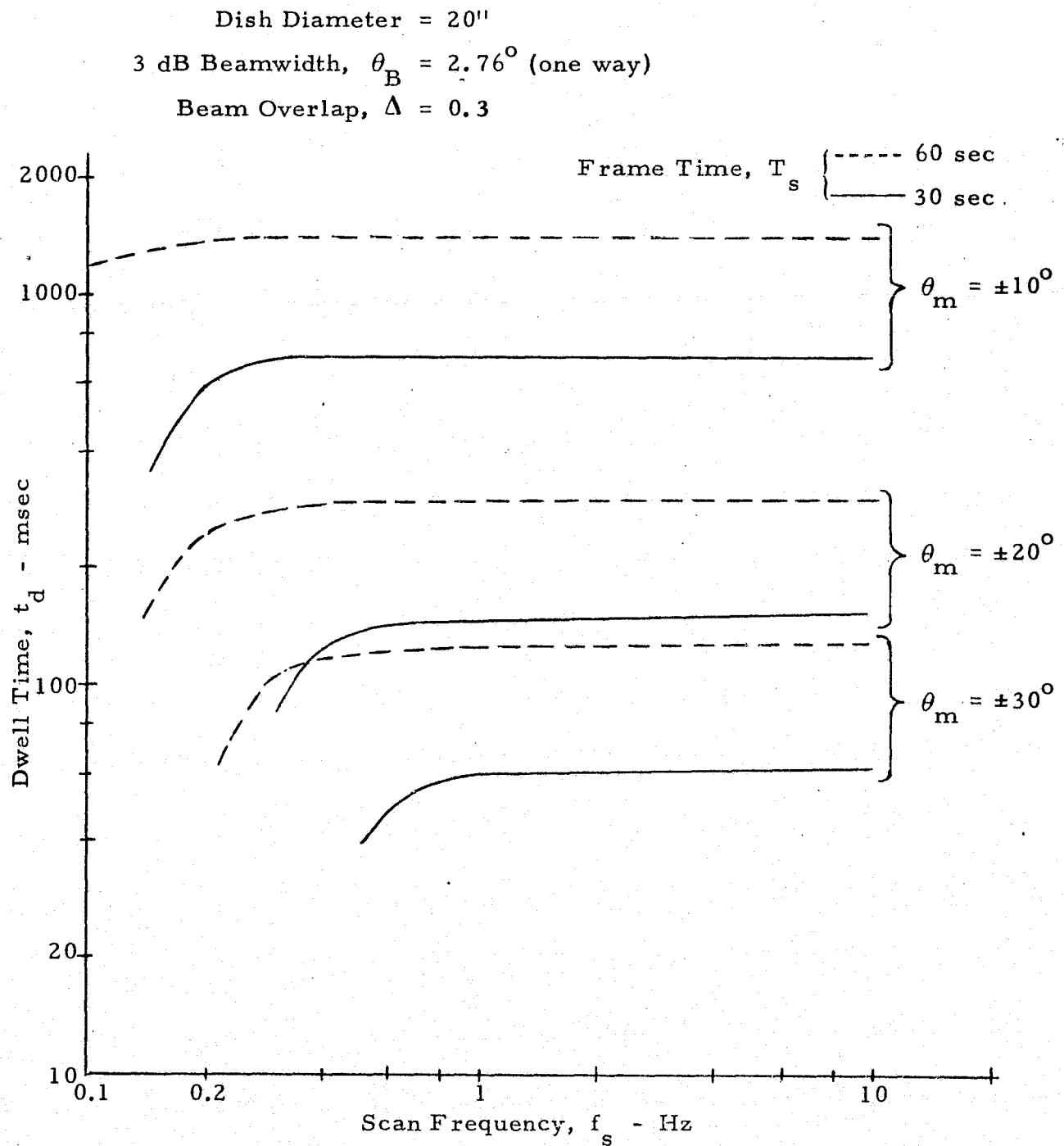


Figure 4. Dwell Time  $t_d$  Versus Scan Frequency  $f_s$  and Frame Time  $T_s$  for 20" Diameter Antenna Dish

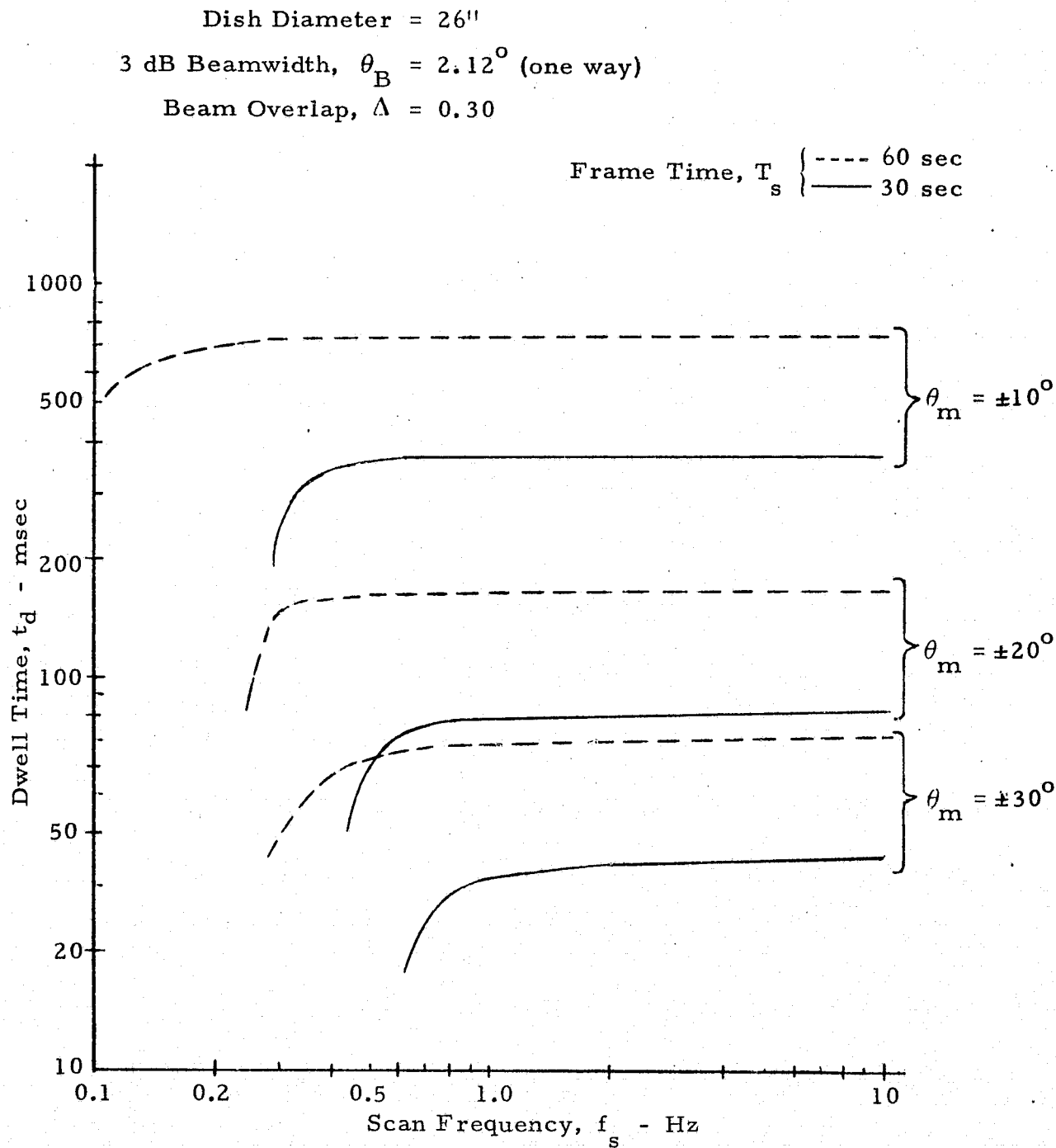


Figure 5. Dwell Time  $t_d$  Versus Scan Frequency  $f_s$  and Frame Time  $T_s$  for 26" Diameter Antenna Dish

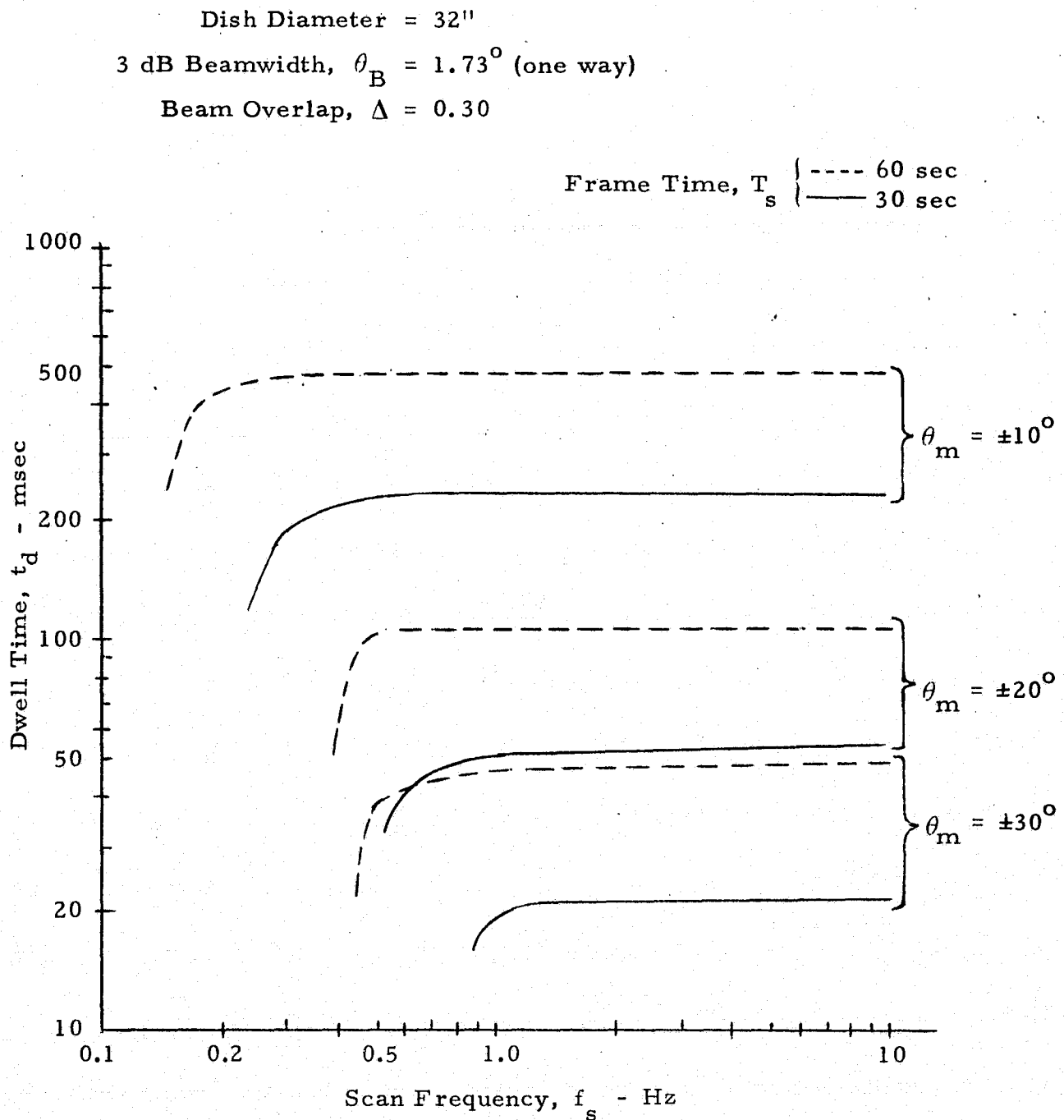


Figure 6. Dwell Time  $t_d$  Versus Scan Frequency  $f_s$  and Frame Time  $T_s$  for 32" Diameter Antenna Dish

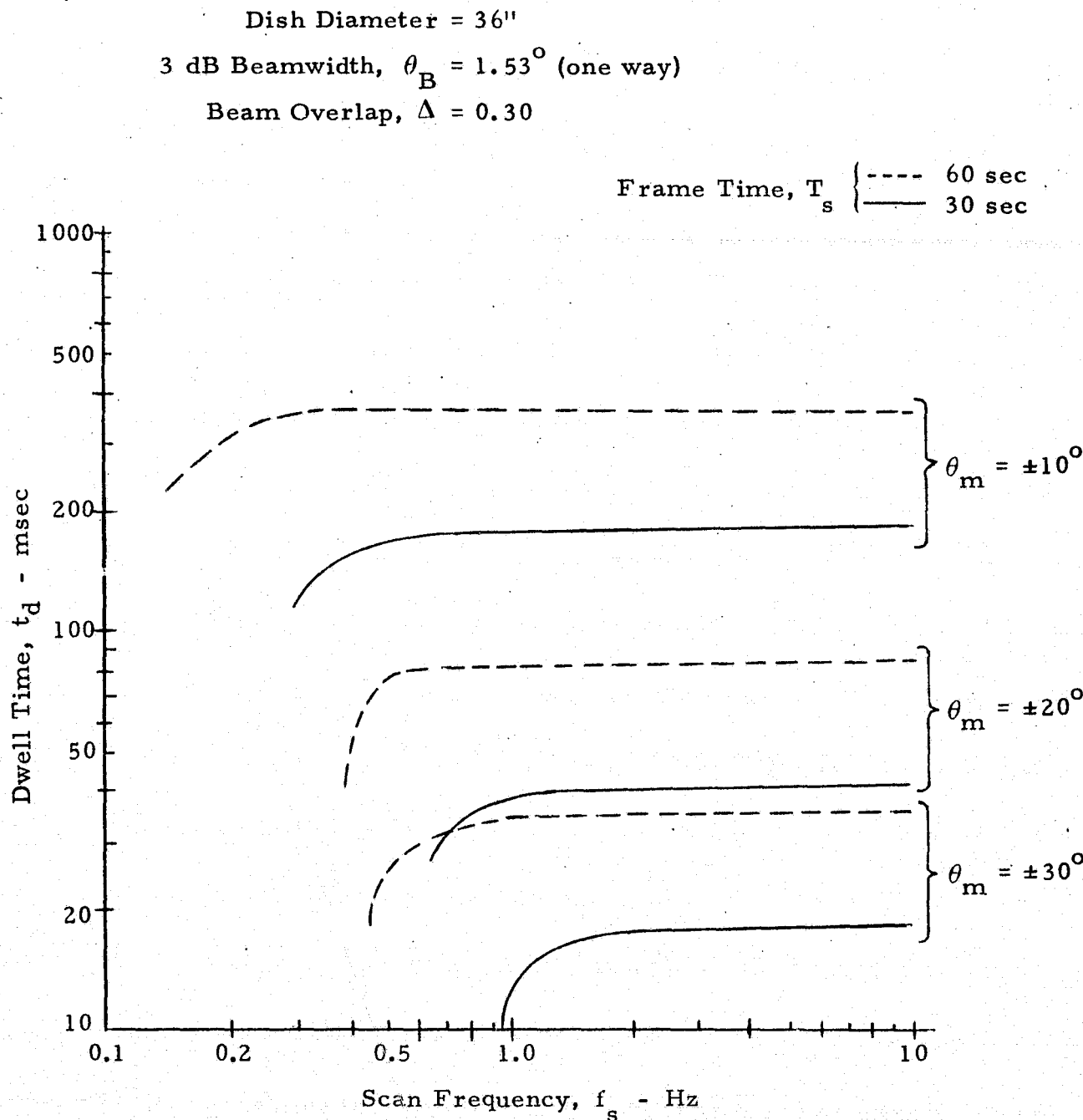


Figure 7. Dwell Time  $t_d$  Versus Scan Frequency  $f_s$  and Frame Time  $T_s$  for 36" Diameter Antenna Dish

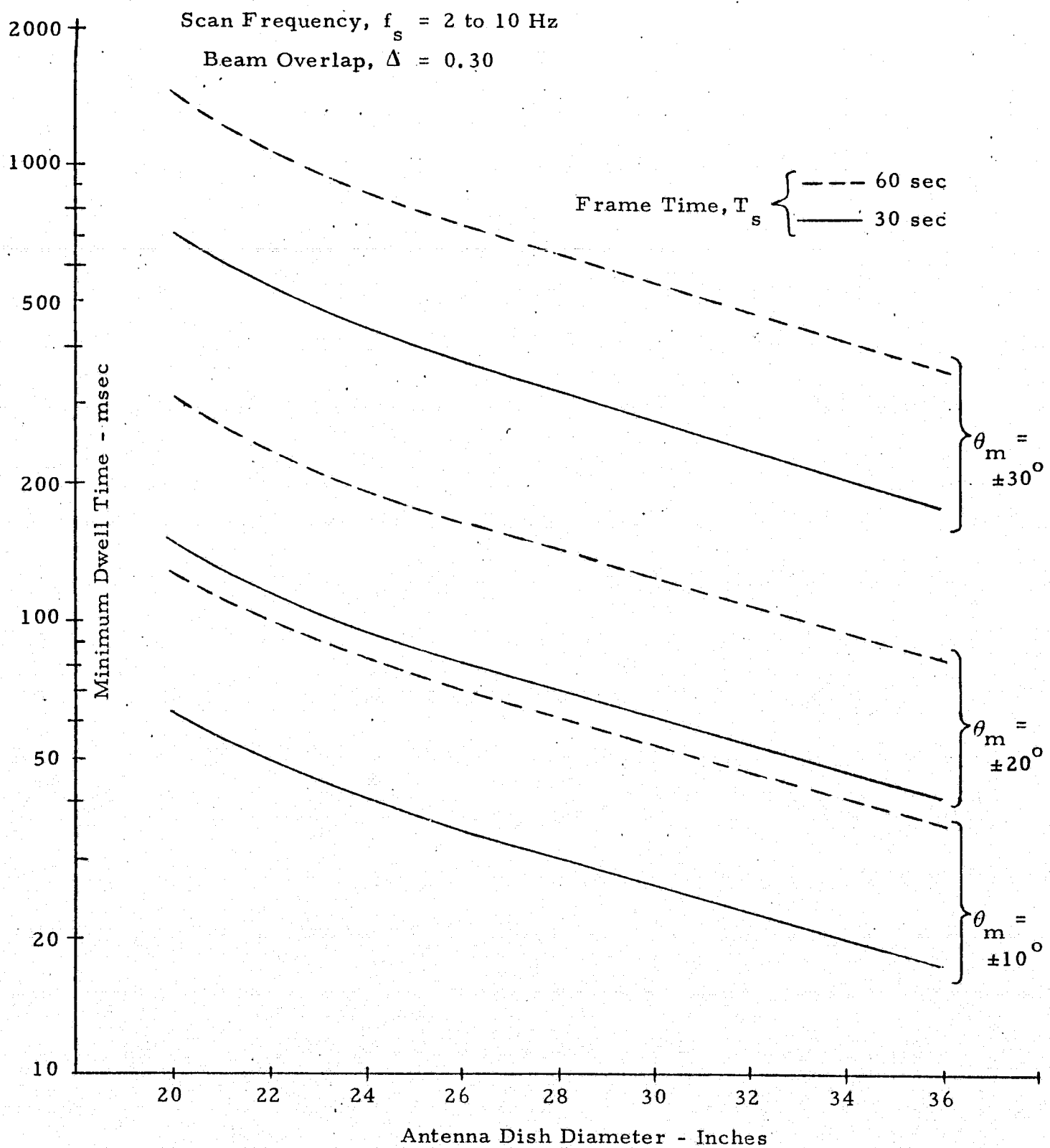


Figure 8. Minimum Dwell Time Versus Dish Diameter, Frame Time, and Maximum Scan Angle for  $f_s$  Range of 2 to 10 Hz

## APPENDIX N

POWER BUDGETS FOR PASSIVE TARGET DETECTION -  
PULSE DOPPLER RADAR

Sergei Udalov

## 1.0 INTRODUCTION

In this appendix, we consider the power requirements for passive target detection with a pulse doppler radar system. The power requirements are based on the power budget which takes into account such factors as antenna dimensions, system losses, and mission-dependent parameters, such as angular search limits ( $\pm \theta_m$ ) and the search frame time ( $T_s$ ). The analysis is based on the use of hybrid spiral scan for angular search and doppler filter bank for signal detection. Two basic mission-dependent modes are considered. These are:

- (1) Range = 22.2 km (12 nmi), search limit  $\theta_m = \pm 20^\circ$ .
- (2) Range = 14.8 km (8 nmi), search limit  $\theta_m = \pm 30^\circ$ .

In addition to these two basic modes, another mode is considered where the search limit is set at  $\pm 30^\circ$  regardless of range. It is shown that the latter mode imposes additional power requirements for detection at 22.2 km, particularly if the antenna dimensions are limited to a 20" diameter dish.

Consistent with the previously established criteria, the total detection time is assumed to be 60 sec, the time which can be allotted either to a single scan or to two consecutive scans, each of 30 sec duration. The total probability of detection for the 60 sec interval is 0.99 and the average false alarm rate is one per hour.

To make the results most general, the power requirements are estimated for several antenna sizes ranging from 20" to 36" in diameter. Also, the results are presented in a format which accounts primarily for the losses associated with the pulse doppler radar detection and the power required for the detection is shown in terms of all the other additional total system losses. These additional system losses may consist of such terms as RF losses, field degradation, threshold loss, etc.

## 2.0 ANTENNA SIZE FACTOR

Antenna size plays an important twofold role in determining the power requirements for passive target detection. First, it is obvious that increasing the diameter of the antenna dish increases the gain and thus reduces the transmitter power requirements for the initial detection, as well as for the subsequent acquisition and tracking. On the other hand, increasing antenna diameter reduces the beamwidth, which in turn reduces the dwell time on target as the antenna beam is scanned over the volume determined by the angular search limits.

The gain of the parabolic dish antenna is approximately proportional to the area, and hence proportional to the square of the antenna diameter. The dwell time is approximately proportional to the antenna beamwidth which varies as an inverse function of antenna diameter.

Figure 1 shows the relationship between the antenna gain and the one-way beamwidth (3 dB) as a function of antenna dish diameter at 15 GHz. The data for Figure 1 was extrapolated for larger dishes from the parameters of the baseline system's 20" diameter dish. The beamwidth data of Figure 1 was then used in Appendix M to calculate the corresponding dwell times for several typical dish sizes. Table 1 shows the dwell times as a function of dish diameter, frame time and scan limits. This data is for a hybrid spiral scan. Note that, because the scan is performed over the volume determined by the scan limits, the dwell time decreases approximately proportionally to the inverse of the square of the dish diameter.

The antenna gain (in dB) enters twice into the radar equation and thus the net power reduction is still obtained with the larger dishes. This increase, however, is also influenced by such secondary factors as integration loss, frame times, etc. These factors are included in the power estimates discussed below.

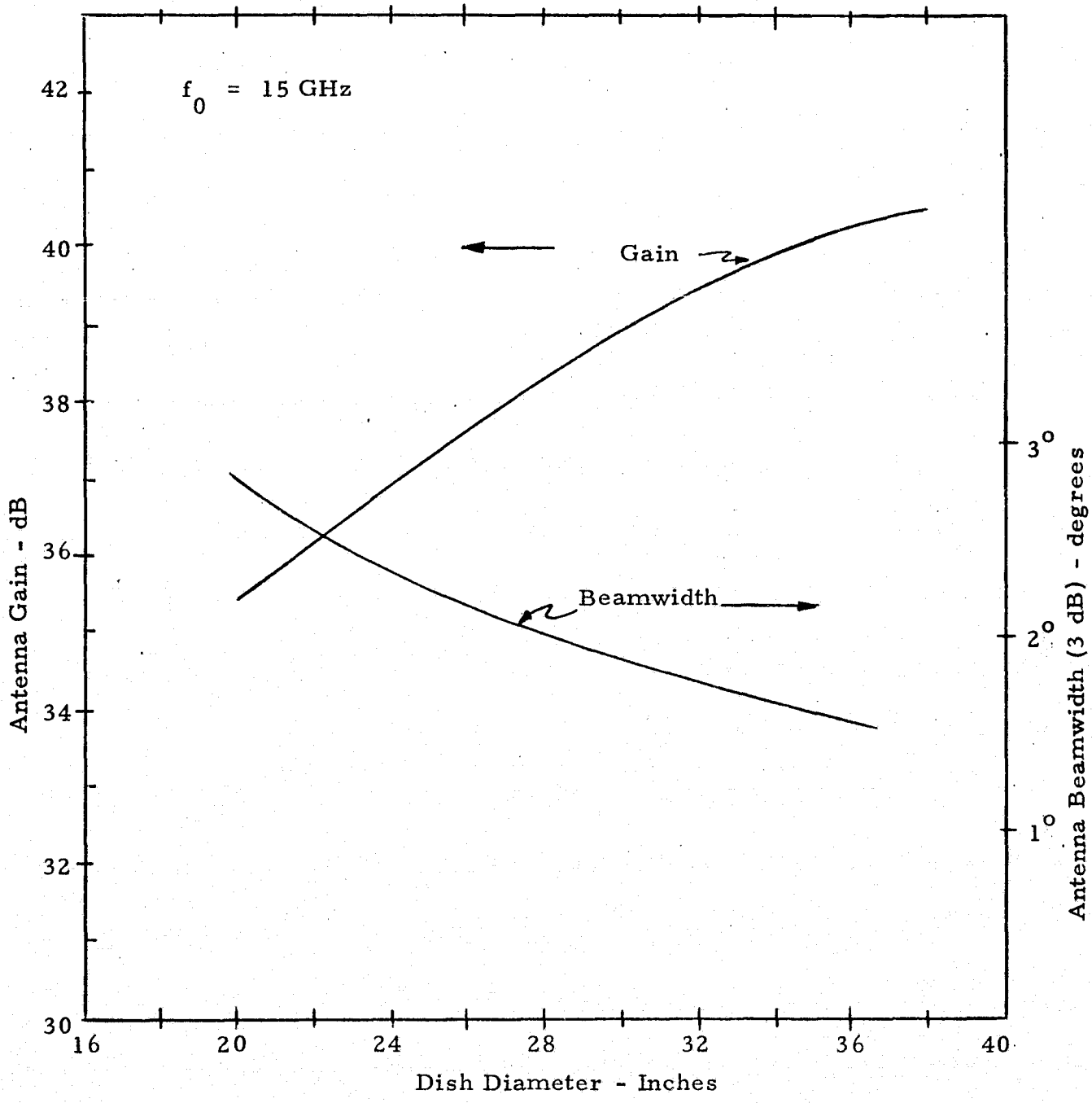


Figure 1. Antenna Beamwidth (3 dB) and Gain vs. Diameter  
of a Parabolic Dish for  $f_0 = 15 \text{ GHz}$

$2 \text{ Hz} \leq f_s < 10 \text{ Hz}$						
Frame Time, $T_s$						
	30 sec			60 sec		
$\theta_m$ , deg	$30^\circ$	$20^\circ$	$10^\circ$	$30^\circ$	$20^\circ$	$10^\circ$
Antenna Dish Diameter	$t_d$ - msec			$t_d$ - msec		
20 in.	63.1	150	707	127	302	1,417
26 in.	34.9	82.8	372	71.3	167	748
32 in.	22.6	53.7	239	46.5	109	479
36 in.	17.3	40.3	183	36.1	84.1	367

Table 1. Minimum Dwell Time vs. Dish Diameter, Frame Time and Maximum Scan Angle for Scan Frequency  $f_s$  Range of 2-10 Hz

### 3.0 THE RANGE EQUATION

The range equation for the pulse doppler radar in the detection mode is given in Table 2. The objective is to solve the detection equation for the peak transmitted power,  $P_p$ , in terms of the scan-dependent parameters such as  $\bar{R}_p$ ,  $\tau_t$ , and  $L_i$ . The pertinent parameters which determine the quantitative solution of the detection equation are given in Table 3.

The result is summarized in the form:

$$P_p (\text{dBw}) = \bar{R}_p (\text{dB}) + L_{st} (\text{dB}) + L_i (\text{dB}) - 2G(\text{dB}) - \tau_t (\text{dB}) + 50.5^* \text{ dB} . \quad (1)$$

The scan dependence of  $\bar{R}_p$  is due to use of either two 30-second frames or of a single 60-second frame. Swerling II target is assumed because of 6-step frequency diversity gain. Probability of detection is 0.90 per scan for two-frame scan, and 0.99 for the single frame scan, thus resulting in total probability of detection  $P_D = 0.99$ , regardless of the number of scan frames used.

It must be pointed out that  $\tau_t$  in the range equation is the dwell time per frequency which also takes into account the nonoptimal position of the target within the beamwidth of the scanning antenna. The relationship between  $\tau_t$  and  $t_d$  is

$$\tau_t = \frac{\tilde{t}_d}{N} = \frac{t_d K}{N}$$

where

$$\begin{aligned} \tau_t &= \text{minimum dwell time per frequency} \\ N &= \text{number of frequencies used} \end{aligned} \quad \left. \begin{array}{l} \\ \end{array} \right\} \text{Frequency diversity parameters}$$

$$K = \sqrt{\Delta(2-\Delta)} = 0.714 \text{ for } \Delta = 0.3$$

$$\tilde{t}_d = \text{average dwell time per scan} .$$

---

\* This constant is for the 22.2 km (12 nmi) detection range. The corresponding constant for the 14.8 km (8 nmi) detection range is 43.5 dB.

Table 2. Range Equation for Passive Mode Detection,  
Pulse Doppler Radar

$$\bar{R}_p = \frac{2\bar{A}^2}{N_0} = \frac{G^2 \bar{\sigma} \lambda^2 2 d_t^2 P_p \tau_t}{(4\pi)^3 R^4 K T_s d_r L}$$

where

$\bar{R}_p$  = SNR required for given  $P_D$  and  $P_{fa}$

$\bar{\sigma}$  = average target cross section ( $1 \text{ m}^2$ )

$\lambda$  = radar wavelength (0.02 m)

$d_t$  = transmit duty cycle (0.625)

$P_p$  = peak transmit power

$\tau_t$  = dwell time per frequency (worst case)

R = range

K = Boltzman constant =  $1.38 \times 10^{-23}$

T = system noise temperature

L = total losses (polarization losses not included)

$d_r$  = received duty cycle (0.375)

**Table 3. Quantitative Solution of Range Equation for Passive Mode Detection, Pulse Doppler Radar**

<u>Term</u>	<u>Value</u>	<u>dB (+)</u>	<u>dB (-)</u>
$\text{SNR}_{\text{req}}$		$\bar{R}_p$	
$G^2$	$f(A)$		2 G (dB)
$\lambda$	0.02 m	34	
$\bar{\sigma}$	1 m <sup>2</sup>		0
Dwell Time	$f(A, \theta_m, T_s)$		$\tau_t$ (dB)
$(4\pi)^3$	2000	33	
Range	22.2 km (12 nmi)	173.8	
K	$1.38 \times 10^{-23}$ joules/ $^\circ\text{K}$		228.6
$T_s$ (NF = 7 dB)	1165 $^\circ\text{K}$	30.7	
Total System Losses*		$L_{st}$ (dB)	
Lateral Scan Loss		1.2	
Scan Alignment Loss		2.1	
Average Eclipsing Loss	$(d_t = 0.625)$	7.5	
Center Line Loss		1.1	
Receiver Duty Factor	$(d_r = 0.375)$		4.3
Doppler Filter Mismatch		1.0	
Integration Loss	$f(A, \theta_m, T_s)$	$L_i$ (dB)	
	$\bar{R}_p + 283.4 + L_{st}$ (dB) + $L_i$ (dB)	- 232.9 - 2G (dB) - $\tau_t$ (dB)	

$$P_p (\text{dBw}) = \bar{R}_p (\text{dB}) + L_{st} (\text{dB}) + L_i (\text{dB}) - 2G (\text{dB}) - \tau_t (\text{dB}) + 50.5 \text{ dB}$$

\* Exclusive of losses shown in this table. Thus,  $L_{st}$  includes such losses as RF, threshold, etc.

The integration loss  $L_i$  can be estimated by considering the total doppler filter bandwidth  $B'$  required to pass the single line of the frequency hopped spectrum. Because of frequency hopping and unknown velocity, the doppler lines will be spread across the band  $\Delta f$  which is determined by the frequency hop range, the carrier frequency and the range of possible closing and opening velocities. The bandwidth required to pass only the spectrum of the frequency dwell pulse is approximately  $1/\tau_t$ . Thus, the total bandwidth of the doppler filter must be at least the sum of  $\Delta f$  and  $1/\tau_t$ . The effective number of pulses integrated,  $n_i$ , can then be written as

$$\begin{aligned} n_i &= B' \tau_t N = \left( \Delta f + \frac{1}{\tau_t} \right) \tau_t \times N = (\Delta f \tau_t + 1) N \\ &= \left( \frac{\Delta f t_d K}{N} \right) N + N = \Delta f t_d K + N \quad (3) \end{aligned}$$

where  $\Delta f = |\Delta f_{cl}| + |\Delta f_{op}|$ .

From (3), it is evident that  $n_i$  depends on the dwell time  $t_d$  which, in turn, is the function of the antenna beamwidth and scan frame time.

#### 4.0 PEAK POWER CALCULATIONS

To demonstrate how the peak requirements are calculated for various combinations of antenna sizes and numbers of scan (one or two), we will carry out one sample calculation step by step and then we will present the results for all others in a form of graph sets.

The specific case selected for the sample calculation is as follows:

Antenna dish diameter: 20 inches

Two-Way Antenna Gain, 2G: 70.8 dB (G = 35.4 dB)

Number of Scans: 1 and 2

Frequency Hop Range: 250 MHz

Number of Frequencies  
(Diversity): 6

Scan Angle Limit:  $\pm 30^\circ$

Detection Range: 22.2 km (12 nmi)

We begin by looking up the corresponding values of  $t_d$  in Table 1. Thus, for  $f_s \geq 2$  Hz, the  $\tau_t$  and the corresponding probability of detection  $P_D$  are

$$\text{One Scan: } \tau_t(1) = \frac{t_d(1)}{N} = \frac{(0.127)(0.714)}{6} = 0.015 \text{ sec or } 15 \text{ msec}$$

$$P_D = 0.99$$

$$\text{Two Scans: } \tau_t(2) = \frac{t_d(2)}{N} = \frac{(0.0631)(0.714)}{6} = 0.0075 \text{ sec or } 7.5 \text{ msec}$$

$$P_D = 0.90 \quad (4)$$

The corresponding values of average dwell times  $\tilde{t}_d(1)$  and  $\tilde{t}_d(2)$  are 91 msec and 45.1 msec, respectively.

The false alarm number,  $n'$ , is about  $2 \times 10^6$  for either case. This number is consistent with the average false alarm time of 3600 seconds. The analysis supporting this value of  $n'$  stems from the consideration of the number of filters required to cover nonambiguously the frequency uncertainties associated with the closing and opening velocities of the passive target during the acquisition. For the nominal operating frequency of 15 GHz, these uncertainties are:

	<u>Velocity</u>	<u>Doppler Shift</u>
Closing	45 m/sec	4,500 Hz
Opening	23 m/sec	2,300 Hz
$6,800 \text{ Hz} = \text{total } \Delta F$		

The bandwidths required to accommodate the dwell time at each of the six frequencies during each antenna pass are:

$$\text{One Scan: } B(1) = \frac{1}{\tau_t(1)} = \frac{1}{0.015} \approx 67 \text{ Hz}$$

$$\text{Two Scans: } B(2) = \frac{1}{\tau_t(2)} = \frac{1}{0.0075} \approx 133 \text{ Hz.} \quad (5)$$

To accommodate the additional uncertainties caused by the frequency hopping perturbation of the doppler shifts, the bandwidth of each doppler filter has to be increased by

$$\pm \Delta f = \frac{2(\pm V)}{C} (\Delta f_c) \quad (6)$$

where

$\Delta f$  = frequency shift

$V$  = velocity

$\Delta f_c$  = frequency diversity range

$C$  = velocity of light .

For  $\Delta f_c = 250$  MHz, we have

$$\Delta f_{cl} = \frac{(2)(45)(2.5)10^8}{3 \times 10^8} = +75 \text{ Hz}$$

and

$$\Delta f_{op} = \frac{(2)(-23)(2.5)10^8}{3 \times 10^8} = -38 \text{ Hz} . \quad (7)$$

Thus, based on the increased bandwidth,  $B'$ , of each doppler filter, we can proceed to calculate the number of filters required for the one and two scan cases:

$$\begin{aligned} \text{One Scan: } B'(1) &= B(1) + |\Delta f_{cl}| + |\Delta f_{op}| \\ &= 67 + 75 + 38 = 180 \text{ Hz} \end{aligned} \quad (8)$$

$$n_f(1) = \frac{\Delta F}{B'(1)} = \frac{6800 \text{ Hz}}{180 \text{ Hz}} = 38 \text{ filters} \quad (9)$$

$$\begin{aligned} \text{Two Scans: } B'(2) &= B(2) + |\Delta f_{cl}| + |\Delta f_{op}| \\ &= 133 + 75 + 38 = 246 \text{ Hz} \end{aligned} \quad (10)$$

$$n_f(2) = \frac{\Delta F}{B'(2)} = \frac{6800 \text{ Hz}}{246 \text{ Hz}} = 28 \text{ filters} . \quad (11)$$

The probability of false alarm,  $P_{fa}$ , is

$$P_{fa} = \frac{n_i}{t_{fa} \Delta F} \quad (12)$$

where

$n_i$  = effective number of pulses integrated

$t_{fa}$  = false alarm time (3600 sec)

$\Delta F$  = total bandwidth of doppler filter bank.

In our case,

$$n_i = B' t N = B' \tilde{t}_d \quad (13)$$

where  $N$  = number of frequency hops ( $N = 6$ ).

Substituting (12) into (11), we get

$$P_{fa} = \frac{B \tilde{t}_d}{t_{fa} \Delta F} = \frac{\tilde{t}_d}{t_{fa} n_f} \quad (14)$$

Thus, the false alarm number (F.A.N.) is

$$F.A.N. = n' = \frac{1}{P_{fa}} = \frac{t_{fa} n_f}{\tilde{t}_d} \quad (15)$$

To compute  $n'$  for one and two scan cases, let  $t_{fa} = 3600$  sec and substitute appropriate numbers for  $n_f$  and  $\tilde{t}_d$ :

$$\text{One Scan: } n'(1) = F.A.N. = \frac{(3600)(38)}{(91)(10^{-3})} \approx 1.5 \times 10^6 \quad (16)$$

$$(P_{fa} = \frac{1}{n'(1)} \approx 7 \times 10^{-7})$$

$$\text{Two Scans: } n'(2) = F.A.N. = \frac{(3600)(28)}{(45.1)(10^{-3})} \approx 2.2 \times 10^6 \quad (17)$$

$$(P_{fa} = \frac{1}{n'(2)} \approx 4.5 \times 10^{-7})$$

The effective number of pulses integrated  $n_i^*$  and the corresponding integration loss  $L_i(n)$  is:

$$\text{One Scan: } n_i = B'(1) \tilde{t}_d = (180)(0.091) = 16 \quad (18)$$

$$L_i(16) = 2.2 \text{ dB}$$

$$\text{Two Scans: } n_i = B'(2) \tilde{t}_d = (246)(0.045) = 11 \quad (19)$$

$$L_i(11) = 2.4 \text{ dB}.$$

Having established the required  $P_D$  and  $n^*$  values, we tabulate the scan-dependent parameters required to solve for the peak transmitted power. The required data is summarized in Table 4.

Substituting data of Table 4 into equation (1), we get for  $L_{st} = 0$ :

One 60-second scan frame:

$$\begin{aligned} P_p(\text{dBw}) &= \bar{R}_p(\text{dB}) + L_i(\text{dB}) - 2G(\text{dB}) - \tau_t(\text{dB}) + 50.5 \text{ dB} \\ &= 14.5 + 2.2 - 70.8 - (-18.2) + 50.5 \\ &= 14.6 \text{ dBw or } \underline{28.8 \text{ watts (peak)}}. \end{aligned} \quad (20)$$

$$P_{ave} = P_p \frac{d}{t} = (28.8)(0.625) = \underline{18 \text{ watts (ave)}}$$

Two 30-second scan frames:

$$\begin{aligned} P_p(\text{dBw}) &= 11.6 + 2.4 - 70.8 - (-21.2) + 50.5 \\ &= 14.9 \text{ dBw or } \underline{30.9 \text{ watts (peak)}} \end{aligned} \quad (21)$$

$$P_{ave} = P_p \frac{d}{t} = (30.9)(0.625) = \underline{19.3 \text{ watts (ave)}}$$

Note that the results provided by (20) and (21) are for  $L_{st} = 0$ . In a real system,  $L_{st}$  will obviously not be zero and thus the required peak power will increase accordingly. Figures 2 and 3 show the peak powers required as a function of  $L_{st}$  for various combinations of  $\theta_m$ ,  $T_s$ , dish size, and detection range. Note that the sample calculation presented above (see uppermost curves of Figure 3) represents the worst case, i.e.,  $\theta_m = \pm 30^\circ$

---

\* D. K. Barton, Radar System Analysis, Prentice-Hall, 1964.

Table 4. Scan-Dependent Parameters for Sample Calculation

	Number of frequencies: N = 6 Scan angle: $\pm 30^\circ$	
Number of Frames	1	2
Required $P_D$ /Frame	0.99	0.90
F.A.N.	$\approx 2 \times 10^6$	$\approx 2 \times 10^6$
Target Type	Swerling II	Swerling II
$\bar{R}_p$	14.5 dB	11.6 dB
Diversity Gain	13.5 dB (see Note)	6.7 dB
$\tau_t$	15.0 msec	7.14 msec
$\tau_t$ (dB)	-18.2 dB	-21.2 dB
$L_i$ (dB)	2.2 dB	2.4 dB

Note: This value of diversity gain exceeds 10 dB allowed maximum.

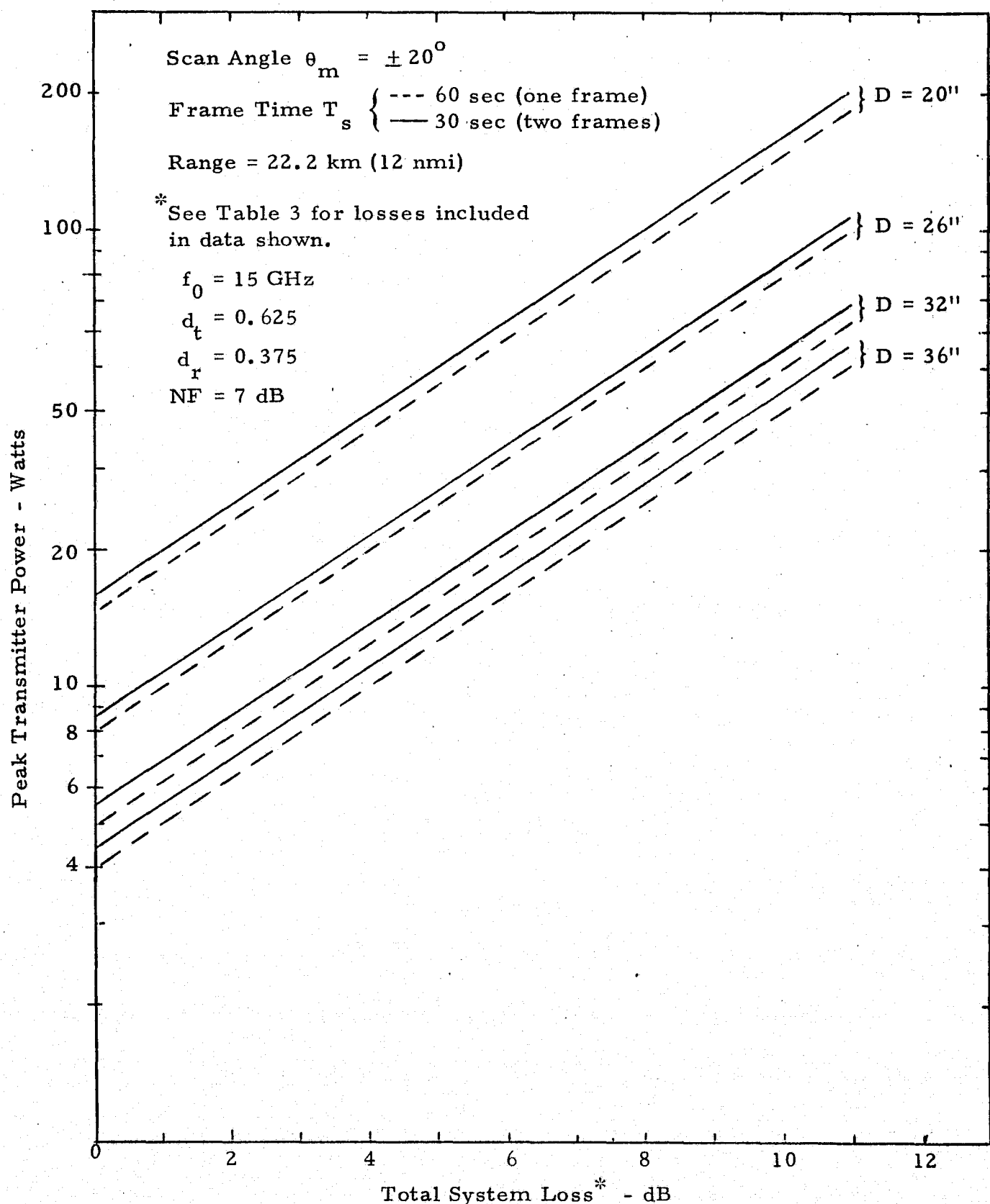


Figure 2. Peak Transmitter Power vs. Total System Loss\* and Antenna Dish Diameter for Passive Target Detection (Pulse Doppler System)

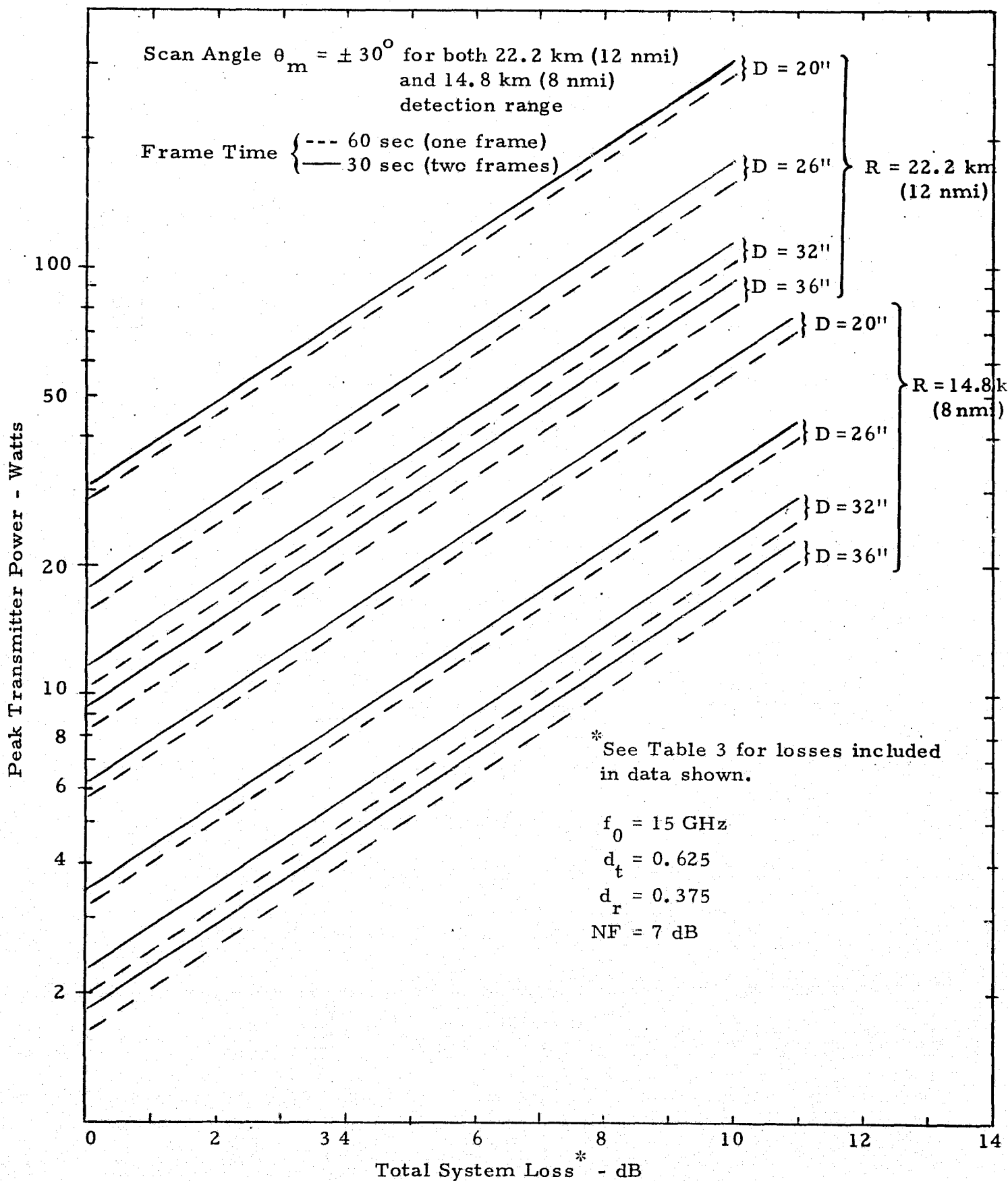


Figure 3. Peak Transmitter Power vs. Total System Loss\* and Antenna Dish Diameter for Passive Target Detection (Pulse Doppler Radar)

and detection range of 22.2 km (12 nmi). All other pertinent data used for obtaining plots of Figures 2 and 3 are summarized in Tables 5 and 6.

## 5.0 CONCLUSIONS

From the data presented in Figure 2, it is evident that, for  $\theta_m = \pm 20^\circ$  passive target detection at 22.2 km (12 nmi) can be performed with a 50-watt peak power transmitter if the total system losses are kept below about 7.5 dB and a minimum dish diameter is 26 inches. Larger dish sizes permit a better tradeoff between the losses and the power margin. With a 20-inch antenna the losses must be kept below 5 dB to provide detection with a 50-watt peak power transmitter.

For  $\theta_m = \pm 30^\circ$ , data in Figure 3 shows that for 50-watt peak power limitation, detection at 22.2 km can be performed only with a 36-inch antenna if the system losses are as high as 7.5 dB. On the other hand, detection at 14.8 km (8 nmi) permits use of smaller size dishes and provides greater loss and margin value tradeoffs for a 50-watt peak power limitation.

D(in)/2G(dB)	20 in/70.8 dB		26 in/75.4 dB		32 in/79.0 dB		36 in/81.0 dB	
T <sub>s</sub> (sec)	30	60	30	60	30	60	30	60
t <sub>d</sub> (sec)	0.150	0.302	0.0828	0.167	0.0537	0.1089	0.0403	0.0841
$\tilde{t}_d$ (sec)	0.107	0.216	0.0591	0.119	0.0383	0.0778	0.0288	0.060
n <sub>i</sub>	18	30	12	19	10	15	9	13
$\tau_t$ (sec)	0.0179	0.036	0.0099	0.0199	0.0064	0.0130	0.0048	0.010
B (Hz)	56	28	101	50	156	77	208	100
B' (Hz)	170	141	215	163	270	190	322	213
n <sub>f</sub>	41	48	32	42	26	36	21	32
F.A.N. ( $\times 10^6$ )	1.35	0.8	1.93	1.26	2.4	1.66	2.6	1.91
P <sub>fa</sub> ( $\times 10^{-7}$ )	7.4	12	5.2	8	4.2	6.0	3.8	5.2
L <sub>i</sub> (dB)	3.2	3.0	2.6	2.4	2.3	2.0	2.1	1.9
$\tau_t$ (dB)	-17.5	-14.4	-20.0	-17.0	-21.9	-18.9	-23.2	-20.0

Table 5. Passive Target Detection Parameters vs. Dish Diameter (D) for  $\theta_m = \pm 20^\circ$

D(in)/2G (dB)	20 in/70.8 dB		26 in/75.4 dB		32 in/79.0 dB		36 in/81.0 dB	
T <sub>s</sub> (sec)	30	60	30	60	30	60	30	60
t <sub>d</sub> (sec)	0.063	0.127	0.0349	0.0713	0.0226	0.0465	0.0173	0.0361
$\tilde{t}_d$ (sec)	0.045	0.091	0.0249	0.051	0.0161	0.0332	0.0124	0.0258
n <sub>i</sub>	11	16	9	12	8	10	7	9
$\tau_t$ (sec)	0.0075	0.015	0.0042	0.0085	0.0027	0.0055	0.0021	0.0043
B (Hz)	133	67	240	118	372	180	486	233
B' (Hz)	246	180	354	231	485	294	600	346
n <sub>f</sub>	28	38	20	30	14	24	12	20
F.A.N. ( $\times 10^6$ )	2.2	1.5	2.8	2.1	3.1	2.5	3.3	2.7
P <sub>fa</sub> ( $\times 10^{-7}$ )	4.5	6.6	3.6	4.8	3.2	4	3.0	3.6
L <sub>i</sub> (dB)	2.4	2.2	2.0	1.7	1.9	1.5	1.8	1.4
$\tau_t$ (dB)	-21.2	-18.2	-23.8	-20.7	-25.7	-22.6	-26.8	-23.7

Table 6. Passive Target Detection Parameters vs. Dish Diameter (D) for  $\theta_m = \pm 30^\circ$

## APPENDIX O

## SIGNAL DESIGN FOR PULSE DOPPLER RADAR SYSTEM

Sergei Udalov

## 1.0 INTRODUCTION

For the pulse doppler radar system to be compatible with the 50-watt CW communication transmitter, the radar signal design must be such that the operation in all radar modes is compatible with the peak power limitation of the transmitter. This means that the average power of the radar signal can be up to 50 watts but that its peak power should not exceed this value.

The analysis of the signal design for the cooperative mode\* indicates that this peak power constraint can be met when the pulse doppler radar interrogator works with a compatible transponder. Consequently, in this appendix, we will concentrate primarily on the signal design for the passive mode radar operation.

The operation in the passive mode can be logically subdivided into the four following modes applicable to the ranges shown:

- |                           |   |
|---------------------------|---|
| (1) Detection:            | $20.4 \text{ km (11 nmi)} \leq R \leq 22.2 \text{ km (12 nmi)}$ |
| (2) Acquisition:          | $18.5 \text{ km (10 nmi)} \leq R \leq 20.4 \text{ km}$          |
| (3) Tracking:             | $2 \text{ km} \leq R \leq 18.5 \text{ km}$                      |
| (4) Short Range Tracking: | $30 \text{ m} \leq R \leq 2 \text{ km}$                         |

(Note: The range division between modes 3 and 4 is arbitrary. Also, 22.2 km detection range requirement is worst case.)

The candidate signal design formats for these modes are described below, and the corresponding range and velocity measurement accuracies are estimated.

---

\* See Appendix E, Final Report (Phase I), "Study to Investigate and Evaluate Means of Optimizing the Radar Function," Axiomatix Report No. R7511-3, under NASA Contract NAS 9-14614, November 1975.

## 2.0 SIGNAL DESIGN CONSIDERATIONS

### 2.1 Generalized Range Equation

We can estimate the radar performance in the various modes by starting with a generalized radar equation and then considering the effect of the parameter changes associated with the modulation formats for the different modes. Table 1 shows the generalized radar equation. The terms which are associated with the mode changes are isolated by the brackets, and their effect is considered separately in Table 2. Also note that the form of the generalized radar equation is for the peak signal  $S_p$  versus unit bandwidth noise  $N_0$ . Using the values of Table 1, we compute the mode-independent value of  $S_p/N_0$  at the acquisition range of 20.4 km. This value of  $D(R)$  combined with results of Table 2 is then used for estimating system performance in the various modes.

Note that in Table 1 we have computed the value of  $D(R)$  based on the assumption of 5 dB system loss. This value is the maximum allowable to perform passive target detection at 22.2 km (12 nmi) with the 20 in. diameter dish and a two-frame (30 sec/frame) search within the scan angle limit  $\theta_m = \pm 20^\circ$  (see Figure 2, Appendix N, of this report).

The assumption of a 20 in. diameter antenna is consistent with baseline design considerations, although the ultimate use of larger dishes is not ruled out and is, in fact, desirable from the standpoint of providing better performance margins.

The value of  $R = 20.4$  km (11 nmi) is used in Table 1 because it is assumed that at this range the signal search and detection phase is already completed and the system is ready to go through the velocity and range acquisition phases.

### 2.2 Center Line Detection Mode Signal Design

The center line detection mode is initiated at the estimated target range of 22.2 km (12 nmi). This mode therefore precedes the velocity and range acquisition modes. The power budgets for the detection mode are

Table 1. Generalized Radar Equation - Pulse Doppler Radar

$$\frac{S_p}{N_0} = \underbrace{\frac{P_p G^2 \lambda^2 \bar{\sigma}}{(4\pi)^3 k T_s L_f} \times \frac{1}{R^4}}_{D(R)} \times \underbrace{\left( \frac{d_t^2}{d_r L_m} \right)}_{\text{Mode Dependent}}$$

where  $S_p/N_0$  = peak signal-to-unit noise bandwidth ratio, dB-Hz

$P_p$  = peak transmitted power

$G$  = antenna gain

$\lambda$  = wavelength (0.02 m)

$\bar{\sigma}$  = average target cross section ( $1 \text{ m}^2$ )

$k$  = Boltzman constant =  $1.38 \times 10^{-23}$  joules/ $^\circ\text{K}$

$R$  = radar range

$d_t$  = transmit duty cycle

$d_r$  = receive duty cycle

$L_{st}$  = system losses, i.e., transmit and receive RF, etc.  
(polarization loss not included)

$L_m$  = mode-dependent losses

$D(R)$  = value of  $S/N_0$  at range  $R$  exclusive of mode-dependent term

Compute  $D(R)$  at acquisition range of 20.4 km (11 nmi):

Term	Value	dB(+)	dB(-)
$P_p$	50 watts	17 dBw	
$G^2$ (20" dish)		70.8	
$\lambda^2$	$\lambda = 0.02 \text{ m}$		34
$\bar{\sigma}$	$1 \text{ m}^2$	0	
$(4\pi)^3$	2000		30
$R$	20.4 km (11 nmi)		172.4
$k$	$1.38 \times 10^{-23}$ joules/ $^\circ\text{K}$	228.6	
$T$ (NF = 7 dB)	1165 $^\circ\text{K}$		30.7
$L_{st}$ , system losses (see text)		5	
		+316.4 dB-Hz	-272.1 dB
$D(20.4 \text{ km})$	= 316.4 dB-Hz - 272.1 dB	= 44.3 dB-Hz	

Table 2. Mode Dependent Terms for Acquisition and Tracking ( $2 \text{ km} \leq R \leq 20.4 \text{ km}$ )

Mode/Terms	Center Line Detection (Search mode $d_t = 0.625$ )		Center Line Acquisition and Tracking $d_t = 0.625$		Center Line Tracking $(d_t \geq 0.1)$		Range Acquisition and Track $(d_t \geq 0.1)$	
	dB (+)	dB (-)	dB (+)	dB (-)	dB (+)	dB (-)	dB (+)	dB (-)
Scan Alignment Loss		2.1						
Lateral Scan Loss		1.2						
Transmitter Duty Factor ( $d_t^2$ )		4.1		4.1		22.8		
Receiver Duty Factor ( $d_r$ )	4.3		4.3		11.1		11.1	
Average Eclipsing Loss		7.5		7.5		0.5		0.5
Doppler Filter Loss		1.0						
Totals	+4.3 dB	-15.9 dB	+4.3 dB	-11.6 dB	+11.1 dB	-22.8 dB	+11.1 dB	-0.5 dB
Net Gain/Loss		-11.6 dB		-7.3 dB		-11.7 dB		+10.6 dB

discussed in detail in Appendix N. Thus, below we will discuss primarily the signal structure for this mode.

Assume that, in the detection mode, the two-frame search is used, i.e., the antenna beam scans twice over the  $\pm 20^\circ$  cone and each frame takes 30 seconds. The frequency is hopped over six positions and thus the dwell time per frequency  $\tau_t = 17.9$  msec (see Table 5 of Appendix N).

Because the transmit duty cycle is 0.625, the radar's PRF must be cycled over several values during each frequency dwell so as to minimize the eclipsing loss. The minimum value of any one of the PRFs must be high enough to provide nonambiguous velocity readout. Since the expected passive target velocity of 45 m/sec corresponds to 4.5 kHz doppler shift at 15 GHz, the minimum PRF for nonambiguous velocity estimation is 9 kpps. The 9 kpps PRF, however, corresponds to nonambiguous range of 17 km, which is less than the 22.2 km detection range.

Consequently, we must consider the use of several PRFs which are considerably higher than the 9 kpps value. Also, because in the acquisition mode we want to determine the range nonambiguously, we will select a set of PRFs which will permit us to obtain the range information by applying the Chinese remainder theorem. The application of this theorem has been already explained in Appendix E of the Final Report for Phase I of this study. Thus, we will modify the previously used values to comply with the passive target acquisition.

The expression for the "basic range time,"  $\tau$ , can be obtained from  $T_{\max}$  (time determined by maximum nonambiguous range) by the following expression:

$$\tau = \frac{T_{\max}}{\prod_{k=1}^K n_k} \quad (1)$$

where  $k$  = number of PRFs and  $n_k$  = set of relatively prime numbers, such as  $N, N+1, N+2, \dots$ . Practical considerations, such as hardware complexity

and acquisition time limitations, dictate that the largest value of  $n_k$  should not exceed the values from about 8 to 50. After considering various tradeoffs for our specific case, we have tentatively selected four PRFs based on the following set of relatively prime numbers:

$$N = 9$$

$$N + 1 = 10$$

$$N + 2 = 11$$

$$N + 4 = 13 .$$

Also, for reasons which will be explained later, we selected  $T_m = 45 \text{ msec}$ , despite the fact that this value corresponds to a nonambiguous range far exceeding the ranges under consideration. Based on the aforementioned values, the basic range time  $\tau$  is:

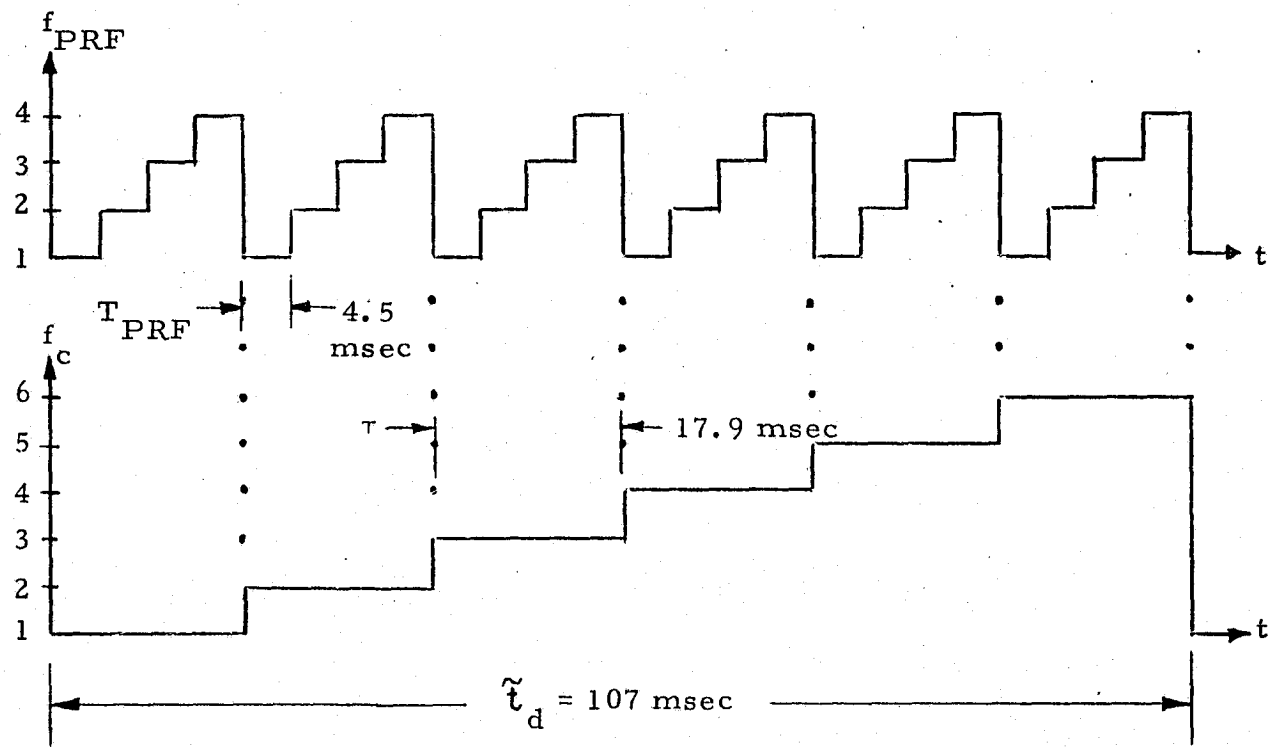
$$\begin{aligned} \tau &= \frac{T_{\max}}{N(N+1)(N+2)(N+4)} = \frac{45 \times 10^{-3} \text{ sec}}{(9)(10)(11)(13)} = 3.5 \times 10^{-6} \text{ sec} \\ &\quad = 3.5 \mu\text{sec} . \end{aligned} \quad (2)$$

The four PRFs and their corresponding interpulse periods are then:

$$\begin{aligned} f_1 &= \frac{1}{(9)(3.5)10^{-6}} = 31.8 \text{ kpps} & T_1 &= \frac{1}{f_1} = 31.5 \mu\text{sec} \\ f_2 &= \frac{1}{(10)(3.5)10^{-6}} = 28.6 \text{ kpps} & T_2 &= \frac{1}{f_2} = 35.0 \mu\text{sec} \\ f_3 &= \frac{1}{(11)(3.5)10^{-6}} = 26.0 \text{ kpps} & T_3 &= \frac{1}{f_3} = 38.5 \mu\text{sec} \\ f_4 &= \frac{1}{(13)(3.5)10^{-6}} = 22.0 \text{ kpps} & T_4 &= \frac{1}{f_4} = 45.5 \mu\text{sec} \end{aligned} \quad (3)$$

Note that all PRFs shown in (3) are sufficiently high to permit nonambiguous velocity determination for the passive target case.

The corresponding frequency hop and PRF change frames are shown in Figure 1. Note that dwell time per frequency,  $\tau_t$ , and the corresponding



Note: Numerical values shown are for 20" diameter dish,  $\theta_m = \pm 20^\circ$ , and the two 30-second frame scans. For other parameters, the durations of the dwells vary accordingly.

Figure 1. Time Schedule of RF Carrier Frequencies and PRFs.

time per PRF,  $T_{\text{prf}}$ , are based on the assumption of average dwell time  $\bar{t}_d$  which is less than nominal dwell time,  $t_d$ , across the center of the beam. For the case of a 20-inch dish,  $\theta_m = \pm 20^\circ$  and two 30-second scans,  $t_d = 150 \text{ msec}$  and  $\bar{t}_d = 107 \text{ msec}$ . The corresponding value for  $T_{\text{prf}}$  is then approximately 4.5 msec.

It must be pointed out that, although four PRFs are used during each RF frequency dwell time, the RF phase is the same throughout the  $\tau_t$  interval. Because of the coherence over the entire RF frequency dwell, the spectra of the consecutive PRF frames reinforce each other in the center line.\* Therefore, the one-sided spectral width of the center line is the reciprocal of the RF frequency dwell time  $\tau_t$ . For  $\tau_t = 17.9 \text{ msec}$ , the bandwidth is approximately 56 Hz. All other noncentral lines do not add over the RF dwell time because of the varying PRF. This, however, is of no consequence to the operation of the center line detection scheme considered here.

Having established the signal format for the center line detection mode, let us examine the changes in this format required to accommodate other modes of radar operation.

### 2.3 Center Line Acquisition and Track Initiation Mode

After the detection of the center line in one of the doppler filters, antenna scan is terminated, the antenna is pointed at the target, and the angle track is initiated. With the antenna pointed at the target, the scan alignment and the lateral scan losses are eliminated. Also, a 200 Hz bandwidth frequency tracker is positioned at the frequency of the detected line and the doppler tracking is initiated. Note that the transmit duty cycle is still 0.625 (receive  $d_r = 0.375$ ) and we have not acquired the range information. The worst case signal-to-noise ratio in the frequency tracker in this mode is:

---

\* C. L. Weber, "Analysis of a Center Line Pulsed Doppler Radar Operating in the Search Mode," Axiomatix Report No. R7407-1 (under Contract NAS 9-13467), July 1974.

$$\begin{aligned}
 (S/N)_{B_{dt}} &= D(20.4 \text{ km}) - 7.3 \text{ dB} \text{ (from Table 2)} - 10 \log(200 \text{ Hz}) \\
 &= 44.3 \text{ dB} - 7.3 \text{ dB} - 23 \text{ dB} = +14.3 \text{ dB} .
 \end{aligned} \tag{4}$$

At this point, we may perform a frequency measurement and thus "memorize" the velocity value for the range acquisition mode which follows.

Note that, although the signal format has not changed, positioning the antenna on the target removes the scan losses, thus providing better center line SNR for frequency tracking. Also, positioning the frequency tracker on the center line removes the doppler filter loss.

#### 2.4 Range Acquisition Mode Signal Structure

For the range acquisition, we reduce the transmit duty cycle to about 0.1 which is commensurate with a pulse width of 3.5 microseconds\* and the 22.0 to 31.8 kpps PRF cycling. The range estimate is then made by checking the SNR in 25 overlapping range bins. Since the information fed into each bin is gated at the same duty cycle as the transmitter ( $d_r = d_t$ ), we do not accumulate excessive noise in each range bin. The SNR in each gate is then:

$$\begin{aligned}
 (S/N)_{RG} &= D(20.4 \text{ km}) + 10.6 \text{ dB} \text{ (from Table 2)} - 10 \log(1/\tau) \\
 &= 44.3 + 10.6 - 10 \log(2.86 \times 10^5 \text{ Hz}) \\
 &= 54.9 \text{ dB} - 54.6 \text{ dB} = +0.3 \text{ dB} .
 \end{aligned} \tag{5}$$

With this SNR and Swerling II target, about 125 pulses have to be integrated\*\* in each gate to provide  $P_D = 0.99$  at  $P_{fa} \approx 10^{-10}$ . The corresponding false alarm time,  $t_{fa}$ , is

$$\begin{aligned}
 t_{fa} &= \frac{N}{n P_{fa}} = \frac{(125)(3.5)10^{-6}}{(25)10^{-10}} = 17.5 \times 10^4 \text{ seconds} \\
 &= 48.6 \text{ hours}
 \end{aligned} \tag{6}$$

\* The pulse width is now equal to the basic range time and thus the solution of the range algorithm can be carried out. This is the reason for selection of  $T_m = 45 \text{ msec}$ .

\*\* DiFranco and Rubin, Radar Detection, Prentice-Hall, 1968, pp. 400-401.

where  $N$  = number of pulsed integrated per gate  
 $\tau$  = pulse width (also range gate width)  
 $n_g$  = number of gates  
 $P_{fa}$  = false alarm rate .

To insure reliable range detection, the system will be cycled at least once through the entire frequency diversity cycle which, in our case, is about 100 msec long. Assuming that the solution of the range algorithm will take another 100 msec, the total time to detect and acquire range will take about 0.2 seconds. This time is an order of magnitude less than the averaging time of the velocity integrator (2 seconds) and consequently the relatively short interruption of the doppler input during range acquisition should not present a problem.

## 2.5 Simultaneous Center Line (Velocity) and Range Tracking Mode

Once the range is acquired and range track is initiated, the doppler frequency tracker and the velocity integrator are supplied from the range gated signal with an average duty cycle of about 0.1. The signal-to-noise ratio in the 200 Hz frequency tracker loop is then

$$\begin{aligned} \frac{(S/N)_B}{dt} &= D(20.4 \text{ km}) - 11.7 \text{ dB} \text{ (from Table 2)} - 10 \log (200 \text{ Hz}) \\ &= 44.3 \text{ dB} - 11.7 \text{ dB} - 23 \text{ dB} = +9.6 \text{ dB} . \end{aligned} \quad (7)$$

Although (7) indicates a reduction in the SNR available for frequency tracking, as compared with high duty cycle ( $d_t = 0.625$ ) mode, the absolute value is still more than adequate to maintain accurate velocity tracking simultaneously with the range tracking. Note that, with this proposed scheme, both the velocity and range tracking are performed simultaneously by their respective circuits and continuous mode switching is not required.

## 2.6 Short Range Mode ( $30 \text{ m} \leq R \leq 2 \text{ km}$ ) Signal Structure

At a range of about 2 km, the target return strength will increase by about 40 dB compared to that at the acquisition range of 20.4 km, i.e.,

$D(2 \text{ km})$  is about 84.3 dB. Furthermore, at this range, even the highest PRF of 31.8 kpps will provide nonambiguous range tracking. The system can therefore be switched into the "short range" mode. In this mode, the pulse width will be reduced to 0.1 microsecond to permit range tracking down to 30 meters. The PRF will be fixed at 31.8 kpps. Table 3 shows the mode-dependent terms for the short range mode.

The SNR for velocity tracking in the short range mode is

$$\begin{aligned} \frac{(S/N)}{B_{dt}} &= D(2 \text{ km}) - 25 \text{ dB} (\text{from Table 3}) - 10 \log (200 \text{ Hz}) \\ &= 84.3 \text{ dB} - 25 \text{ dB} - 23 \text{ dB} = +36.3 \text{ dB}. \end{aligned} \quad (8)$$

Also, the SNR for the range tracking in this mode is

$$\begin{aligned} \frac{(S/N)}{RG} &= D(2 \text{ km}) + 25 \text{ dB} (\text{from Table 3}) - 10 \log (1/\tau_s) \\ &= 84.3 \text{ dB} + 25 \text{ dB} - 10 \log (10^7 \text{ Hz}) \\ &= 109.3 \text{ dB} - 70 \text{ dB} = +39.3 \text{ dB}. \end{aligned} \quad (9)$$

Thus, adequate SNR is available for both the velocity and range tracking in the short range mode.

## 2.7 Estimated Accuracies

### 2.7.1 Range Tracking Accuracy

The primary random component will be determined by the thermal noise. At the acquisition range of 20.4 km, the SNR is about +0.3 dB or a ratio of 1.07. Assuming range tracker noise bandwidth ( $\beta_{nr}$ ) of 10 Hz and lowest PRF ( $f_r$ ) of 22.0 kpps, we can estimate rms time error ( $\sigma_t$ ) for a 3.5 microsecond pulse width ( $\tau$ ) as

$$\sigma_t = \frac{\tau}{\sqrt{(S/N) f_r / \beta_{nr}}} = \frac{3.5 \mu\text{sec}}{\sqrt{(1.07) \frac{22.0 \times 10^4}{10}}} = \frac{3.5 \mu\text{sec}}{(1.035)(47)} = 0.07 \mu\text{sec} \quad (10)$$

**Table 3.** Mode Dependent Terms for Short Range Mode  
 $(\tau = 0.1 \mu\text{sec}, \text{PRF} = 31.8 \text{ kpps})$

Mode/Term	Center Line Tracking		Range Tracking	
	dB(+)	dB(-)	dB(+)	dB(-)
Transmitter Duty Factor ( $d_t^2$ )		50		NA
Receiver Duty Factor ( $d_r$ )	25		25	
Average Eclipsing Loss		0		0
	+25 dB	-50 dB	+25 dB	0
Net Gain/Loss		-25 dB		+25 dB

and thus

$$\sigma_{rn} = 150 \text{ m}/\mu\text{sec} \times 0.07 \mu\text{sec} = \underline{10.5 \text{ meters}}. \quad (11)$$

The slowly varying component will be determined primarily by the time delay variation in the IF filter of the receiver. Assuming a 4-pole Butterworth filter of 400 kHz-3 dB bandwidth, the envelope delay to 50% rise time is 1.5 microsecond.\* Also, if we assume that only 10% of this delay is random and it is uniformly distributed, we obtain for the RMS range error:

$$\sigma_{rd} = \frac{(1.15 \mu\text{sec})(150 \text{ m}/\mu\text{sec})(0.1)}{\sqrt{12}} = \underline{5 \text{ meters}}. \quad (12)$$

The exact nature of this error is difficult to determine, but it cannot be neglected, particularly when operating at short ranges. Consequently, the switch to a shorter pulse width at short range not only improves the random error but also permits the reduction of bias errors because of wider filters.

Specifically, in the short range mode ( $\tau_s = 0.1 \mu\text{sec}$ , PRF = 31.8 kpps), at 2 km, the  $\sigma_r$  due to thermal noise will be:

$$\begin{aligned} \sigma_{rn}' &= \frac{\tau(\mu\text{sec})}{\sqrt{(S/N) f_r / \beta_{nr}}} (150 \mu\text{sec}/\text{m}) = \frac{(0.1)(150)}{\sqrt{(89 \times 10^3) \frac{31.8 \times 10^3}{10}}} \\ &= \frac{15}{(94.4)(56)} = \underline{0.0028 \text{ meters}}. \end{aligned} \quad (13)$$

This value is too small to be of significance. For example, if the range counter clock frequency is 20 MHz and range is measured to the nearest cycle, then  $\Delta r = 7.5 \text{ meters}$ . For uniform distribution,  $\sigma_{rc}$  is

$$\sigma_{rc} = \frac{7.5 \text{ m}}{\sqrt{12} \sqrt{f_r / \beta_{nr}}} = \frac{7.5 \text{ m}}{(3.46) \sqrt{\frac{31.8 \times 10^3}{10}}} = \underline{0.04 \text{ meter}}. \quad (14)$$

\* K. W. Henderson and W. H. Kantz, "Transient Response of Conventional Filters," IRE Trans. on Circuit Theory, December 1958, pp. 333-347.

This points to the fact that internal system errors, range clock primarily, are the limiting factor for random noise at short ranges.

The envelope delay error for short range mode, when normalized for a 4-pole Butterworth filter of 13.4 MHz, is about 0.14 meter ( $1\sigma$ ). All of the major errors listed above are, however, within the specifications.

### 2.7.2 Velocity Tracking Accuracy

The accuracy of the velocity readout will be dependent not only on the available SNR and the integration time, but also on the spectrum smearing due to frequency hopping. If we were to consider the effect of SNR alone on the measurement of a non-hopped spectrum, we could use the following expression:<sup>\*</sup>

$$\sigma_F = \left[ \frac{0.078 B (1 + 1/SNR)^2}{T (1 + SNR)^{1/2}} \right]^{1/2} \quad (15)$$

where  $B$  = tracking filter bandwidth

$T$  = averaging time

SNR = signal-to-noise ratio in  $B$ .

Using frequency acquisition SNR of 14.3 dB,  $B = 200$  Hz, and  $T = 2$  seconds, the rms frequency error of the tracker is 1.26 Hz, which corresponds to an equivalent rms velocity error of 0.0126 m/sec. This value is well within the required specification accuracy and thus we assume that thermal noise is not a limitation in this case.

Now if we consider the effect of frequency agility on the  $\sigma_{FA}$ , we have to use the expression:

$$\sigma_{FA} = \sqrt{\frac{B_i}{2T}} \quad (16)$$

---

<sup>\*</sup> "Optimizing the Rendezvous Radar Function for the Space Shuttle,"  
D C Monthly Report #4, September 1975.

where  $B_i$  = frequency uncertainty due to frequency hopping and  $T$  = averaging time. In our case, for  $\Delta F = 250$  MHz,  $B_i = 113$  Hz. Therefore, for  $T = 2$  sec, we have

$$\sigma_{FA} = \sqrt{\frac{113}{(2)(2)}} = 5.3 \text{ Hz} \quad (17)$$

or the velocity error of 0.053 m/sec.

Although the latter value is still within specification, it becomes obvious that the error due to frequency hopping predominates. Therefore, we will consider the latter value as the one which determines the velocity readout accuracy.

Another source of velocity readout error may be the instrumentation used to measure the doppler shift frequency. For example, if the conventional, i.e., direct-frequency-counting, method is used, the accuracy of this method is always limited to a  $\pm 1$  cycle of the input signal.\* This implies that accuracy becomes poorer as the measured frequency is lowered. But, let us consider what significance this limitation presents for our case.

The velocity readout specification calls for  $3\sigma_v$  accuracy of 0.3 m/sec with readout delay of no more than 2 seconds. Thus,  $\sigma_v = 0.1$  m/sec. At  $f_c = 15$  GHz, the equivalent value of the rms frequency error  $\sigma_F$  is

$$\sigma_F = \frac{(2)(\sigma_v)f_c}{c} = \frac{(2)(0.1)(1.5)10^{10}}{(3)10^8} = 10 \text{ Hz} \quad (18)$$

Suppose now that a frequency counter having a gate width of 2 seconds is used. In other words, the gate width is equal to the delay readout. For a completely noiseless case, the lowest frequency which can be measured within this interval is then 0.5 Hz. The reading, however, can be 0, 0.5, or 1 Hz depending on the timing accuracy and phasing of the gate. The

---

\* Ian T. Band, "Automatic Counter Inverts Period to Get Frequency," Hewlett-Packard Journal, May 1969, pp. 17-20.

error is then  $\pm 0.5$  Hz which is far below the  $\sigma_F = 10$  Hz value. If the gate length remains at 2 seconds, frequencies lower than 0.5 Hz cannot be measured and, thus, a zero velocity readout should be displayed. For frequencies above 1 Hz, the error is  $\pm 1$  Hz which is still only 10% of  $\sigma_F$  value, thus corresponding to  $\sigma_v = 0.01$  m/sec. Consequently, we will assume that  $\sigma_F = 1$  Hz, and correspondingly,  $\sigma_v = 0.01$  m/sec, can be classified as bias errors. Note, however, that the random velocity error due to frequency hopping is at least 5 times as large as the instrumentation error. In other words, as stated earlier, it appears that the frequency hopping error will predominate over other errors. Its magnitude, however, is within the required specification.

## APPENDIX P

## GROUND RETURN ANALYSIS

Sergei Udalov

## 1.0 INTRODUCTION

The possibility of the ground return interfering with the Shuttle rendezvous radar operation arises when the passive target is in a position such that the radar antenna points towards the earth at an angle close to vertical. Such a possibility may occur if the Shuttle misses the rendezvous with the target and thus it has to maneuver back into a position where the radar antenna can be pointed at the target for reacquisition. The minimum altitude for such an occurrence may be 185.3 km (100 nmi orbit) but the range to the target may be anywhere from 1 km (or less) to 20 km.

The analysis presented below takes into consideration the transient response of the ground as the function of the radar pulse width and of the antenna beamwidth. It is shown that, at near vertical incidence and target range of 2 km, the pulse width of 0.1 microsecond or less can provide target-to-clutter power ratios of 7 to 9 dB for antenna beamwidth ranging from  $1.4^{\circ}$  to  $2.8^{\circ}$  and ground reflectivity equal to unity. If the range to the target increases, the ratio decreases at the rate of 12 dB per octave. This ratio also decreases with longer pulse widths, higher ground reflectivity, and wider antenna beamwidth. Consequently, the use of clutter suppression techniques is recommended.

Specifically, the frequency hopping technique appears to be most applicable to pulse doppler radars whose high PRF(s) and high duty cycle do not permit direct range discrimination available to low PRF, low duty cycle radars. The only requirement is that the radar system be capable of rapid ( $f_h \geq 800$  hops/sec) frequency diversity. The material which follows deals with the analysis of the ground return. Included also is a brief description of the frequency hopping method for ground clutter suppression.

## 2.0 GENERAL CONSIDERATIONS

The general nature of the ground return can be understood by considering the simplified case of vertical incidence illustrated in Figure 1. From this figure, it is evident that, as the leading edge of an RF signal hits the ground, progressively larger areas are illuminated and, thus, theoretically, the total return increases as the time progresses. For most cases of practical interest, this is not the case, however. The main factors contributing to the "diminishing return" are: (1) the average reflectivity  $\sigma_n$  generally decreases with the incidence angle  $\theta_n$  and (2) the antenna beam shape attenuates returns at  $\theta_n \geq \theta_B$ , where  $\theta_B$  is the nominal antenna beamwidth. Thus, in most cases, the return from the ground, as measured by a relatively narrow pulse,\* will be like the hypothetical return shown in Figure 2. Such a return can be considered as the "impulse function" for a particular system geometry. To obtain the shape of the return for any other pulse waveform, one must perform the convolution of the transmitted waveform with the impulse function return. The impulse return can be obtained by considering individual contributions of the return from each incremental area  $A_n$ . Table 1 provides an expression for  $\Delta A$  and gives definitions for various terms involved.

As can be seen from Table 1, the evaluation of the total return from an extended surface is rather complex and, therefore, wherever applicable, various simplifications should be used. One such simplification is that, for a relatively narrow beam (i.e.,  $\theta_B \leq 3^\circ$ ),  $\sigma_0$  may be assumed to be nearly constant over the illuminated area. Another simplifying assumption is that within the antenna beamwidth the differences between the ranges to the individual reflectors, i.e.,  $d(\theta)$ , are insignificant compared to the total height,  $h$ , above the ground. Thus, we can write a simplified equation for the total power,  $P_c$ , reflected from the ground:

---

\* A pulse whose duration is short compared to the time required for the wavefront to spread to the 3 dB beamwidth of the antenna.

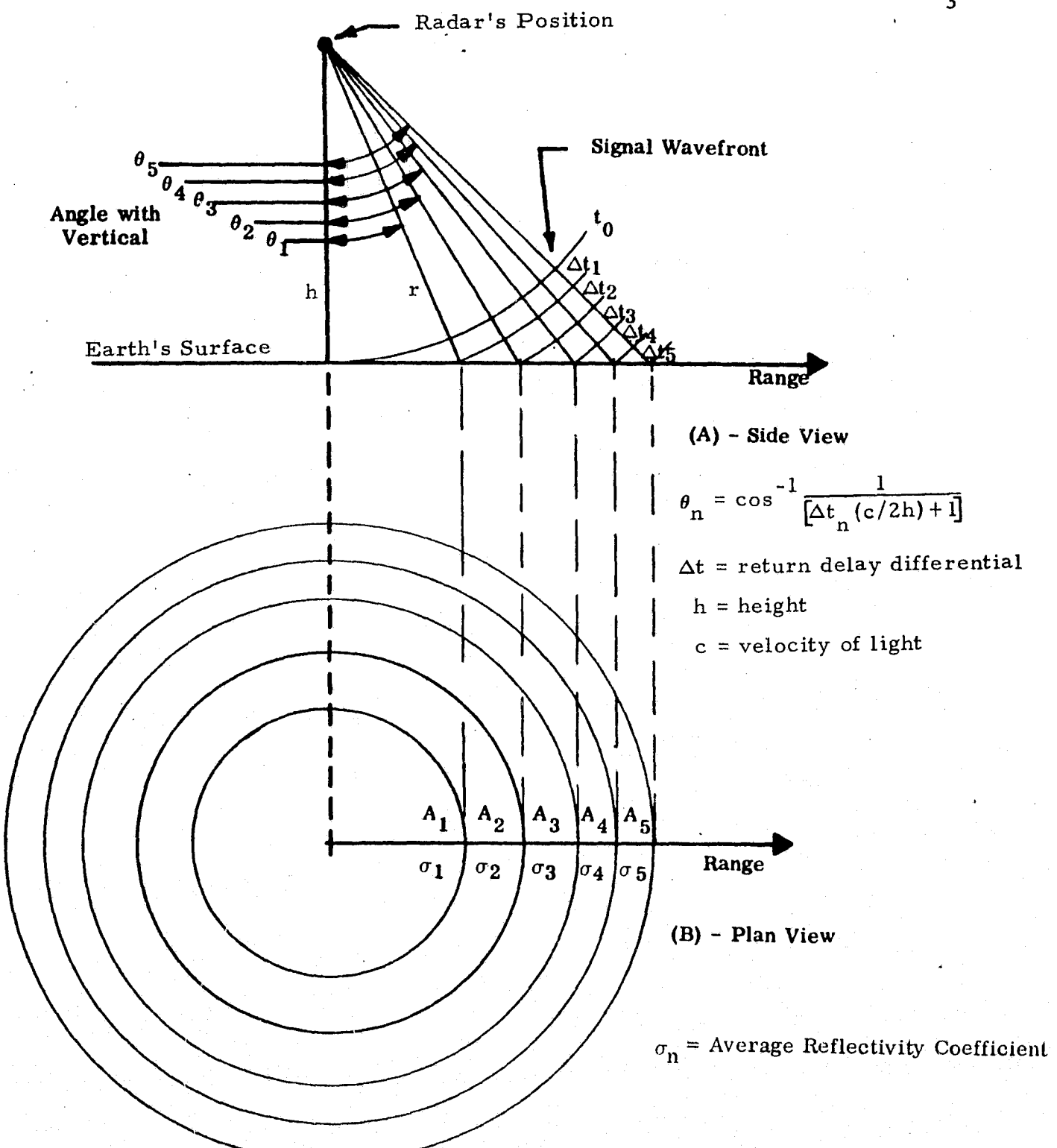


Figure 1. Time-Area Diagram for Transient Analysis of Ground Return

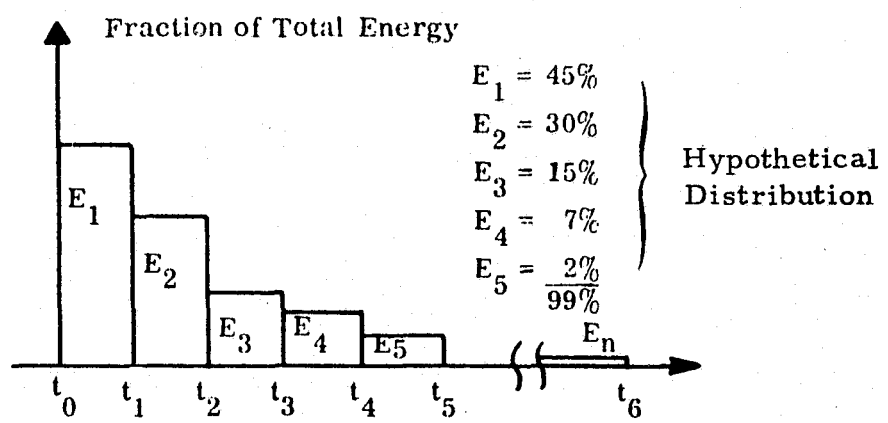


Figure 2. Hypothetical Distribution of Energy Return  
From an Extended Surface (Impulse Response)

Table 1. General Expression for Power Return from an Incremental Area of an Extended Surface

$$\Delta P_{\text{rec}} = \frac{P_t G^2(\theta) \lambda^2}{(4\pi)^3 d^4(\theta)} \sigma_0(\theta, \rho, \lambda', \beta) \Delta A(\theta)$$

where  $\Delta P_{\text{rec}}$  = power received from an incremental surface area  $\Delta A(\theta)$

$P_t$  = transmitted power

$G(\theta)$  = antenna gain in the direction of the unit area

$\lambda$  = operating wavelength

$d(\theta)$  = distance between radar antenna and incremental area  $A(\theta)$

$\rho$  = surface roughness

$\lambda'$  = wavelength-dependent losses

$\sigma_0(\theta, \rho, \lambda', \beta)$  = average radar cross section per unit area

$\Delta A(\theta)$  = incremental area

$$P_c \approx \frac{P_t G^2 \lambda^2}{4\pi^3 h^4} \sigma_0(\alpha) A(\theta, h)$$

where  $P_t$  = transmitted power

$G$  = antenna gain

$\lambda$  = wavelength

$h$  = radar height above ground

$\sigma_0(\alpha)$  = surface reflectivity (function of incidence angle  $\alpha$ )

$A(\theta, h)$  = illuminated area.

Note that the illuminated area is a function of height as well as  $\theta$ , which can be any angle within the main lobe of the antenna beamwidth. Thus, when calculating  $P_c$  at any particular height  $h$ , the value and characteristics of  $\theta$  must be clearly defined. In the following sections, we analyze the time-varying behavior of  $\theta$  and from it we derive the expressions for the transient response of the ground return at near vertical incidence.

### 3.0 TRANSIENT RESPONSE OF THE NEAR VERTICAL GROUND RETURN

The analysis presented below takes into account the effect of the time dependence, as well as the radar pulse width dependence, of the ground return. It is also shown that the antenna beamwidth is a major factor which influences the target-to-clutter power ratio.

We begin by referring to Figure 3, which shows the relationship between the quasi-stationary and the time-variable parameters which determine the transient behavior of the near vertical ground return. Specifically, we assume that the altitude  $h$  varies slowly compared to other time-dependent parameters, and thus is quasi-stationary. We also assume that the average reflectivity  $\sigma_0$  is uniform within the limits defined by the antenna beamwidths under consideration and that the illuminated ground patch is level.

Thus, as the RF wavefront hits the ground at nadir point a, the boundary of the reflecting area begins to spread and, at some time  $t$  after nadir contact, it spreads to a circle containing point b. Also, as shown in the figure, the boundary of the illuminated area is defined by the time-varying angle  $\theta(t)$ . From the geometry shown, we have

$$\cos \theta(t) = \frac{h}{h + \Delta r(t)} \quad (1)$$

where

$$\Delta r(t) = \frac{2t}{c}, \quad (2)$$

since we are considering only the monostatic radar return.

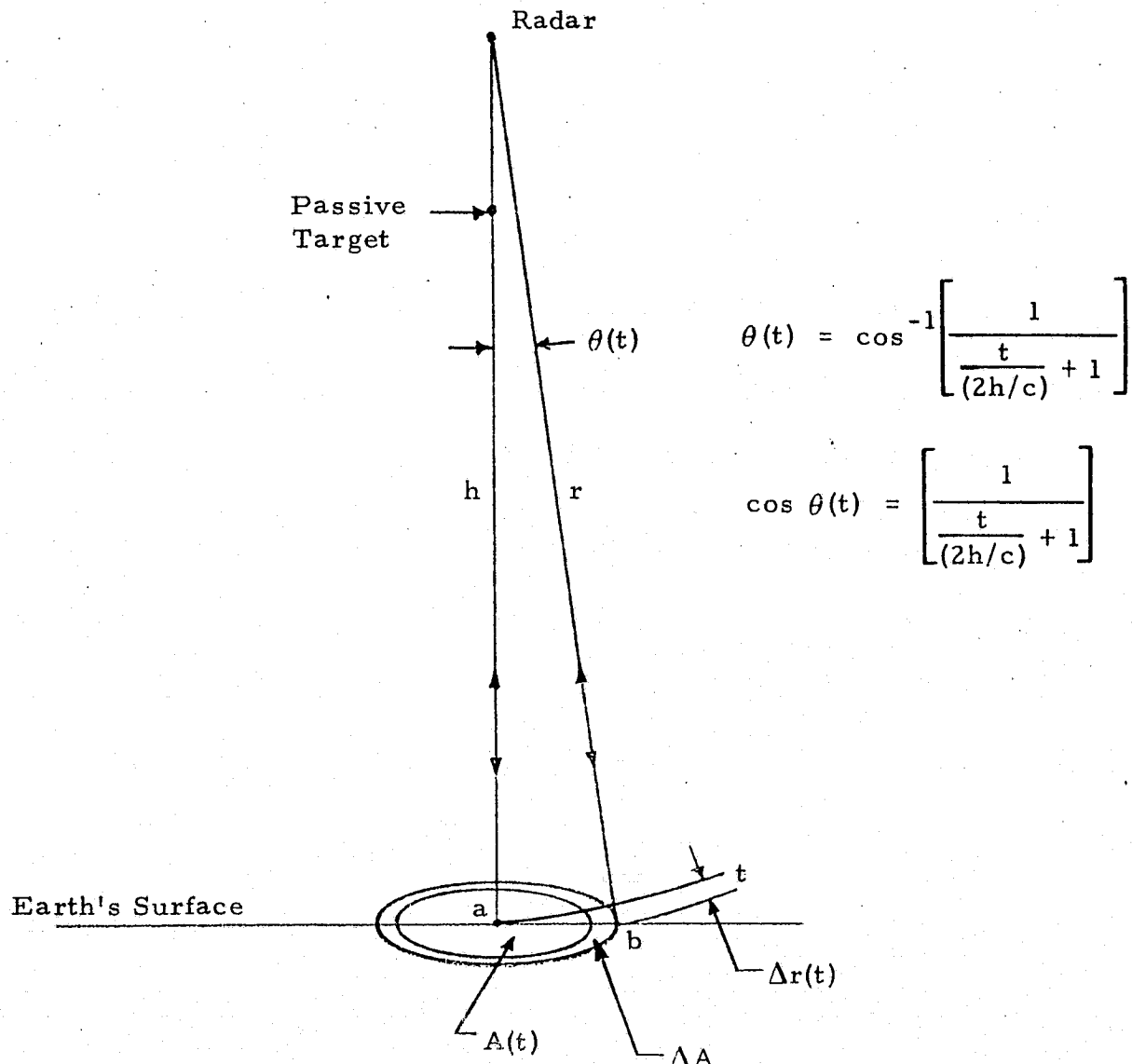


Figure 3. Near Vertical Return Geometry

Substituting (2) into (1), we have

$$\cos \theta(t) = \frac{1}{1 + \frac{t}{(2h/c)}} = \frac{1}{1 + \frac{t}{T}} \quad (3)$$

where we define

$$T = \frac{2h}{c} = \text{nadir return delay}. \quad (4)$$

Note that, for the case of  $h = 185.3 \text{ km}$  (100 nmi),  $T$  is

$$T = \frac{(2)(185.3 \times 10^3 \text{ m})}{300 \text{ m}/\mu\text{sec}} = 1235.3 \mu\text{sec}. \quad (5)$$

Now, since we are considering cases where  $t \ll T$  and  $\theta \ll 1$  radian, we can expand both sides of (3) into their respective series. Thus, (3) becomes

$$1 - \frac{\theta^2(t)}{2!} + \frac{\theta^4(t)}{4!} - \dots = 1 - \frac{t}{T} + \frac{2}{2!} \left(\frac{t}{T}\right)^2 - \dots \quad (6)$$

Retaining only the first lowest order terms of both sides, we have

$$\theta^2(t) \approx 2 \frac{t}{T}. \quad (7)$$

Equation (7) establishes a relatively simple relationship between  $\theta(t)$  and  $t$ , i.e., the time after start of radar return.

Now we will derive the expression for the time-varying area of the ground return. From Figure 1, it is evident that

$$\begin{aligned} A(t) &= \pi h^2 \tan^2 \theta(t) \\ &\approx \pi h^2 \theta^2(t) \text{ for } \theta(t) \ll 1 \text{ radian}. \end{aligned} \quad (8)$$

Substituting (7) into (8), we obtain the expression for  $A(t)$  explicitly as the function of  $t$ :

$$A(t) = \frac{2\pi h^2}{T} t. \quad (9)$$

Equation (9) shows that the illuminated area varies directly as a function of  $t$ , provided that we do not consider the effect of the antenna directivity pattern  $G(\theta)$ . For a Gaussian beam shape approximation, the two-way normalized directivity (gain) pattern is given by

$$G^2(\theta) = \exp(-5.552 \theta^2/\theta_B^2) \quad (10)$$

where  $\theta_B$  is one way 3 dB beamwidth and  $\theta$  is the direction of signal arrival w/r to beam center. But, from (7) we know that  $\theta$  is a time-varying function  $\theta(t)$ . Thus, we can rewrite (10) as a time-varying weighing function:

$$w[\theta(t)] = \exp[-5.552 \theta^2(t)/\theta_B^2]. \quad (11)$$

The weighing factor expressed by (11) can be applied only to the differential areas defined by an expanding ring having a time "thickness"  $\Delta t$ . In other words, (11) can be applied only to the "impulse response" of the ground. To obtain the expression for such a response, we use (9). Thus, the differential increase in area  $\Delta A$  due to time increase  $\Delta t$  is computed by subtracting  $A(t)$  from  $A(t + \Delta t)$ :

$$\Delta A = A(t + \Delta t) - A(t) = \frac{2\pi h^2}{T} (t + \Delta t - t) = \frac{2\pi h^2}{T} \Delta t. \quad (12)$$

The magnitude of the impulse response is obtained by dividing  $\Delta A$  by  $\Delta t$  and letting  $\Delta t \rightarrow 0$ . Consequently,

$$\delta_G(t) = \lim_{\Delta t \rightarrow 0} \frac{\Delta A}{\Delta t} = \lim_{\Delta t \rightarrow 0} \frac{A(t + \Delta t) - A(t)}{\Delta t} = \frac{2\pi h^2}{T}. \quad (13)$$

Because this is a definition of the derivative, we thus obtain:

$$\delta_G(t) = \frac{dA}{dt} = \frac{2\pi h^2}{T} \quad (14)$$

for the unweighted impulse response of the ground. Note that within the assumptions used, i.e.,  $\theta(t) \ll 1$  radian and  $\theta_B \ll 1$  radian, this

response is constant, which is a characteristic of a perfect integrator. This is also evident from (9), which tells us that the reflecting area increases linearly with time. Since such a ramp-like response is obtained from an integrator when a unit step function is applied to its input, we could have obtained (14) by direct differentiation of (9).

Now, we can proceed and apply the antenna pattern weighting function (11) to the unweighted impulse response (14):

$$\delta'_G(t) = \frac{2\pi h^2}{T} \exp[-5.552 \theta_B^2(t)/\theta_B^2] \quad (15)$$

where the prime indicates the weighted response.

Substituting (7) into (15):

$$\begin{aligned} \delta'_G(t) &= \frac{2\pi h^2}{T} \exp[-(5.552)(2)t/T] \\ &= \frac{2\pi h^2}{T} \exp[-t/t_0(\theta_B, h)] \end{aligned} \quad (16)$$

where

$$t_0(h, \theta_B) = \frac{\theta_B^2 T}{(2)(5.552)} = \frac{\theta_B^2 (2h)}{(2)(5.552)c} = 0.180 \theta_B^2 (h/c). \quad (17)$$

Note that (16) and (17) can be used to obtain the ground return due to any envelope shape of the transmitted radar signal. For this, the envelope of the transmitted radar signal has to be convolved with (16).

But, since we are interested primarily in ground response due to rectangular pulses, we can integrate (16) to obtain the weighted ground return waveform due to a unit step. Once we know the response to the unit step, the response to a pulse of any length can be obtained by the conventional method of using positive and delayed negative step functions.

The weighted step response of the ground is the integral of (16).

Thus,

$$\begin{aligned}
 u'_G(t) &= \frac{2\pi h^2}{T} \int_0^t e^{-t'/t_0} dt' \\
 &= \frac{2\pi h^2}{T} [-t_0 e^{-t'/t_0}]_0 = \frac{2\pi h^2}{T} (-t_0 e^{-t/t_0} + t_0) \\
 &= \frac{2\pi h^2}{T} t_0 (1 - e^{-t/t_0})
 \end{aligned} \tag{18}$$

where  $T$  and  $t_0$  have been defined by (4) and (17), respectively. The physical significance of (18) can be understood better if we replace the  $t_0$  factor outside the parentheses by its definition given in (17):

$$\begin{aligned}
 u'_G(t) &= \frac{2\pi h^2}{T} \times \frac{\theta_B^2 T}{(2)(5.552)} \times (1 - e^{-t/t_0}) \\
 &= \frac{\pi h^2 \theta_B^2}{4} \times \frac{1}{1.388} \times (1 - e^{-t/t_0})
 \end{aligned} \tag{19}$$

The term  $\pi h^2 \theta_B^2 / 4$  is the area of the ground within the cone defined by the 3 dB beamwidth of the antenna. Furthermore, the factor 1.388 is the weighting factor for this area due to the Gaussian beam shape approximation.\* Therefore, we can write (19) in terms of its coefficients as

$$u'_G(t) = A(\theta_B, h) b(1 - e^{-t/t_0}) \tag{20}$$

where  $A(\theta_B, h) = \frac{\pi h^2 \theta_B^2}{4}$  = ground area, function of  $h$  and  $\theta_B$

$b$  = weighting coefficient, function of beam shape approximation used ( $b = 1/1.388$  for a Gaussian beam)

$t_0$  = system "time constant," function of  $h$  and  $\theta_B$ .

---

\* In (19), we deliberately factored the coefficient 5.552 as (4)(1.388).

Note that (20) is rather general and thus can be used along with (16) for various combinations of parameters provided that the assumptions used for expansion (6) are valid.

Let us now use (20) for calculating the ground return response to a unit step for  $h = 185.3$  km and beamwidths associated with 0.5 m and 1 m diameter antennas. Table 2 gives typical beamwidths for such antennas. Table 3 presents the computations of the corresponding time constants,  $t_0$ .

The results are shown in Figure 4. Because the ordinate is normalized to the response of the 0.5 m diameter antenna ( $\theta_B = 2.8^\circ$ ), the asymptotic value of  $A(\theta_B, h)b$  for this antenna is four times that of the 1.0 m diameter ( $\theta_B = 1.4^\circ$ ) antenna response. This, of course, is to be expected from (20) and Table 2. The main feature revealed by curves of Figure 4 is that response of the narrow beam antenna is also four times "faster" than that for the  $2.8^\circ$  beam antenna. But, again, this is to be expected from the examination of  $t_0$  values given in Table 3.

Figure 4 also shows the ground return responses of the two antennas to a 0.1  $\mu$ sec duration radar pulse. Such responses can be computed by using the following expressions:

$$f_G(t) = A(\theta_B, h) b(1 - e^{-t/t_0}) \quad 0 < t \leq \tau \quad (21)$$

$$f_G(t) = A(\theta_B, h) b(1 - e^{-\tau/t_0}) e^{-(t-\tau)/t_0} \quad t > \tau \quad (22)$$

where  $\tau$  is the radar pulse duration in time units compatible with units of  $t_0$ . In this practical case, both  $\tau$  and  $t_0$  are in microseconds.

#### 4.0 TARGET-TO-GROUND CLUTTER POWER RATIO

To compute the target-to-ground clutter power ratio,  $P_s/P_c$ , for given pulse widths and for either of the two antennas, one estimates the maximum value of  $A(\theta_B, h)b$  for these pulse widths from Figure 4.

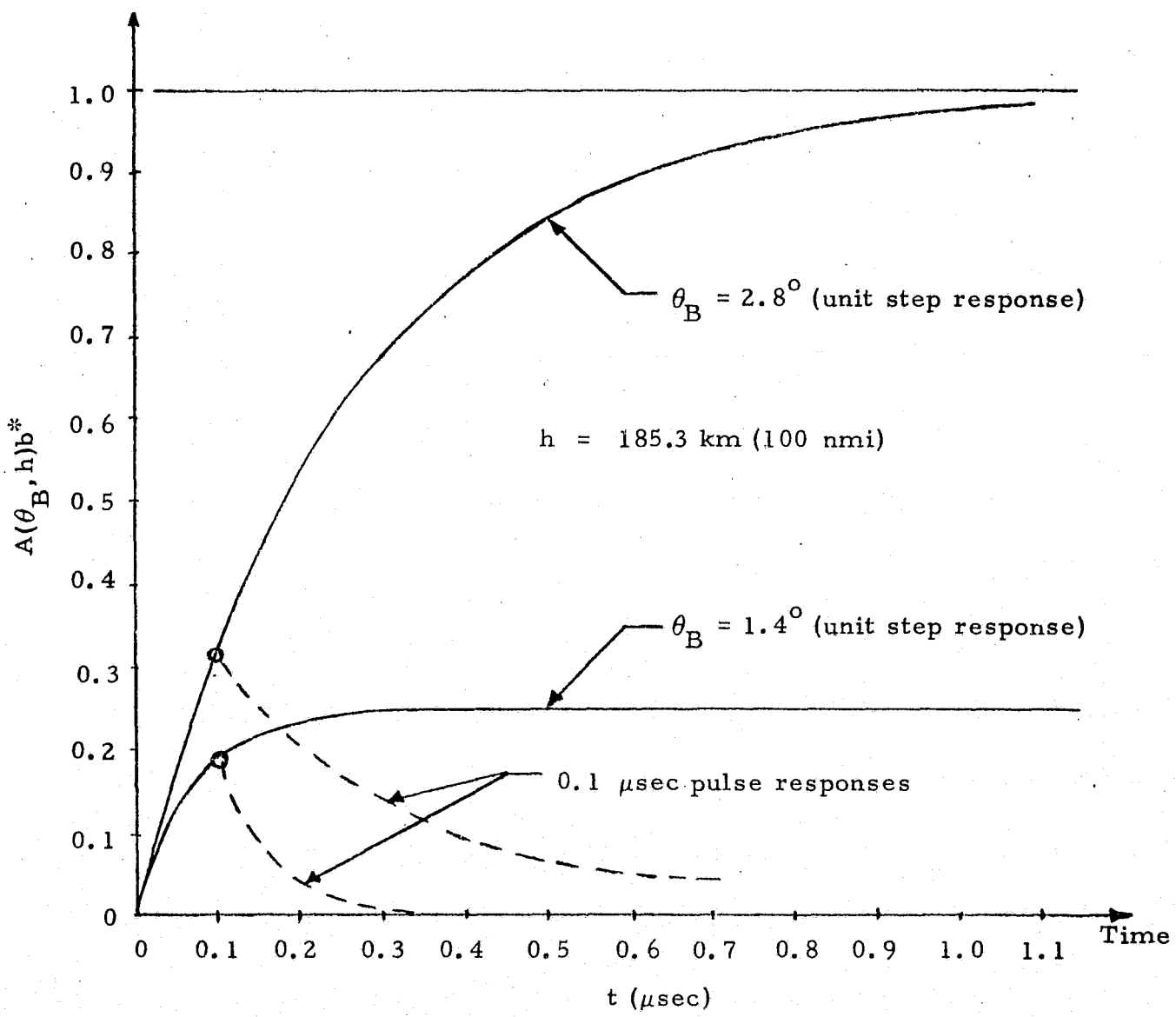
Table 2. Antenna Beamwidth vs. Dish Diameter  
(Typical Values)

Dish Diameter	$\theta_B$ (3 dB)		$\theta_B^2$ (3 dB)
	One way (deg)	One way (rad)	Two way (rad <sup>2</sup> )
0.5 m (20 in.)	2.8	0.0489	0.0024
1.0 m (40 in.)	1.4	0.00244	0.0006

Table 3. Computation of Time Constants,  $t_0(h, \theta_B)$

$$t_0(185.3 \text{ km}, \theta_B = 2.8^\circ) = \frac{\theta_B^2 (\text{rads}^2) T}{(2)(5.552)} = \frac{(0.0024)(1235.3 \mu\text{sec})}{11.104} = \underline{0.267 \mu\text{sec}}$$

$$t_0(185.3 \text{ km}, \theta_B = 1.4^\circ) = \frac{\theta_B^2 (\text{rads}^2) T}{(2)(5.552)} = \frac{(0.0006)(1235.3 \mu\text{sec})}{11.104} = \underline{0.0667 \mu\text{sec}}$$



\*Ground return normalized to 0.5 meter (20 in.) antenna response

Figure 4. Normalized Near Vertical Ground Return Response to Unit Step and to Pulses of Finite Duration

For example, for the 0.1  $\mu$ sec pulse, these values are indicated by circles on the unit step response curves.

As an example, let us compute the  $P_s/P_c$  ratio for a  $1 \text{ m}^2$  target at 2 km and  $\theta_B = 2.8^\circ$ . The altitude is assumed to be 185.3 km, i.e., 100 nmi. For this, we modify the derivation of a previous equation to accommodate the time-varying ground return. Table 4 shows the derivation and gives a numerical example.

The equation derived in Table 4 involves all the pertinent parameters needed for determining  $P_s/P_c$ . The numerical example is only for  $\tau = 0.1 \mu\text{sec}$ , however. This value of  $\tau$  was chosen as an example because, as shown below, the results obtained for the two antenna beamwidths begin to diverge beyond a 1 dB value as the pulse width increases beyond 0.1  $\mu\text{sec}$  value. The difference in favor of the narrow beamwidth antenna is due to the smaller area of the ground illuminated by this antenna.

Now, since we have shown that the  $P_s/P_c$  ratio is a function of pulse length, as well as of the antenna beamwidth, it is worthwhile to examine the relationship between  $P_s/P_c$  and  $\tau$ . Such a relationship is shown in Figure 5 for  $R = 2 \text{ km}$ ,  $h = 185.3 \text{ km}$ , and  $\sigma_0 = 1$ . From Figure 5, it is evident that, for pulses shorter than 0.1  $\mu\text{sec}$ , the difference between the  $P_s/P_c$  ratios associated with the two antenna beamwidth is not too great (less than 2 dB) and, furthermore, this difference diminishes with pulse width. The absolute values of  $P_s/P_c$  increase sharply for pulse widths less than 0.1  $\mu\text{sec}$  for both beamwidths. For pulses wider than 0.1  $\mu\text{sec}$ , the difference between the  $P_s/P_c$  ratios obtained with the two antennas approaches the asymptotic value of 6 dB which, of course, is the same as that shown in Figure 4. Thus, in general, the narrow beamwidth antenna provides better discrimination against ground clutter, a fact which is well established for all other types of clutter. However, it must be pointed out that the 1 m (40 in.) diameter dish represents about the maximum practical limit to an antenna structure which can be fitted inside the available space without introducing significant design complications.

Table 4. Target-to-Ground Clutter Power Ratio for a Boresight Target and Near Vertical Ground Return

$$\frac{P_s}{P_c}(\tau) = \frac{P_t G^2 \lambda^2 \sigma_t}{(4\pi)^3 R^4 L} \times \frac{(4\pi)^3 h^4 L}{P_t G^2 \lambda^2 A_G(\theta_B, h, \tau) b \sigma_0} = \frac{\sigma_t h^4}{R^4 A_G(\theta_B, h, \tau) b \sigma_0}$$

$$= \frac{\sigma_t h^4 (4)}{R^4 \pi h^2 \theta_B^2 b (1 - e^{-\tau/t_0}) \sigma_0} = \frac{4 \sigma_t h^2}{\pi b R^4 \theta_B^2 (1 - e^{-\tau/t_0}) \sigma_0}$$

where

$P_t$  = peak transmitted power

$G$  = bore axis antenna gain

$\lambda$  = wavelength

$R$  = target range (meters)

$h$  = altitude (meters)

$\sigma_t$  = target cross-section ( $1 \text{ m}^2$ )

$L$  = system losses

$A_G(\theta_B, h, \tau)$  = ground return area

$b$  = antenna beam shape factor ( $b = 0.72$  for Gaussian approximation)

$\theta_B$  = antenna beamwidth (in radians)

$\tau$  = pulse width

$t_0 = 0.180 \theta_B^2 (h/c)$  for Gaussian beam shape

$\sigma_0$  = ground reflectivity

$P_s$  = target power

$P_c$  = ground clutter power

Table 4 (continued)

Numerical Example

$$\text{Let } h = 1.853 \times 10^5 \text{ meters}$$

$$R = 2 \times 10^3 \text{ meters}$$

$$\tau = 0.1 \text{ microsecond}$$

$$\theta_B^2 = 0.0024 \text{ rads}^2 (2.8^\circ \text{ antenna})$$

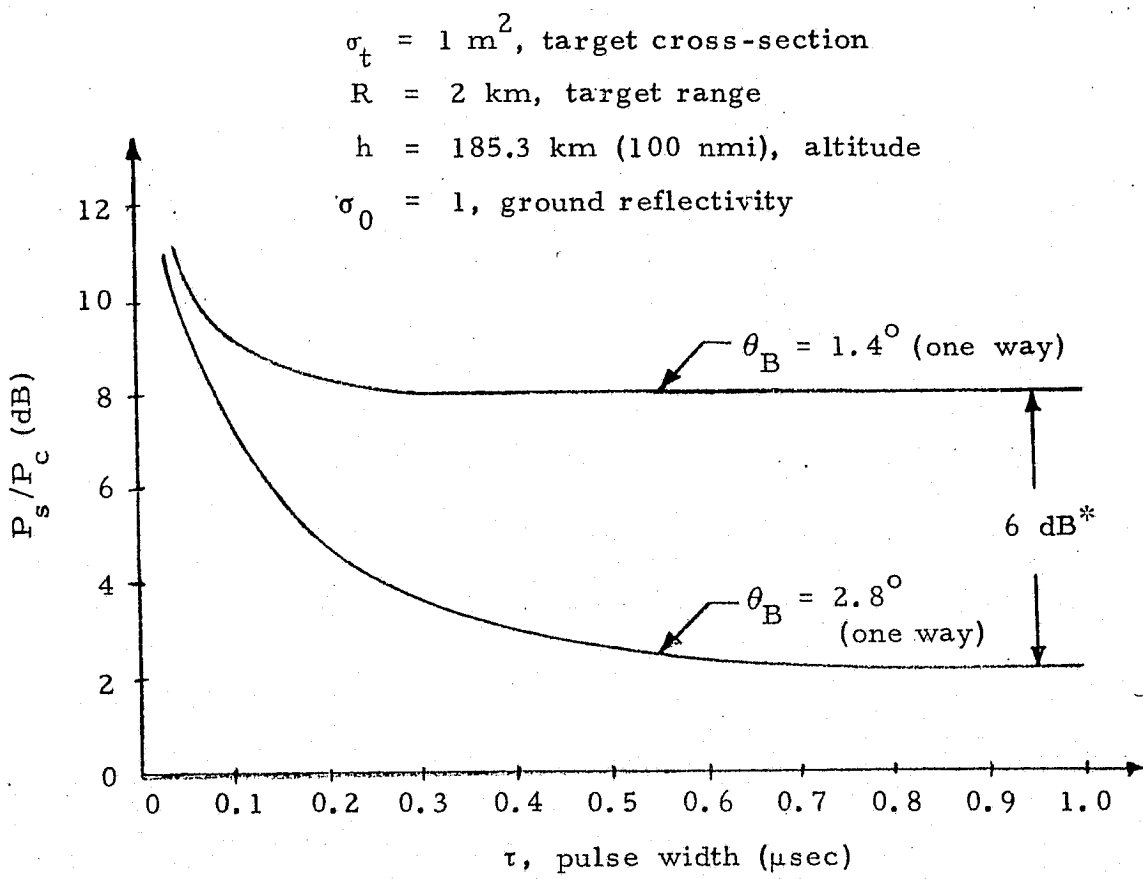
$$\sigma_t^2 = 1 \text{ meter}^2$$

$$\frac{P_s}{P_c}(0.1 \mu\text{sec}) = \frac{(4)(1.853 \times 10^5)^2}{\pi(0.72)(2 \times 10^3)^4(0.0024)(0.312)^*\sigma_0}$$

$$= \frac{1.58}{0.312 \sigma_0} = \frac{5.07}{\sigma_0} \quad \text{or} \quad +7.05 \text{ dB} - \sigma_0 \text{ (dB)}$$

$$\text{For } \sigma_0 = 1: \quad \frac{P_s}{P_c}(0.1 \mu\text{sec}) = \underline{\underline{5.07}} \quad \text{or} \quad \underline{\underline{+7.05 \text{ dB}}}$$

\* From Figure 4 at  $\tau = 0.1 \mu\text{sec}$



\* Asymptotic difference for  $\tau \gg 1 \mu\text{sec}$ .

Figure 5. Target Power-to-Ground Clutter Ratio vs. Pulse Width and Antenna Beamwidth (Boresight Target, Near Vertical Ground Return)

## 5.0 EFFECT OF GROUND REFLECTIVITY AND ATMOSPHERIC ATTENUATION

In the preceding numerical example, it was assumed that ground reflectivity,  $\sigma_0$  (also frequently referred to in the literature as  $\sigma^0$ ), was equal to unity. The reflectivity, however, varies over a large range of values and is heavily dependent on the type of reflecting surface and the angle of incidence. Figure 6 shows experimentally obtained data values of  $\sigma_0$  as a function of surface and incidence angle for frequencies of interest. From Figure 6, it is evident that only the sea return may cause  $\sigma_0$  to increase above unity at incidence angles less than 10 degrees. But for the case of relatively calm sea (wind velocity, 0-5 knots), the  $\sigma_0$  drops very sharply as the incidence angle is increased, the behavior of which is typical of near specular return. With higher wind velocities, the  $\sigma_0$  drops slower with increased angle of incidence. The latter behavior indicates that angles of incidence less than 10 degrees may present a sea return problem. However, turbulent sea state may be accompanied by other effects, such as rain squalls, which may attenuate the return. Also, with relatively turbulent sea state, frequency diversity should provide significant decorrelation of the surface return.

Atmospheric attenuation alone, not counting the specific effects of the rain absorption, will reduce the power of the near vertical ground return, thus offsetting the deleterious effects of increased surface reflectivity. At near vertical incidence, the two-way atmospheric attenuation of the ground return is estimated to be at least in the 3 to 4 dB range.

## 6.0 GROUND RETURN SUPPRESSION CONSIDERATIONS

### 6.1 Problem Statement

The analysis carried out in Section 4 of this appendix indicates that, at an altitude of 185 km (100 nmi) and the passive target range of 2 km, the  $P_s/P_c$  ratio is at best in the 7 to 9 dB range for  $\sigma_0 = 1$  and  $\tau = 0.1 \mu\text{sec}$ .

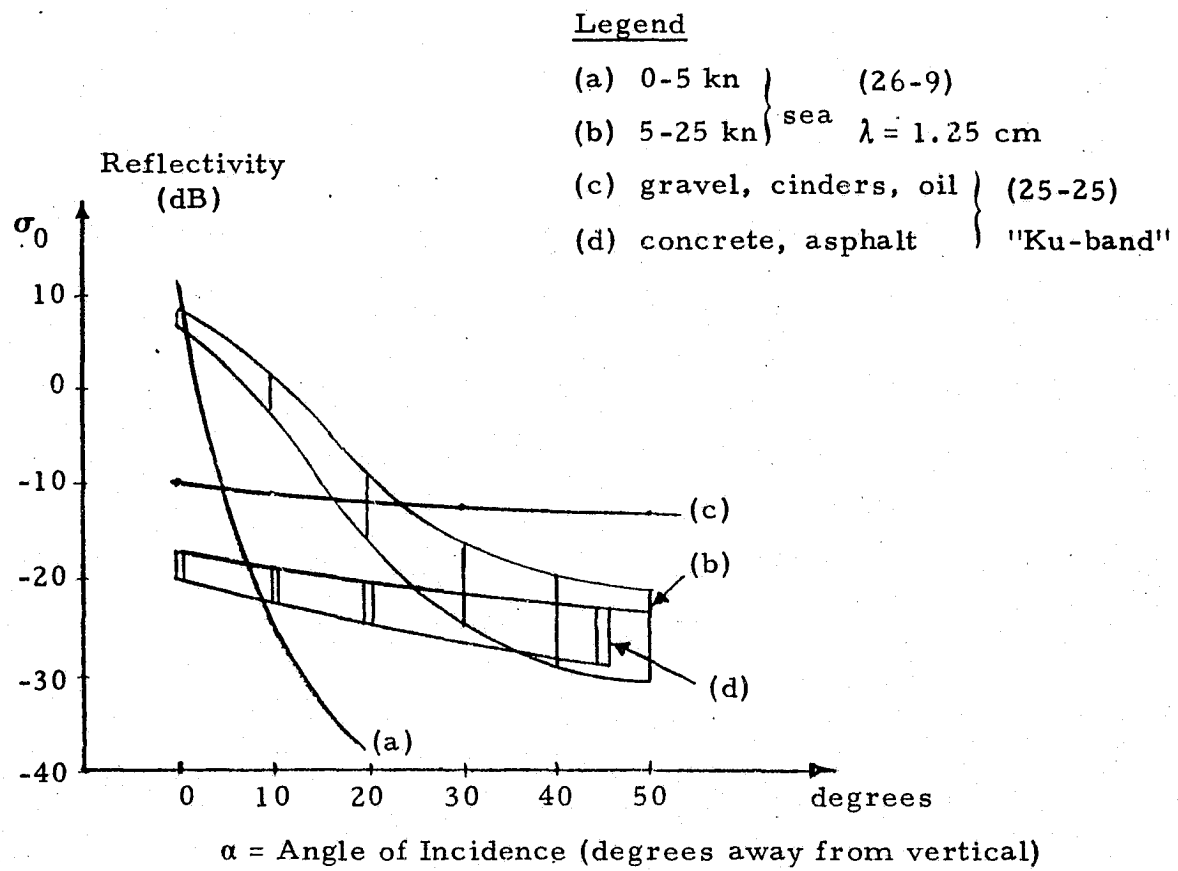


Figure 6. Reflectivity vs. Surface and Incidence Angle  $\alpha$   
 (Numbers in parentheses indicate pages in  
Skolnik's Radar Handbook)

If one includes about 4 dB of atmospheric attenuation, the  $P_s/P_c$  may increase to the 11 to 13 dB range. This extra margin, however, may be easily offset by an unpredictable increase in  $\sigma_0$ . Furthermore, the 2 km target range and  $\tau = 0.1 \mu\text{sec}$  are characteristic of the "short range" mode, the mode which follows the initial acquisition ( $R \geq 19 \text{ km}$ ) and tracking ( $2 \text{ km} \leq R \leq 19 \text{ km}$ ) modes. Thus, the problem to address is: What technique should be used to insure that the  $P_s/P_c$  ratio is sufficiently high to permit operation in any mode?

Let us look at the numbers involved. At an altitude of 185 km (100 nmi), the round trip time to ground surface is 1.253 msec, corresponding to a PRF of 810 pps. Thus, one could consider using the PRF of about 800 pps or lower and obtain range discrimination in real time. Such an approach would require working with a low duty cycle, thus essentially going to a noncoherent pulse radar system. The range tracking must then be performed by differentiating range track information. For short range operation, i.e., at 2 km or so, sufficient SNR could be obtained with peak power commensurate with pulse doppler radar (40 to 50 watts peak). But at longer ranges, i.e., ranges commensurate with 19-20 km passive target detection ranges, peak powers in the order of several kilowatts will be required.

In principle, one could also consider ground clutter discrimination based on doppler analysis of target and ground. Such discrimination, however, would depend on proper range gating of the return and this, in itself, may be a problem because of range ambiguity of the ground return. The nonambiguous range PRF of 800 pps cannot be used for the doppler tracking because it allows only 4 m/sec nonambiguous velocity readout. All other PRFs higher than 800 pps would result in the possibility of range gate stealing by ground return at near vertical angles of incidence and values of  $\sigma_0 \geq 1$ . Also, preliminary considerations indicate that the doppler spread of the ground return is a very complex function of incidence angle and, at near vertical incidence, may vary from 0 to about 20 kHz within the  $2.8^\circ$  beamwidth. The frequency spread estimate is based on the orbital velocity

of about 7,800 m/sec for a 100 nmi orbit. The doppler shift (along the flight path) for 15 GHz operating frequency is then

$$f_d \text{ (Hz)} = (100 \text{ Hz/m/sec}) \times V_{\text{orb}} \times \sin \alpha \quad (23)$$

where  $f_d$  = doppler frequency due to element at incidence angle  $\alpha$

$V$  = orbital velocity in m/sec

$\alpha$  = angle of incidence.

Thus, for  $\alpha = 1.4^\circ$  (angle of incidence at half-beamwidth) and  $\sin \alpha = 0.024$ , we have

$$f_d = (100 \text{ Hz/m/sec})(7800 \text{ m/sec})(0.024) = 19,000 \text{ Hz.} \quad (24)$$

Although the arguments supported by (23) and (24) are rather general, they do point to the fact that doppler velocity discrimination techniques may be complicated unless  $\alpha$  is sufficiently high so that the doppler shift within the beamwidth is completely out of the low frequency range associated with the -23 to +45 m/sec passive target velocity spread. For example, if  $\alpha \geq 10^\circ$ , the minimum doppler shift frequency is about 135 kHz. This necessitates PRF of at least 270 kpps to prevent ground spectrum foldover (aliasing) into the region of low frequencies. Nevertheless, ground return suppression by doppler frequency discrimination cannot be ruled out if one imposes a restriction on the minimum value of  $\alpha$  permitted during rendezvous.

## 6.2 High Frequency Hop Rate Method for Ground Return Suppression

The simplest solution for ground return suppression is to increase the rate of frequency diversity hops. Thus, if we let  $t_f \leq T_{\text{gr}}$  ( $T_{\text{gr}} = 1.235$  msec), where  $t_f$  is the frequency dwell time, the receiver will shift to another frequency when the ground return arrives. The PRF line widening (smear) due this hop rate is

$$B_i \approx \frac{1}{t_f} = \frac{1}{1.235 \times 10^{-3}} = 810 \text{ Hz.} \quad (25)$$

For frequency averaging time  $T_A$ , the residual frequency uncertainty  $\sigma_F$  is:<sup>\*</sup>

$$\sigma_F = \sqrt{\frac{1}{2 t_f T_A}} = \sqrt{\frac{B_i}{2 T_A}} . \quad (26)$$

Thus, for  $B_i = 810$  Hz and  $T_A = 2$  sec,

$$\sigma_F = \sqrt{\frac{810}{(2)(2)}} = 14.2 \text{ Hz} \geq 10 \text{ Hz} \text{ (spec for } \sigma_V = 0.1 \text{ m/sec at 15 GHz).} \quad (27)$$

But, if we assume<sup>\*\*</sup> that range rate readout delay  $T_D = T_A/2$ , then we can increase  $T_A$  to 4 seconds and

$$\sigma_F = \frac{14.2 \text{ Hz}}{\sqrt{2}} = \underline{10.04 \text{ Hz}} \approx 10 \text{ Hz (spec)} . \quad (28)$$

Since most of the frequency uncertainties will be much less than 810 Hz, we can assume that the increased frequency hop rate will be the driving factor for doppler measurement accuracy. Also, if we go as far as to assume that  $\alpha \geq 45^\circ$ , then the slant range to ground is  $100 \text{ nmi} \times \sqrt{2}$ . Thus, we may gain another factor of  $\sqrt{2}$  in our  $\sigma_F$  accuracy because we can hop slower. In this case,

$$\sigma_F (\alpha \geq 45^\circ) \leq \frac{10 \text{ Hz}}{\sqrt{2}} \approx 7.1 \text{ Hz} \leq 10 \text{ Hz (spec)} . \quad (29)$$

However, with  $\alpha \geq 45^\circ$ , the  $\sigma_0$  may not be problematic unless we are concerned with ground clutter at target ranges greater than 2 km. Consequently for a more realistic assessment of frequency accuracy limitations imposed by the frequency hop method, we should restrict ourselves to values expressed by (28).

<sup>\*</sup> C. L. Weber, private communication.

<sup>\*\*</sup> W. McQuillan, RI/SD presentation of October 15, 1974, p. II.

The salient advantage of the rapid frequency hop method is that it does not impose restrictions on the time domain structure of the radar signal. Consequently, the duty cycle and the PRF(s) can be chosen to provide optimum performance for the various modes.

Also, with 6-step frequency diversity, each frequency hop cycle will be completed within about 7.4 msec, or the time corresponding to the radar range of 600 nmi. Since the orbital altitudes of the Shuttle may range from 100 to 500 nmi, each frequency hop cycle will provide clutter rejection not only for nadir return at 500 nmi but also for the slant range return of up to 600 nmi. At  $h = 500$  nmi, the slant range of 600 nmi corresponds to about  $33.6^\circ$  angle of incidence and the  $\sigma_0$  should be at least 10 dB below the nominal  $\sigma_0 = 1$  value. This reduction may not be sufficient to provide acquisition at passive target ranges of up to 20 km, but the efficiency of the frequency hop technique can be increased further by providing a vernier shift of each frequency hop cycle. Such a vernier shift can be used to provide rejection of ground returns from slant ranges many times greater than the 500-600 nmi range interval.

## 7.0 CONCLUSIONS

The transient response of the ground return clutter has been analyzed for the case of near vertical incidence, and the relationship between the parameters influencing this response has been established. The findings are consistent with the commonly established trends, namely, that the narrower pulse widths and smaller antenna beamwidths provide better clutter rejection. The use of pulses narrower than  $0.1 \mu\text{sec}$  may be questionable, however, because of the physical size of some of the larger targets, i.e., the 18-meter long Agena.

Sample calculations of  $P_s / P_c$  ratio at lowest orbital altitude of 185.3 km (100 nmi) indicate that, unless the incidence angle ( $\alpha$ ) is restricted to a minimum value of  $10^\circ$ , there exists a possibility of clutter interfering with the passive target return at ranges as close as 2 km. As the range to

the passive target increases, the target return power drops as the inverse of  $R^4$  and the ground return becomes a potential source of interference. The expected modes of interference are either the range gate or doppler tracker stealing, or both, when the ground return falling in the particular tracking gate exceeds the power of the passive target return tracked by the gate(s).

Consequently, the use of ground clutter rejection techniques is recommended. The most promising method, particularly applicable to high PRF pulse doppler systems, appears to be that of frequency hopping, and the variations thereof. Note that frequency hopping is required anyway for the purpose of target fluctuation reduction and thus the adaptation of the hopping pattern to clutter rejection should not impose excessive complication on the system design.

Specifically, the hopping pattern should be such that the radar operation is shifted to a different frequency when the ground return arrives at the receiver. The ultimate objective of the clutter rejection scheme should be to insure reliable radar operation with the passive target in all modes, including the initial acquisition and track initiation.